

Air Force Institute of Technology

AFIT Scholar

---

Theses and Dissertations

Student Graduate Works

---

3-5-2007

## Assessment of Optical Turbulence Profiles Derived from Probabilistic Climatology

Brett W. Wisdom

Follow this and additional works at: <https://scholar.afit.edu/etd>



Part of the [Atmospheric Sciences Commons](#), and the [Signal Processing Commons](#)

---

### Recommended Citation

Wisdom, Brett W., "Assessment of Optical Turbulence Profiles Derived from Probabilistic Climatology" (2007). *Theses and Dissertations*. 2918.

<https://scholar.afit.edu/etd/2918>

This Thesis is brought to you for free and open access by the Student Graduate Works at AFIT Scholar. It has been accepted for inclusion in Theses and Dissertations by an authorized administrator of AFIT Scholar. For more information, please contact [richard.mansfield@afit.edu](mailto:richard.mansfield@afit.edu).



**ASSESSMENT OF OPTICAL TURBULENCE PROFILES  
DERIVED FROM PROBABILISTIC CLIMATOLOGY**

THESIS

Brett W. Wisdom, Captain, USAF

AFIT/GEO/ENP/07-02

DEPARTMENT OF THE AIR FORCE  
AIR UNIVERSITY

***AIR FORCE INSTITUTE OF TECHNOLOGY***

Wright-Patterson Air Force Base, Ohio

APPROVED FOR PUBLIC RELEASE; DISTRIBUTION UNLIMITED

The views expressed in this thesis are those of the author and do not reflect the official policy or position of the United States Air Force, Department of Defense, or the United States Government.

AFIT/GEO/ENP/07-02

ASSESSMENT OF OPTICAL TURBULENCE PROFILES  
DERIVED FROM PROBABILISTIC CLIMATOLOGY

THESIS

Presented to the Faculty  
Department of Engineering Physics  
Graduate School of Engineering and Management  
Air Force Institute of Technology  
Air University  
Air Education and Training Command  
In Partial Fulfillment of the Requirements for the  
Degree of Master of Science in Electrical Engineering

Brett W. Wisdom, BSEE  
Captain, USAF

22 March 2007

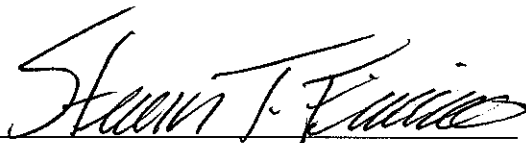
APPROVED FOR PUBLIC RELEASE; DISTRIBUTION UNLIMITED

ASSESSMENT OF OPTICAL TURBULENCE PROFILES  
DERIVED FROM PROBABILISTIC CLIMATOLOGY

Brett W. Wisdom, BSEE

Captain, USAF

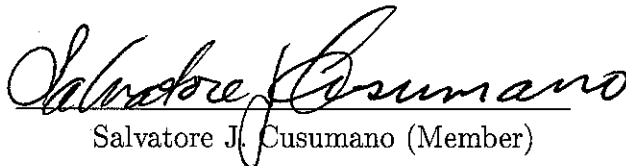
Approved:



Steven T. Fiorino (Chairman)

5 MAR 07

date



Salvatore J. Cusumano (Member)

5 MAR 07

date



Richard J. Bartell (Member)

5 MAR 2007

date

## *Abstract*

Optical turbulence profiles normally come in only two forms, empirical profiles, such as Clear 1, and parametric models, such as Hufnagel-Valley 5/7. However, these turbulence models are tailored for specific locations and climatic conditions and are not suitable in all cases. The AFIT Center for Directed Energy developed the High Energy Laser End-to-End Operational Simulation (HELEEOS) Climatological  $C_n^2$  optical turbulence model to compensate for this shortcoming in the empirical models. The Climatological  $C_n^2$  profiles in HELEEOS allow for individual optical turbulence forecasts based on the probabilistic site climatology for sites located in the desert and mid-latitude climates. Combining the climatological record with a forecast of the strength of optical turbulence results in the Climatological  $C_n^2$  profiles described in this thesis.

Comparisons of the HELEEOS probabilistic Climatological  $C_n^2$  profiles are made to thermosonde data collected from several worldwide sites. Data are collected for three desert and six mid-latitude sites corresponding to the ExPERT locations found in HELEEOS. Path-integrated values of the optical turbulences are calculated and compared at three distinct altitudes.

A Design of Experiments (DOE) factorial design matrix is used to establish statistical equivalence between the forecasted strength of the HELEEOS Climatological  $C_n^2$  path-integrated turbulence values and the measured thermosonde dataset. The HELEEOS and thermosonde datasets are shown to be statistically equivalent for the HELEEOS Mode turbulence profiles with a 500 m boundary layer. The profiles are shown to be accurate representations of the observed optical turbulence field. Confidence intervals, to within 80% confidence, are established for all HELEEOS Desert and Mid-latitude sites. These deterministic values provide the basis for future efforts to characterize the optical turbulence in mid-tropospheric HEL applications.

In addition, wave-optics simulations are used to determine the suitability of the HELEEOS Climatological  $C_n^2$  as an input turbulence model. Results show that the HELEEOS Climatological  $C_n^2$  turbulence models consistently provide improved performance in the long term spot size of a propagated HEL beam over currently available optical turbulence models. In the case of the ABL standard, 2 x Clear 1, HELEEOS routinely outperforms the standard in all simulations, providing a 17% improvement in spot size.

## *Acknowledgements*

First and foremost, I would like to say thank you to my advisor, Lt. Col Fiorino, for allowing me to research a topic that combined two interest areas for me - optical turbulence and weather. Some people cannot say they enjoyed their thesis research; I can say I enjoyed it everyday. I would also like to thank Rick Bartell. His guidance and insight into HELEEOS was critical to this thesis. Thank you for your patience in working with me, Rick, even if it meant explaining the same things multiple times. I think I finally understand how HELEEOS computes the Climatological  $C_n^2$  profiles in the boundary layer. I would also like to thank Dr. Salvatore Cusumano, whose expertise challenged me to fully explore optical turbulence and wave optics simulations.

I am indebted to Lt John Meyers and Dr. George Jumper at AFRL, who provided the entire thermosonde dataset used in this research. Thank you for your timely delivery and the quality of the products. I owe a great deal of gratitude to Matt Krizo, who responded immediately to every Matlab<sup>®</sup> problem I encountered in HELEEOS. Thank for all the Matlab<sup>®</sup> help and guidance; it was greatly appreciated.

Finally, I want to say thank you to the one person that made the most difference during my tenure at AFIT - my wonderful wife, Peggy. Thanks for enduring this seemingly endless separation and the perpetual travel back and forth to Ohio with such grace. Thank you, sweetheart, for understanding the demands of this program on my time, and for sacrificing our time together for the pursuit of my own goals. Without your DOE expertise this never could have happened, and I dedicate this thesis to you. You mean the world to me. I love you beautiful.

Brett W. Wisdom



## Table of Contents

	Page
Abstract . . . . .	iv
Acknowledgements . . . . .	vi
List of Figures . . . . .	ix
List of Tables . . . . .	xiii
I. Introduction . . . . .	1
1.1 Problem Significance . . . . .	1
1.2 Introduction to High Energy Lasers . . . . .	2
1.3 Introduction to Optical Turbulence . . . . .	3
1.4 Problem Statement . . . . .	6
1.5 Research Goals . . . . .	8
1.6 Organizational Overview . . . . .	8
II. Background and Literature Review . . . . .	10
2.1 Chapter Overview . . . . .	10
2.2 The Statistical Atmosphere . . . . .	10
2.2.1 Covariance and Power Spectral Density Functions . . . . .	11
2.2.2 Structure Functions . . . . .	13
2.3 Theories of Optical Turbulence Spectra . . . . .	15
2.4 $C_n^2$ and Moments of $C_n^2$ . . . . .	17
2.5 Optical Turbulence Profiles . . . . .	22
2.6 HELEEOS . . . . .	25
2.7 Design of Experiments . . . . .	33
III. Research Methodology and Data . . . . .	41
3.1 Chapter Overview . . . . .	41
3.2 Generalized Test Approach . . . . .	41
3.3 Terminology . . . . .	43
3.4 Thermosonde Data . . . . .	44
3.5 HELEEOS Data . . . . .	50
3.6 DOE Test Methodology and Design . . . . .	56

	Page
IV. Results . . . . .	61
4.1 Validation of the Statistical Model . . . . .	61
4.2 Data Manipulation and Blocking Factors . . . . .	62
4.3 Results . . . . .	65
4.3.1 Transformed Data Results . . . . .	66
4.3.2 Untransformed Data Results . . . . .	70
4.4 Application of the Model . . . . .	83
4.5 Overall Results . . . . .	90
V. Conclusions and Recommendations . . . . .	92
5.1 Research Conclusions . . . . .	92
5.2 Recommendations and Future Work . . . . .	95
Bibliography . . . . .	101

## List of Figures

Figure		Page
1.1.	Airborne Laser. The COIL integrated into the Boeing 747 provides the needed firepower to destroy enemy missiles in the boost phase. The ABL is designed to operate at high-altitudes over a designated battlefield near missile launch areas. The turret at the front of the aircraft accurately focuses the laser beam and provides the needed atmospheric compensation. Courtesy of Boeing Corporation, photo credit: USAF Photo by Jim Shryne. <a href="http://www.boeing.com/defense-space/military/abl/">http://www.boeing.com/defense-space/military/abl/</a> . . . . .	3
1.2.	Advanced Tactical Laser. The COIL integrated into the C-130 provides the needed firepower to destroy surface based enemy targets. Courtesy of Boeing Corporation. <a href="http://www.boeing.com/news/feature/aa2004/backgrounders/advanced_tactical_laser.pdf">http://www.boeing.com/news/feature/aa2004/backgrounders/advanced_tactical_laser.pdf</a> . . . . .	4
1.3.	HELEEOS Graphical User Interface. . . . .	7
2.1.	Richardson cascade theory of energy. The inner scale of turbulence is denoted by $l_0$ , while the outer scale is denoted by $L_0$ . Eddies between the scale sizes of $l_0$ and $L_0$ represent the inertial subrange. Energy injected into the atmospheric volume is transferred from eddy to eddy until it is fully dissipated, shown by the arrows. Adopted from Andrews and Phillips, 2006 . . . . .	16
2.2.	Kolmogorov and von Kármán spectral models of refractive index fluctuations. The inner scale of turbulence is 1 cm; the outer scale of turbulence is 10 m. The Kolmogorov spectrum is represented by a classical -11/3 power law. The von Kármán modifications to the Kolmogorov spectrum can be seen in the spectral "roll-off" near the limits of the inertial subrange. The von Kármán spectrum is finite and isotropic for <i>all</i> wavenumbers. Reproduced from Andrews & Phillips, 2006 . . . . .	18
2.3.	Example of a thermosonde payload. This measuring device is carried aloft by a weather balloon, and the airborne instrument package is capable of measuring temperature differentials using fine-wire probes separated by a 1 m distance. Measurements are taken every 7-8 m in the vertical, to an altitude of 30 km above sea level. Thermosonde measurement are normally conducted at night to eliminate the effects of solar radiation on the fine-wire probes. In addition to the temperature measurements, the thermosonde also measures pressure, humidity and horizontal wind velocity. The $C_n^2$ vertical profile is depicted on the right side of the figure. . . . .	19
2.4.	Atmospheric coherence length and isoplanatic angle. The atmospheric coherence length, $r_0$ is the maximum spatial extent over which the propagated wavefront remains correlated. The isoplanatic angle, $\theta_0$ , is the maximum angular separation over which the turbulence remains unchanged. . . . .	21

Figure		Page
2.5.	Optical turbulence profiles. Subplot (a) shows the model comparison through 30 km. Note the stronger turbulence values of the CLEAR I Night profile in the lower atmospheric regions below the boundary layer. The SLC Day and SLC Night profiles are identical above the boundary layer. The only distinction is the SLC Night has a lower turbulence value below the boundary layer than the SLC Day. The SLC profiles use the HV57 profile for altitudes below 18.5 m. Subplot (b) shows the distinctions in the two SLC models as well as the pronounced strength of the Clear I model below 1230 m. . . . .	24
2.6.	Worldwide EXPERT sites. The user can select any of the more than 400 global sites. Each site contains specific climatological data pertinent to that site. Climatological $C_n^2$ is one atmospheric parameter that can be selected for each site. . . . .	26
2.7.	Example log-normal distributions and percentiles. The distributions are all log-normally distributed. The shaded area represents the percentile of interest. The mode value is the most frequent value contained in the distribution. The shaded area can be interpreted as containing that percentage of all $C_n^2$ observations. For example, the 80 <sup>th</sup> percentile contains 80% of all $C_n^2$ observations obtained from the thermosonde soundings. The log-normal distributions were generated using the equation: $p_I(I) = \frac{1}{\sqrt{2\pi}I\sigma_I} \exp \left[ -\frac{\left( \ln\left(\frac{I}{\langle I \rangle}\right) + \frac{1}{2}\sigma_I^2\right)^2}{2\sigma_I^2} \right]$ . . . . .	27
2.8.	Example Climatological $C_n^2$ profiles for Wright-Patterson AFB, OH. Three user-defined percentiles of interest are shown: Mode, 80 <sup>th</sup> , and 99 <sup>th</sup> percentile. The relative magnitude of the Climatological $C_n^2$ profiles increases as the percentiles of interest increase. This is expected, since the 99 <sup>th</sup> percentile encapsulates 99% of all $C_n^2$ measurements within one standard deviation. . . . .	32
2.9.	HELEEOS Climatological $C_n^2$ and thermosonde profiles for Vandenberg AFB, CA. . . . .	33
2.10.	A two-factor factorial design. The figure on the left is a factorial design without interactions. The figure on the right is a factorial design with interactions. Adapted from Montgomery, 2006 . . . . .	37
2.11.	A two-factor factorial design. The figure on the left is a factorial design without interactions. The figure on the right is a factorial design with interactions. The crossed lines in (b) indicate interactions between Factor A and Factor B. Adapted from Montgomery, 2006 . . . . .	38
3.1.	Vertical $C_n^2$ profiles of an actual thermosonde flight launched from Holloman AFB, NM. The complete vertical profile of the launch is shown in (a), while the 5k ft, 10k ft and the 20k ft vertical profiles are shown in (b), (c) and (d) respectively. The elevation was 609 m. Note the large variations in the magnitude of the optical turbulence along the ascension path. Increasing temperature gradients and stronger optical turbulence are observed at the top of the boundary layer near 1800m, and at 4300m, possibly created by mountain wave activity in the vicinity of launch. . . . .	45

Figure		Page
3.2.	Thermosonde distributions for three mid-latitude and one desert site. The lognormal distribution can be seen in each plot. For larger sample sizes, the lognormal distribution becomes apparent, as in (c) and (d). Small sample sizes do not exhibit a recognizable lognormal distribution, but it is assumed all thermosondes are lognormally distributed.	50
3.3.	HELEEOS Atmosphere GUI for 500 m boundary layer. Notice the time of day selection 00:00-03:00 results in a 500 m boundary layer. The HELEEOS turbulence percentiles are also depicted. . . . .	51
3.4.	HELEEOS Atmosphere GUI for 1524 m boundary layer. Note Local Time of Day is the default value of Daily Average. The 1524 m boundary layer can also be selected by using Local Time of Day 09:00-21:00.	52
3.5.	Random $C_n^2$ profiles generated by the <i>RandCn2Prof</i> function in <i>ATMTools</i> <sup>®</sup> . The black line is the HELEEOS profile created for Holloman AFB, NM (ExPERT Summer, mode Climatological $C_n^2$ turbulence, 50th percentile RH, and daily average temperature). The blue, red and green lines are the random $C_n^2$ profiles created that retain the same atmospheric parameters of $r_0$ , $\theta_0$ and $\sigma_R^2$ as the basis atmospheric structure (the black profile). Standard deviation for 1000 random iterations was $7.1081 \times 10^{-17} \text{ m}^{-2/3}$ . Note: all altitudes are in m above ground level (AGL) rather than m mean sea level (MSL). . . . .	53
3.6.	Log normal distribution of 5000 random $C_n^2$ realizations using <i>ATMTools</i> <sup>®</sup> . The rough lognormal curve is depicted by the red line. As the number of iterations increase, the distribution becomes even more "classically" lognormally distributed. . . . .	54
3.7.	Problems associated with the boundary layer calculations in HELEEOS. In (a), constant Climatological $C_n^2$ values are observed from about 360 m through 1524 m. In (b), the temporary software solution produced a smooth curve from about 360 m to 1524 m. . . . .	56
3.8.	Partial DOE nighttime summer design matrix for Vandenberg AFB, CA. The nighttime thermosonde data served as the test truth data for both the nighttime and daytime (daily average) Time of Day categories.	57
3.9.	Partial DOE daytime summer design matrix for Vandenberg AFB, CA.	58
4.1.	Histogram plot of the residual errors is shown in (a). The normal probability plot of the residuals is shown in (b). The plot shows acceptable correlation of the residuals. All residuals fall within three standard deviations of the mean. The model was not a perfect model as shown by the lack of perfect linearity in the residual errors. . . .	63
4.2.	Least squares means for all locations. The blue line is the HELEEOS results and the red line is the thermosonde results. The vertical bars indicate 80% confidence intervals. The blue circle denotes the mean value of the HELEEOS datasets and the red square denotes the mean value of the thermosonde datasets. . . . .	67
4.3.	Least squares means plot of the effects of Altitude and Location on the HELEEOS and thermosonde path-integrated $C_n^2$ values. Plots (a-1) and (a-2) demonstrate the consistency of both the HELEEOS and thermosonde. Plot (b) breaks the altitudes out for a closer analysis. All plots are for the combined effects of Mode and 50 <sup>th</sup> percentile turbulence levels. . . . .	70

Figure		Page
4.4.	(a) Weighted marginal means plot of the effects of Summer and Altitude for the HELEEOS and thermosonde path-integrated $C_n^2$ values. (b) Weighted marginal means plot of the effects of Winter and Altitude for the HELEEOS and thermosonde path-integrated $C_n^2$ values. All plots combine the effects of the Mode and 50 <sup>th</sup> percentile turbulence levels. . . . .	71
4.5.	Weighted marginal means plot of the effects of Season and Location on the HELEEOS and thermosonde path-integrated $C_n^2$ values. The results are similar to the least squares means plot of the previous figure.	72
4.6.	Final results for Desert Summer Mode (plot (a)) and 50 <sup>th</sup> percentile (plot (b)) turbulence profiles. Note the lognormal distribution of the confidence intervals, consistent with naturally occurring distributions of atmospheric turbulence values. . . . .	73
4.7.	Final results for Desert Winter Mode (plot (a)) and 50 <sup>th</sup> percentile (plot (b)) turbulence profiles. Note the lognormal distribution of the confidence intervals, consistent with naturally occurring distributions of atmospheric turbulence values. . . . .	76
4.8.	Final results for Mid-latitude Winter Mode (plot (a)) and 50 <sup>th</sup> percentile (plot (b)) turbulence profiles. Note the familiar lognormal distribution of the confidence intervals, consistent with naturally occurring distributions of atmospheric turbulence values. . . . .	78
4.9.	Final results for Mid-latitude Summer Mode (plot (a)) and 50 <sup>th</sup> percentile (plot (b)) turbulence profiles. . . . .	82
4.10.	Mid-latitude Summer sites vertical Climatological $C_n^2$ profiles, sfc-10k ft. The 500 m boundary layer (BL) is indicated by the blue line and the 1524 m boundary is indicated by the red line. In all cases of the Mid-latitude Summer profiles, the nighttime vertical Climatological $C_n^2$ profile (500 m BL) is stronger than the daytime vertical Climatological $C_n^2$ profile (1524 m BL). The subplots are shown from the sfc-10k ft for clarity of the boundary layer. . . . .	84
4.11.	Long-term spot size 45.6 ms realization using the Clear optical turbulence model. The long-term spot size is 12.4 cm. . . . .	86
4.12.	Long-term spot size 45.6 ms realization using the HV57 optical turbulence model. The long-term spot size is 10.7 cm. . . . .	87
4.13.	Long-term spot size 45.6 ms realization using the Winter HELEEOS Climatological $C_n^2$ Mode turbulence profile for Holloman AFB, NM . The long-term spot size is 10.3 cm. . . . .	88
4.14.	Long-term spot size 45.6 ms realization using the Summer HELEEOS Climatological $C_n^2$ Mode turbulence profile for Holloman AFB, NM. The long-term spot size is 10.4 cm. . . . .	89
4.15.	Long-term spot size 45.6 ms realization using the Winter HELEEOS Climatological $C_n^2$ Mode turbulence profile for Osan AB, NM. The long-term spot size is 10.6 cm. . . . .	91
5.1.	Sample Summer Climatological $C_n^2$ profile depicting envelope of turbulence coverages for Holloman AFB, NM. . . . .	97

## *List of Tables*

Table		Page
2.1.	SLC Daytime and Nighttime Models . . . . .	23
2.2.	CLEAR I Night Model . . . . .	24
3.1.	Locations of Thermosonde Campaigns and Nearest ExPERT Site	42
3.2.	Seasonal Thermosonde Campaigns . . . . .	47
3.3.	Thermosonde $C_n^2$ Statistics . . . . .	49
4.1.	HELEEOS 80% Confidence Intervals (CI) for ExPERT Desert Sites . . . . .	75
4.2.	HELEEOS 80% Confidence Intervals (CI) for ExPERT Mid-Lat Sites . . . . .	81

# ASSESSMENT OF OPTICAL TURBULENCE PROFILES DERIVED FROM PROBABILISTIC CLIMATOLOGY

## I. Introduction

### 1.1 *Problem Significance*

Developing a technique for accurately forecasting optical turbulence has long been a concern in high energy laser (HEL) applications. Atmospheric optical turbulence produces adverse results on HEL propagation and the available energy delivered on a distant target. Early HEL tests with CO<sub>2</sub> lasers noted these energy-depleting impacts, and these same effects still resonate today with the next generation of high energy lasers, the Chemical Oxygen Iodine Laser or COIL. After the first Gulf War, a new requirement surfaced to develop and deploy a laser weapon system capable of destroying an enemy missile during a launch phase. However, this meant developing a greater understanding of the impacts of the atmosphere on a propagated laser beam.

Profiles of atmospheric optical turbulence emerged from studies conducted in the 70s and 80s, and these are the standards still today. However, there are inherent limitations with these profiles, particularly when applying them on a global scale. The original measurements used to empirically derive these profiles originated in desert and maritime climates. Even though these standards are in widespread and in even global use, they arose from data collected in very specific climates with homogeneous characteristics. As a result, the usefulness of each profile is limited to atmospheric regimes matching those of the original test site.

In an effort to improve upon these profiles, AFIT's Center for Directed Energy (CDE) developed a novel technique for forecasting optical turbulence based on probabilistic climatology. This unique new feature is part of the High Energy Laser End-to-End Operational Simulation (HELEEOS) software package. Its uniqueness stems from its ability to correlate optical turbulences to corresponding percentiles of



temperature and relative humidity at many worldwide sites. The optical turbulence values correlated to the relative humidity percentiles are the basis for the vertical optical turbulence profiles in the most dynamic layer of the atmosphere, the layer from the earth's surface to approximately 5k ft above ground level, known as the boundary layer. The climatological record is the most reliable long term metric for the weather at a site, and HELEEOS computes individual optical turbulence profiles by capitalizing on this extensive seasonal weather data. This is quite unique to the software, and is a method that has not been attempted elsewhere.

Past studies [8] showed that the HELEEOS climatology-based  $C_n^2$  profiles qualitatively compare well with the empirical standards. However, no quantitative analysis on the confidence of these profiles currently exists. This research effort develops a practical user level of confidence in these profiles.

## ***1.2 Introduction to High Energy Lasers***

The age of the laser began in 1961. [22] It is often opined that the laser was a solution in search of a problem. The laser quickly found utility in a wide range of applications such as communications, data storage and retrieval, and an ever-popular desire as a lethal weapon system. Vast resources of time and money have been invested in developing and deploying a battlefield directed energy weapon. The Airborne Laser (ABL) is just such a platform, projected to deliver destructive firepower to destroy enemy missiles during the boost phase of a flight. The ABL is a mega-Watt class chemical oxygen-iodine laser (COIL) integrated aboard a Boeing 747 aircraft and designed to provide the needed lethality to rupture an enemy missile's fuel or oxidizer tanks [20, 21]. Figure 1.1 shows the USAF's recently delivered ABL.

The tactical equivalent of the ABL is the Advanced Tactical Laser (ATL), currently in the Advanced Concept Technology Demonstration (ACTD) acquisition phase. This COIL laser is integrated into a C-130 Special Operations aircraft and is intended to provide precise directed energy for battlefield and urban operations. [3, 6]



Figure 1.1: Airborne Laser. The COIL integrated into the Boeing 747 provides the needed firepower to destroy enemy missiles in the boost phase. The ABL is designed to operate at high-altitudes over a designated battlefield near missile launch areas. The turret at the front of the aircraft accurately focuses the laser beam and provides the needed atmospheric compensation. Courtesy of Boeing Corporation, photo credit: USAF Photo by Jim Shryne. <http://www.boeing.com/defense-space/military/abl/>

Its primary application is destruction of ground-based targets from a mid-tropospheric orbit. Figure 1.2 shows the proposed design and application of this high-energy laser.

According to the Government Accountability Office (GAO), atmospheric compensation for the airborne laser is a critical program risk element. The deficiencies in atmospheric compensation arise from jitter control of the laser beam, that is, providing the lethality to a stable, fixed location on the missile or target on the ground. [20,21]. Atmospheric compensation is the one of the least mature technologies for these programs [20,21], and is considered critical to program completion. Therefore, knowledge and understanding of the atmospheric medium is cornerstone to successful employment of these HELs.

### *1.3 Introduction to Optical Turbulence*

Lethal application of directed energy firepower through a volume of the atmosphere requires extensive knowledge of the effects of the atmosphere on the propa-

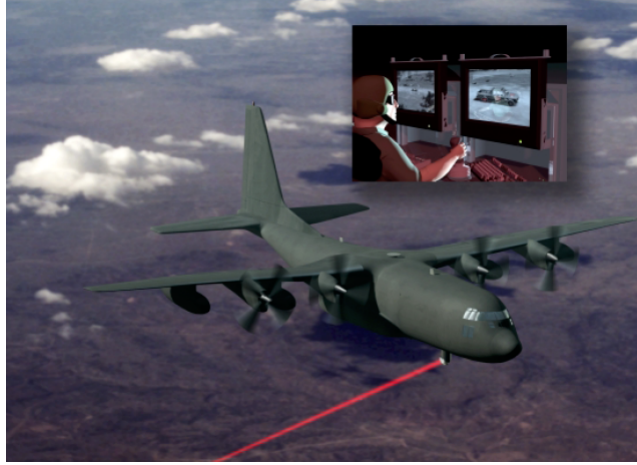


Figure 1.2: Advanced Tactical Laser. The COIL integrated into the C-130 provides the needed firepower to destroy surface based enemy targets. Courtesy of Boeing Corporation. [http://www.boeing.com/news/feature/aa2004/backgrounders/advanced\\_tactical\\_laser.pdf](http://www.boeing.com/news/feature/aa2004/backgrounders/advanced_tactical_laser.pdf)

gating laser beam. A laser beam propagating through the atmosphere encounters random temperature differentials that create atmospheric density fluctuations and, in turn, induce random changes in the atmospheric index of refraction. These random fluctuations in the index of refraction, known as optical turbulence, along the path of the laser beam create phase errors on the propagating wavefront. Atmospheric turbulence affects the optical and infrared wavelengths, and is critically important to applications such as the ABL and ATL. Optical turbulence induces adverse beam effects such as beam spread, beam wander and jitter, and scintillation. All of these result in beam degradation beyond the diffraction limit and loss of power on the target, and if severe enough can significantly reduce the lethality of the weapon system.

The primary indicator of the strength of optical turbulence is the index of refraction structure constant,  $C_n^2$ . This index is measured in units of  $m^{-2/3}$  and is often on the order of  $10^{-13} m^{-2/3}$  or less. Since the late 1970s, several optical turbulence profiles have emerged as standards, based on empirical measurements of  $C_n^2$  values throughout the atmosphere.  $C_n^2$  is a function of altitude; the turbulence is strongest near the surface of the earth, and generally decreases with increasing altitude. It also

increases aloft near locations of distinct atmospheric phenomena such as jet streams or the vertical extent of frontal airmasses where strong temperature differentials exist.

For a laser beam propagating through the atmosphere at a zero zenith angle, the turbulence along the path is similar to that predicted by these empirical turbulence standard profiles. For a propagation path at some angle  $\zeta$ , the  $C_n^2$  value along the path becomes a function of  $\cos(\zeta)$ . A beam traversing a slant path a distance from zenith encounters a greater volume of optical turbulence along the propagation path than along a zero zenith angle. As a result, the path integrated  $C_n^2$  value must take into account the slant angle and slant range. Any factor depending on the path integrated  $C_n^2$  value must also assume an angular dependence on the optical turbulence. This concept has added significance for ATL applications where the propagation path is always a slant path from an orbit to ground based targets. The greater the slant range, the more degradation caused by the turbulence.

It is generally accepted that a path-integrated value of  $C_n^2$  is a truer measure of the strength of optical turbulence than a single point value of  $C_n^2$ . Constant values of  $C_n^2$  relate only to horizontal propagation paths. For any vertical path, the best measure of the overall strength of the turbulence field is the path-integrated sum of the turbulence along that path. It is dependent on the distance traveled through the vertical column of the atmosphere and the vertical depth of the differential layers. However, propagation distance is not the only factor in assessing the strength of the optical turbulence field. The location of the greatest turbulence along the optical path is also a significant factor. Strong turbulence located close to the aperture induces stronger turbulence effects than turbulence located close to the target. If the strongest turbulence is located closest to the aperture, at the initial point of the propagation path, the overall effect is a loss of spatial coherence resulting in large amplitude variations in the beam. If the strongest turbulence is located near the target, the result is still a loss of spatial coherence, but not as pronounced as that nearest the aperture. However, pockets of increased turbulence throughout the vertical slant path cause additional losses in the beam energy and often severely degrade the beam. For

a platform such as the ATL, this is very important since optical turbulence acts to reduce the total energy per unit area on the target and degrade the lethality and performance of the laser weapon system.

#### **1.4 Problem Statement**

HELEEOS is a parametric one-on-one engagement level software model. It was developed by the AFIT Center for Directed Energy and sponsored by the High Energy Laser Joint Technology Office (JTO). [4] It incorporates scaling laws tied to respected wave optics code for laser beam propagation, and is capable of integrating all significant degradation effects such as thermal blooming, aerosol and molecular absorption and scattering, and optical turbulence into its calculations. The strong point of HELEEOS is that it enables the user to evaluate the uncertainty in low-altitude HEL engagements due to all major clear-air atmospheric phenomena. Figure 1.3 shows the HELEEOS main graphical user interface. The user defines the engagement scenario within the Atmosphere, Geometry, Target and Laser System Mission Parameters menus.

A computational feature unique to HELEEOS is the climatology-based optical turbulence prediction, referred to as Climatological  $C_n^2$  hereafter in this thesis. Gravley showed these climatological profiles are qualitatively equivalent by comparison to both empirical models and simulation models of  $C_n^2$  profiles. [8] This makes it well suited as a forecasting aid in electro-optical and infrared (EO/IR) mission planning and execution. A field analysis tool is currently not available to predict the strength of optical turbulence at most worldwide locations, but HELEEOS has the potential to fill this void by predicting optical turbulence based on the climatological record of surface and upper air environmental parameters. These Climatological  $C_n^2$  profiles, currently available for only Mid-latitude and Desert locations, are based on a limited set of measured turbulence data. HELEEOS currently has no capability to produce Climatological  $C_n^2$  profiles for tropical or arctic climates.



Figure 1.3: HELEEOS Graphical User Interface.

HELEEOS is a capable optical turbulence forecasting tool, but is lacking a quantitative assessment of the path-integrated Climatological  $C_n^2$  predictions. This research effort aims to bridge that gap by developing confidence bounds for the Climatological  $C_n^2$  HELEEOS profiles based on path-integrated comparisons with actual thermosonde  $C_n^2$  measurements from a variety of worldwide locations. The Climatological  $C_n^2$  profiles combined with intervals to within 80% confidence can then be utilized as a forecast decision aid both by researchers as well as combat-ready units utilizing EO/IR weapons.

## 1.5 Research Goals

The primary goals of this research are threefold. First is to quantitatively assess HELEEOS's performance against measured optical turbulence data. The second goal is to establish confidence bounds of the path-integrated HELEEOS climatological  $C_n^2$  profiles, to within 80% confidence. Gravley showed that HELEEOS Climatological  $C_n^2$  profiles qualitatively recreate measured  $C_n^2$  profiles. However, this research aims to go another step further and assess the statistical equivalence of the path-integrated HELEEOS Climatological  $C_n^2$  profiles to measured thermosonde data and to establish confidence bounds on the HELEEOS values to within 80% confidence. This is done with a rigorous application of the statistical analysis technique known as Design of Experiments. Until now, no measures of statistical equivalency have existed for the HELEEOS Climatological  $C_n^2$  profiles, and this research effort aims to quantify, through deterministic values, this equivalence to within 80% confidence. Finally, this research effort gauges the performance of the HELEEOS Climatological  $C_n^2$  turbulence model against models recognized as the industry standards. The Climatological  $C_n^2$  turbulence model and the empirical models both serve as the input turbulence models in wave optics simulations, and HELEEOS's performance versus the standard profiles is assessed through several wave optics simulation scenarios.

## 1.6 Organizational Overview

Chapter 2 is a thorough literature review of pertinent topics necessary to the fundamental understanding of optical turbulence. In addition, Chapter 2 presents a more comprehensive look at HELEEOS and discusses in detail the methodology behind the Climatological  $C_n^2$  profiles. Finally, Chapter 2 develops the foundational knowledge for the powerful statistical analysis model known as Design of Experiments (DOE), which is the test approach used to quantify the confidence in the HELEEOS path-integrated Climatological  $C_n^2$  values. Chapter 3 outlines the test methodology of this research effort for both the thermosonde data and the HELEEOS data. Specific test locations are presented in Chapter 3 as well. In addition, Chapter 3 also develops

the DOE test design matrix for all causal factors in the test. Chapter 4 presents the results of the DOE analysis effort for both transformed test data as well as the untransformed test data. Data are presented both as composite and as site-specific results. Wave optic simulations comprise the remainder of Chapter 4, with discussion of the wave optics simulations and the parameters used in the simulations. Long term spot size is the metric for comparison of the HELEEOS profiles to the standard empirical profiles in the wave optics simulations. Chapter 5 concludes this thesis and provides recommendations as well as areas of future research work.



## II. Background and Literature Review

### 2.1 Chapter Overview

The purpose of this chapter is to provide a theoretical foundation and a comprehensive literature review on the subject of atmospheric optical turbulence, as well as past research efforts dealing with the effects of micrometeorology on the strength of optical turbulence. This chapter also provides an overview of the HELEEOS software package and the statistical design method known as Design of Experiments. The first section discusses the statistical nature of the atmosphere and presents fundamental turbulence theory. Section 2.3 introduces the Kolmogorov and von Kármán spectra and establishes mainstream turbulence theory. Section 2.4 discusses the refractive index structure constant,  $C_n^2$ , and its related moments. Section 2.5 describes several different empirical optical turbulence profiles. Section 2.6 is a detailed explanation of the HELEEOS Climatological  $C_n^2$  product. The HELEEOS databases and the ExPERT climatological database are presented in this section. Section 2.7 lays the foundational theory for an introductory overview of the test design methodology known as Design of Experiments.

### 2.2 The Statistical Atmosphere

Any optical system utilizing electromagnetic radiation must account for the characteristics of the medium through which it propagates. The atmosphere is the path medium for mid-tropospheric HEL applications, and as such, it is essential to understand optical turbulence in order to efficiently propagate a focused laser beam over any distance through it. Viscous flow throughout the atmosphere falls into two categories: laminar flow and turbulent flow, each represented by a characteristic Reynolds number. Slow mixing rates and uniformly changing velocities characterize laminar flow. Turbulent flow, on the other hand, is a chaotic regime with constantly varying velocity fields. Due to these rapidly changing velocity flows, random subflows called turbulent eddies develop. The random nature of these turbulent eddies makes closed form mathematical representation very difficult, if not impossible, due to many

different variables involved. As a result, atmospheric turbulence becomes a nonlinear, three dimensional random vector process requiring a statistical approach with emphasis on dimensional analysis. Because of the stochastic nature of the velocity field, each point in space is modeled as a random variable. This statistical approach accurately describes both the turbulence and its effects on EO/IR systems.

*2.2.1 Covariance and Power Spectral Density Functions.* Let  $x_1$  and  $x_2$  be two realizations of a stationary random process  $x(t)$  taken at times  $t_1$  and  $t_2$  respectively. The autocorrelation function of  $x(t)$  is defined to be [1]

$$R_x(t) \equiv R_x(\tau) = \langle x(t_1)x(t_2) \rangle \quad (2.1)$$

where the brackets indicate the ensemble average of the random process. The covariance function of the random process is defined by

$$\begin{aligned} B_x(t_1, t_2) &= \langle [x(t_1) - \langle x(t_1) \rangle][x(t_2) - \langle x(t_2) \rangle] \rangle \\ &= \langle x(t_1)x(t_2) \rangle - m(t_1)m(t_2) \\ &= R_x(\tau) - m^2 \end{aligned} \quad (2.2)$$

The covariance function represents the correlation between the fluctuations from the mean at  $t_1$  with the mean at  $t_2$ . [2] The *Wiener-Khinchin* theorem established a Fourier transform relationship between the covariance function and the power spectral density (PSD) function,  $S_x(\omega)$ , defined by the expressions [1, 7]

$$B_x(\tau) = \int_{-\infty}^{\infty} e^{i\omega\tau} S_x(\omega) d\omega \quad (2.3)$$

$$S_x(\omega) = \frac{1}{2\pi} \int_{-\infty}^{\infty} e^{-i\omega\tau} B_x(\tau) d\tau \quad (2.4)$$

The three dimensional spatial covariance function describes this correlation within a volume of space for a random field  $u(\mathbf{R}) = (x, y, z; t)$ . The PSD characterizes the statistical distribution of the size and number of turbulent eddies in the volume. [19] In three dimensions, the spatial variable,  $\mathbf{R}$ , and the spatial frequency,  $\kappa$ , share the same Fourier transform relationship as the time  $\tau$  and frequency  $\omega$  in one dimension. The spatial covariance function and the spatial power spectrum of the random field  $u(\mathbf{R})$  are given by [1, 2, 19]

$$\Phi_u(\mathbf{K}) = \left(\frac{1}{2\pi}\right)^3 \int \int \int_{-\infty}^{\infty} e^{-i\mathbf{K}\cdot\mathbf{R}} B_u(\mathbf{R}) d^3 R \quad (2.5)$$

$$B_u(\mathbf{R}) = \int \int \int_{-\infty}^{\infty} e^{-i\mathbf{K}\cdot\mathbf{R}} \Phi_u(\mathbf{K}) d^3 \kappa \quad (2.6)$$

Turbulence theory is not a result of application of first principles and certain approximations must be made to account for the random nature of the atmosphere. Two important approximations are those of homogeneity and isotropy. The random field is homogeneous if the statistical moments are invariant to a time shift; likewise, the random field is isotropic if the statistical moments are invariant under rotation. Under the assumptions of *statistically homogeneous and isotropic* and recognizing the fields are real, these Fourier transform relations reduce to [1, 2, 19]

$$\Phi_u(\kappa) = \frac{1}{2\pi^2 \kappa} \int_0^{\infty} B_u(R) \sin(\kappa R) R dR \quad (2.7)$$

$$B_u(R) = \frac{4\pi}{R} \int_0^{\infty} \Phi_u(\kappa) \sin(\kappa R) \kappa d\kappa \quad (2.8)$$

where  $\kappa = |\mathbf{K}|$  is the magnitude of the wavenumber vector. Convergence of Equation 2.7 places restrictions on the behavior of the covariance function due to the singularity at  $\kappa = 0$ .

2.2.2 *Structure Functions.* The theoretical treatment of the PSD and covariance functions hinges on the assumption of homogeneity of the atmospheric volume under consideration. These assumptions stipulate constant means throughout the volume, something that obviously is not the case within the atmosphere. The means are fluctuating due to random, nonhomogeneous changes in the wind flows. However, the atmosphere can be modeled as *locally homogeneous* with slowly varying means. Structure functions provide the ability to deal with random processes in stationary increments. The random field,  $u(\mathbf{R})$  can be considered to have two parts, a mean and a locally fluctuating part,  $u(\mathbf{R}) = m(\mathbf{R}) + u_1(\mathbf{R})$ . The structure function then is the atmospherically induced variance of the locally homogeneous field: [1, 2, 19]

$$D_u(\mathbf{R}_1, \mathbf{R}_2) = D_u(\mathbf{R} = \langle [u_1(\mathbf{R}_1) - u_1(\mathbf{R}_1 + \mathbf{R})]^2 \rangle. \quad (2.9)$$

The spectrum is related to the structure function by the *Weiner-Khinchin* theorem [1, 2], which states the autocorrelation function and the power spectral density form a Fourier transform pair provided the autocorrelation function is at least wide-sense stationary. Mathematically, the structure function is defined as

$$D_u(\mathbf{R}) = 2 \int \int \int_{-\infty}^{\infty} \Phi_u(\mathbf{K}) [1 - \cos(\mathbf{K} \cdot \mathbf{R})] d^3 \kappa. \quad (2.10)$$

In the case where the field is locally homogeneous and isotropic, the structure function becomes a function of the spatial distance  $R$  alone and the vector dot product relationship is removed:

$$D_u(\mathbf{R}) = 8\pi \int_0^{\infty} \kappa^2 \Phi_u(\kappa) \left( 1 - \frac{\sin(\kappa R)}{\kappa R} \right) d\kappa. \quad (2.11)$$

Two important observations of Equation 2.11 can be made. First, the term  $1 - \frac{\sin(\kappa R)}{\kappa R}$  acts as a high-pass filter, removing low spatial frequencies  $K < r^{-1}$ . The structure function removes contributions from scale sizes much larger than the separation through this high-pass filter. [1, 2] Secondly, the structure function allows a singular-

ity at  $\kappa = 0$  of the type  $\kappa^{-\alpha}$ , where  $\alpha < 5$ . [1, 2] The inverse Fourier relationship for the power spectral density is not as straightforward, and the power spectral density function takes the form [1, 2]

$$\Phi_u(\kappa) = \frac{1}{4\pi^2\kappa^2} \int_0^\infty \frac{\sin(\kappa R)}{\kappa R} \frac{d}{dR} \left[ R^2 \frac{d}{dR} D_u(R) \right] dR. \quad (2.12)$$

Atmospheric statistical averages are ensemble averages over a homogeneous and isotropic volume of space. The ensemble averages are both spatial and temporal in nature.  $C_n^2$  is an ensemble parameter and is a second order moment in itself. Spatial properties of the ensemble parameters are transformed into temporal ensemble parameters through the Taylor "frozen flow" hypothesis. This hypothesis states that the temporal variations in an atmospheric volume are produced by advection of the quantities by the mean wind speed throughout that volume rather than by changes in the quantities themselves. [1] This is similar to the advection of slowly changing clouds across the sky. Mean wind speeds drive these clouds across the horizon with little change in the shape of the clouds over small time intervals. Using the Taylor frozen flow hypothesis, spatial statistics are converted to temporal statistics simply by knowledge of the mean wind flow.

Two time scales are of concern in atmospheric statistics. The first are those related to the motion of the atmosphere across the observation path and the other is that arising from the motion of the turbulent eddies. [1, 2] Advection across the observation path is on the order of 1 s, while the eddy dissipation is on the order of 10 s. The eddy dissipation rate is much slower than the advection rate and the turbulent eddies are considered as "frozen" in space and simply moved across the observation plane by the mean wind speed. Ensemble averages are time averages and Taylor's frozen flow hypothesis translates spatial averages into temporal averages. By advecting a spatial parameter temporally, it maintains the ensemble assumptions of homogeneity and wide-sense stationarity. However, pockets of increased turbulence still exist in the atmosphere, and the frozen flow hypothesis breaks down when the

time scale for the turbulent eddies approaches the time scale for the mean advection flow. When this occurs, statistical estimation is difficult, if not impossible, due to the nonlinearities of the random processes in the atmosphere.

### *2.3 Theories of Optical Turbulence Spectra*

Optical turbulence is the result of small fluctuations in the atmospheric index of refraction due to random temperature fluctuations. When temperature and humidity gradients exist within an atmospheric volume, any random turbulent eddies within that volume cause mixing of these gradients and give rise to corresponding gradients in the index of refraction. These index of refraction variations act as random optical lenses on a propagating wavefront, minutely changing the focal length and distorting the resulting wavefront. Research in the 1940s by Andreï Kolmogorov showed that a statistical treatment of random velocity fluctuations provides meaningful insight into optical turbulence, with the condition the field is locally homogeneous and isotropic.

There is a defined regime over which this statistical treatment applies, known as the inertial subrange. The inner scale of turbulence,  $l_0$ , and the outer scale of turbulence,  $L_0$  of the inertial subrange defines the space over which turbulent flow transitions back to laminar flow and all the energy within the eddies is redistributed by viscosity back into the atmospheric volume. This is the Richardson theory of the cascade of energy [18] from large scale sizes to small scale sizes, depicted in Figure 2.1.

Fundamental turbulence theory is based on the assumption the turbulence is weak throughout the inertial subrange. This means the effects experienced during propagation through the medium are phase-only effects. It also requires a sufficiently large coherence range within the inertial subrange to prevent amplitude effects on a propagating beam. If the eddies within a volume are strong enough, the volume is no longer homogeneous and isotropic and weak turbulence theory breaks down. A propagating beam through other than weak turbulence experiences both phase and amplitude effects.

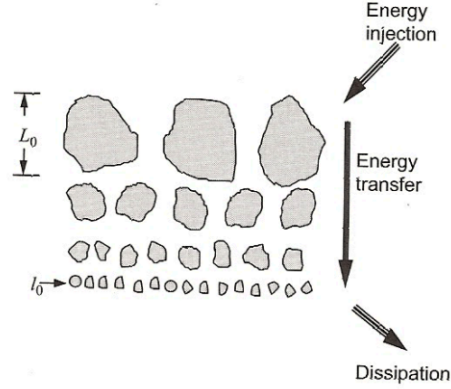


Figure 2.1: Richardson cascade theory of energy. The inner scale of turbulence is denoted by  $l_0$ , while the outer scale is denoted by  $L_0$ . Eddies between the scale sizes of  $l_0$  and  $L_0$  represent the inertial subrange. Energy injected into the atmospheric volume is transferred from eddy to eddy until it is fully dissipated, shown by the arrows. Adopted from Andrews and Phillips, 2006

Kolmogorov's work showed that the velocity structure function obeys a  $2/3$  power law relationship on the magnitude of the vector separation,  $r$ , mainly through the use of dimensional analysis rather than first principles. In three dimensions, the  $2/3$  power law relationship is equivalent to an  $-11/3$  power law behavior on the spatial frequencies. Kolmogorov showed that within the inertial subrange, the power spectrum behaves according to

$$\Phi_n(\kappa) = 0.033C_n^2\kappa^{-11/3} \quad (2.13)$$

where  $\kappa$  is the scalar spatial frequencies in units of rad/m. Equation 2.13 is known as the Kolmogorov power-law spectrum. [1]

Other spectral models extended Kolmogorov's work to account for the effects of the inner and outer scales of turbulence. In order to extend Kolmogorov's power law spectrum into the range of the inner scale of turbulence, known as the dissipation range  $\kappa > 1/l_0$ , Tatarskii introduced a Gaussian function to truncate the spectrum at high wave numbers. [1, 2] The Tatarskii spectrum model,

$$\Phi_n(\kappa) = 0.033C_n^2\kappa^{-11/3}\exp\left(-\frac{\kappa^2}{\kappa_m^2}\right), \quad \kappa \gg \frac{1}{L_0}, \kappa_m = 5.92/l_0 \quad (2.14)$$

accounts for this inner scale region. However, both the Kolmogorov and Tatarskii spectrums have a singularity at  $\kappa = 0$ , and neither are finite for all wavenumbers. This implies the structure function can be calculated but the covariance function cannot. In addition, the power spectrum is isotropic only in the inertial subrange for values of  $\kappa > 1/L_0$ .

In order to extend this theory to finite wavenumbers and to ensure isotropy over all wavenumbers, von Kármán modified the spectrum. [1]

$$\Phi_n(\kappa) = \begin{cases} 0.033C_n^2(\kappa^2 + \kappa_0^2)^{-11/6}, & 0 < \kappa \ll 1/l_0 \\ 0.033C_n^2\exp\left(-\frac{\kappa^2}{\kappa_m^2}\right)(\kappa^2 + \kappa_0^2)^{-11/6}, & 0 \leq \kappa < \infty; \kappa_m = 5.92/l_0 \end{cases} \quad (2.15)$$

Both of these equations are collectively referred to as the von Kármán spectrum. Figure 2.2 shows the Kolmogorov and von Kármán spectrums with the inner and outer scale modifications showing up on the von Kármán spectrum. Other models better characterize the rise, or bump, in the measured spectral data seen at higher wave numbers near  $1/l_0$  (not shown in the figure). The most common of these is the modified Hill spectrum.

#### 2.4 $C_n^2$ and Moments of $C_n^2$

The index of refraction structure constant,  $C_n^2$ , is the quantitative index for the magnitude of optical turbulence. Thermosonde soundings or aircraft measuring devices produce a vertical measurement, while scintillometers measure  $C_n^2$  over short horizontal distances. Studies by Kopeika et al. [13] suggest it is also possible to predict surface  $C_n^2$  values based on local conditions of temperature, relative humidity and wind speed. A thermosonde is a balloon-borne instrument package capable of measuring the temperature structure constant,  $C_T^2$ , along an ascension path. Figure 2.3 shows



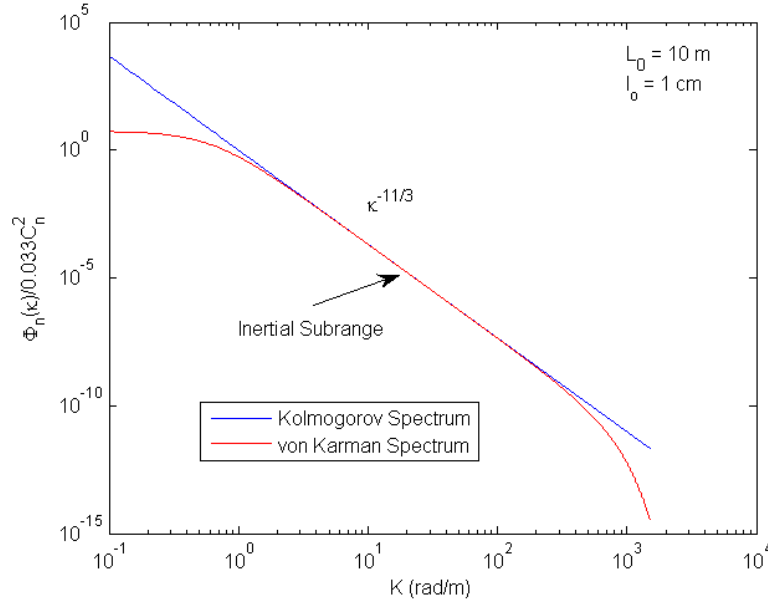


Figure 2.2: Kolmogorov and von Kármán spectral models of refractive index fluctuations. The inner scale of turbulence is 1 cm; the outer scale of turbulence is 10 m. The Kolmogorov spectrum is represented by a classical -11/3 power law. The von Kármán modifications to the Kolmogorov spectrum can be seen in the spectral “roll-off” near the limits of the inertial subrange. The von Kármán spectrum is finite and isotropic for *all* wavenumbers. Reproduced from Andrews & Phillips, 2006

a typical weather balloon-borne thermosonde boom along with a typical vertical  $C_n^2$  profile. Jumper et al. [11,12] showed that the  $C_n^2$  value can be computed directly from these *in-situ* measurements of the temperature structure constant, from the following:

$$C_n^2 = \left[ 79 \times 10^{-6} \frac{P}{T^2} \right] C_T^2 \quad (2.16)$$

where P is the dry-air pressure in hPa and T is the temperature in degrees Kelvin.

$C_n^2$  is a function of altitude, generally decreasing with height above the Earth’s surface, and measured in units of  $m^{-2/3}$ . Values for  $C_n^2$  range from  $10^{-14} m^{-2/3}$  for weak turbulence to  $10^{-12} m^{-2/3}$  for moderate to strong turbulence (surface values). The atmospheric boundary layer, typically defined as the surface to 1.5 km, is the region of the atmosphere most directly influenced by the dynamic exchange of heat

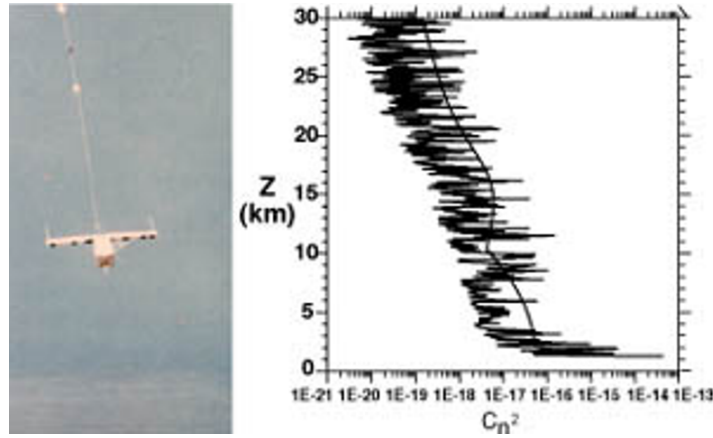


Figure 2.3: Example of a thermosonde payload. This measuring device is carried aloft by a weather balloon, and the airborne instrument package is capable of measuring temperature differentials using fine-wire probes separated by a 1 m distance. Measurements are taken every 7-8 m in the vertical, to an altitude of 30 km above sea level. Thermosonde measurement are normally conducted at night to eliminate the effects of solar radiation on the fine-wire probes. In addition to the temperature measurements, the thermosonde also measures pressure, humidity and horizontal wind velocity. The  $C_n^2$  vertical profile is depicted on the right side of the figure.

from the earth's surface. Within the boundary layer, strong gradients exist due to mechanical mixing and daytime thermal convective activity. Above the boundary layer, known as the free atmosphere,  $C_n^2$  values decrease with height at  $-4/3$  exponential rate. At the capping inversion layer near the top of the boundary layer, strong temperature gradients exist and an increase in the turbulence strength is noted in this region. The strength of turbulence decreases with altitude to approximately a height of 30 km. Above this level, optical turbulence is essentially non-existent and  $C_n^2$  values are typically zero above this altitude.

For a propagation path at some angle,  $\zeta$ , from zenith, the  $C_n^2$  value along the path becomes a function of  $\sec(\zeta)$ . A propagating beam passes through a greater amount of optical turbulence along a slant path than that encountered at zenith angle. The computed path  $C_n^2$  value along a slant path must account for this increased distance through a vertical layer. Any factor depending on the path-integrated  $C_n^2$  value must also assume an angular dependence on the optical turbulence. For example, the long term spot size for a laser beam propagated through turbulence is given by [1]

$$W_{LT} = W \sqrt{1 + 4.35L^{5/6} k^{7/6} \Lambda^{5/6} \int_0^L C_n^2(z) \left(1 - \frac{z}{L}\right)^{5/3} dz} \quad (2.17)$$

where  $W$  is the diffraction limited spot size radius,  $\Lambda$  is the output plane beam diffraction parameter,  $L$  is the propagation distance along the slant path and  $z$  is the incremental propagation distance along the slant path. This is the effective spot size due to turbulence-induced spreading of the propagated beam through a vertical column. The differential distance element,  $dz$ , accounts for the incremental layers across the slant path.

Several moments of  $C_n^2$  describe the atmosphere. The spatial coherence radius,  $\rho_0$ , describes the maximum spatial extent over which the phase of the propagating wavefront remains constant and points along the wavefront remain correlated. For a beam propagating from a source to a distant target,  $\rho_0$  is a measure of the beam spatial coherence after propagating through turbulence. [1, 2, 10] Two points of the wavefront separated by a distance greater than  $\rho_0$  are uncorrelated. Fried's coherence length,  $r_0 = 2.1\rho_0$ , is defined as the atmospheric spatial coherence width for an imaging system. This parameter is more often used to describe the atmospheric coherence length. For the case of a plane wave,

$$r_{0 \text{ pw}} = 2.1 \left[ 1.46 \sec(\zeta) k^2 \int_0^L C_n^2(z) dz \right]^{-3/5} \quad (2.18)$$

where  $k$  is the wavenumber,  $\zeta$  is the angle measured from zenith,  $z$  is the incremental propagation distance and  $L$  is distance from the source to the target. The term,  $\sec(\zeta)$  accounts for the propagation path angle from zenith. Plane wave cases apply to exoatmospheric sources, for example starlight, that enter the earth's atmosphere as a plane wave. [10]. For the case of a spherical wave, representing a point source within the atmosphere, the atmospheric coherence length is defined as

$$r_{0 \text{ sp}} = 2.1 \left[ 1.46 \sec(\zeta) k^2 \int_0^L C_n^2(z) \left(1 - \frac{z}{L}\right)^{5/3} dz \right]^{-3/5} \quad (2.19)$$

The isoplanatic angle,  $\theta_0$  is another moment of  $C_n^2$ . The isoplanatic angle represents the angular distance (from a reference beacon) over which the turbulence is relatively unchanged and is a measure of the coherence angle between two beams. Typical isoplanatic angles are measured in  $\mu$ radians. Figure 2.4 graphically shows the isoplanatic angle and the atmospheric coherence length. The isoplanatic angle is given by,

$$\theta_0 = \left[ 2.91k^2 \sec(\zeta) \int_0^L C_n^2(z)z^{5/3}dz \right]^{-3/5} \text{ rad.} \quad (2.20)$$

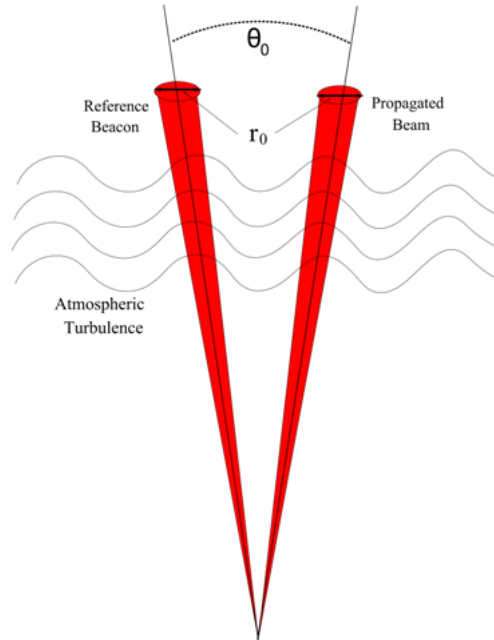


Figure 2.4: Atmospheric coherence length and isoplanatic angle. The atmospheric coherence length,  $r_0$  is the maximum spatial extent over which the propagated wavefront remains correlated. The isoplanatic angle,  $\theta_0$ , is the maximum angular separation over which the turbulence remains unchanged.

The Rytov variance,  $\sigma_\chi^2$ , is a measure of the scintillation in a propagated laser beam. Scintillation is the fluctuation in received irradiance that results from propagation through atmospheric turbulence. It arises from both temporal variations, such as the twinkling of a star, and spatial variations such as laser speckle. The Rytov variance is a second order statistic of the approximation for the Gaussian wave equa-

tion, and is dependent on the propagation distance. The intensity variance of the beam,  $\sigma_I^2$  is approximately  $4\sigma_\chi^2$ , for the weak turbulence regime. For a plane wave, the Rytov variance is defined as [2,10]

$$\sigma_\chi^2(L) = 0.56k^{7/6} \int_0^L C_n^2(z) \left(1 - \frac{z}{L}\right)^{5/6} dz \quad (2.21)$$

and for a spherical wave,

$$\sigma_\chi^2(L) = 0.56k^{7/6} \int_0^L C_n^2(z) \left(\frac{z}{L}\right)^{5/6} \left(1 - \frac{z}{L}\right)^{5/6} dz. \quad (2.22)$$

Fried's parameter, the isoplanatic angle, and the Rytov variance are the primary moments of  $C_n^2$  that describe the atmospheric turbulence.  $C_n^2$  and its moments completely characterize the atmospheric propagation path and the turbulence along that path.

## 2.5 Optical Turbulence Profiles

Weak turbulence theory and the concepts of homogeneity, isotropy, and structure functions led to the development of optical turbulence  $C_n^2$  profiles. Each profile is empirically derived from averaged data, and none of them allow for random  $C_n^2$  profiles. One of the most commonly used turbulence profiles in use is the Hufnagel-Valley 5/7 profile, referred to as HV57. This is a parametric model derived from stellar scintillations and thermosonde measurements. [2]

Using thermosonde measurements, Hufnagel developed a vertical profile model for atmospheric optical turbulence. However, the original profile limited the lower vertical extent to the top of the atmospheric boundary layer. Ulrich, following recommendations by Valley, extended this model to the surface, resulting in the HV57 turbulence profile. [2,9] This model yields vertical  $C_n^2$  values such that the coherence length along the path is 5 cm and the isoplanatic angle is 7  $\mu$ rad for  $\lambda = 0.5\mu\text{m}$ .

Table 2.1: SLC Daytime and Nighttime Models

SLC Day		SLC Night	
$C_n^2(h)$ ( $m^{-2/3}$ )	Altitude (m)	$C_n^2(h)$ ( $m^{-2/3}$ )	Altitude (m)
$1.70 \times 10^{-14}$	$h < 18.5$	$8.40 \times 10^{-15}$	$h < 18.5$
$3.13 \times 10^{-13}/h^{1.05}$	$18.5 < h < 240$	$2.87 \times 10^{-12}/h^2$	$18.5 < h < 110$
$1.30 \times 10^{-15}$	$240 < h < 880$	$2.50 \times 10^{-16}$	$110 < h < 1500$
$8.87 \times 10^{-7}/h^3$	$880 < h < 7200$	$8.87 \times 10^{-7}/h^3$	$1500 < h < 7200$
$2.00 \times 10^{-16}/h^{0.5}$	$7200 < h < 20000$	$2.00 \times 10^{-16}/h^{0.5}$	$7200 < h < 20000$

The HV57 turbulence profile uses the following equation to characterize optical turbulence: [1]

$$C_n^2(h) = 0.00594 \left(\frac{w}{27}\right)^2 (10^{-5}h)^{10} \exp\left(\frac{-h}{1000}\right) + 2.7 \times 10^{-16} \exp\left(\frac{-h}{1500}\right) + A \exp\left(\frac{-h}{100}\right) \quad (2.23)$$

where  $h$  is the altitude in meters,  $w$  is the rms windspeed (m/s) in the range 5-20 km, and  $A$  is a nominal surface  $C_n^2$  value ( $C_n^2(0)$ ) in  $m^{-2/3}$ . For the HV57 standard turbulence profile,  $w$  is 21 m/s and  $A$  is  $1.7 \times 10^{-14} m^{-2/3}$ .

The submarine laser communications (SLC) model is another empirically derived optical turbulence profile, calculated from curve-fitting a piecewise continuous polynomial to measured optical turbulence data. An SLC daytime profile and an SLC nighttime profile exists from the polynomial fit. Data for the these models came from measurements in a subtropical environment (Mt. Haleakala, Maui, Hawaii) and may not be applicable for non-maritime locations. Table 2.1 lists the piecewise polynomial fits of the data. [1, 2, 16] For  $\lambda = 0.5 \mu m$ , the SLC model gives values of  $r_0 = 10$  cm and  $\theta_0 = 12.7 \mu rad$ .

CLEAR I is another commonly used optical turbulence profile created for summer nighttime conditions in the New Mexico desert. This is the primary model used in ABL research. Its primary distinction over the other models is a more pronounced strength in the optical turbulence in the lower atmosphere particularly near the boundary layer. However, this model is not defined for heights below 1230 m

Table 2.2: CLEAR I Night Model

Altitude, $h$ (in km MSL)	$C_n^2(h)$ Coefficients ( $m^{-2/3}$ )
$1.23 < h < 2.13$	$\log_{10}(C_n^2) = 0.814h^2 - 4.3507h - 10.7025$
$2.13 < h < 10.34$	$\log_{10}(C_n^2) = -0.0134h^2 + 0.0335h - 16.2897$
$10.34 < h < 30$	$\log_{10}(C_n^2) = -0.0005h^2 - 0.0449h - 17.0577$ $+ 0.6181 \exp\{-0.5[\frac{(h-15.5617)}{3.4666}]^2\}$

AGL. Augmentation from 1230 m to the surface is necessary if the model is to be used for surface applications. CLEAR I gives values of  $r_0$  and  $\theta_0$  of 5.8 cm and 6.7  $\mu$ rad respectively for  $\lambda = 0.5 \mu$ m. Table 2.2 lists the forms and coefficients of this model. [2,16] Figure 2.5 shows the plots of the HV57, SLC day and night, and Clear I night turbulence profiles.

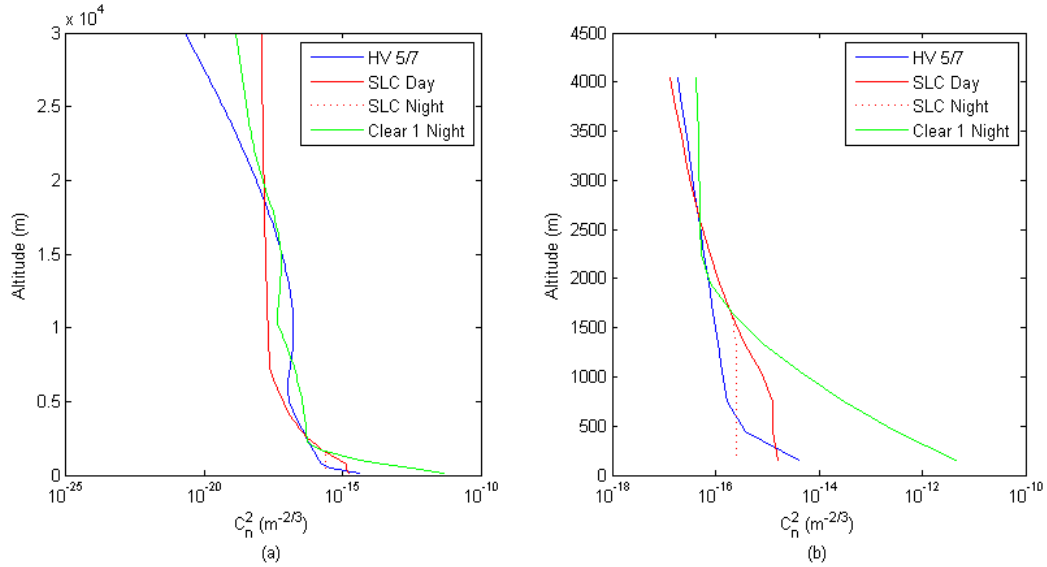


Figure 2.5: Optical turbulence profiles. Subplot (a) shows the model comparison through 30 km. Note the stronger turbulence values of the CLEAR I Night profile in the lower atmospheric regions below the boundary layer. The SLC Day and SLC Night profiles are identical above the boundary layer. The only distinction is the SLC Night has a lower turbulence value below the boundary layer than the SLC Day. The SLC profiles use the HV57 profile for altitudes below 18.5 m. Subplot (b) shows the distinctions in the two SLC models as well as the pronounced strength of the Clear I model below 1230 m.

## 2.6 HELEEOS

HELEEOS is a parametric one-on-one engagement level software model. It was developed by the AFIT Center for Directed Energy and sponsored by the High Energy Laser Joint Technology Office (JTO). [4] It incorporates scaling laws tied to respected wave optics code for laser beam propagation, and integrates all significant atmospheric phenomena such as thermal blooming, aerosol and molecular absorption and scattering, and optical turbulence into its calculations. HELEEOS enables the user to evaluate the uncertainty in low-altitude HEL engagements due to all major clear-air atmospheric phenomena.

HELEEOS utilizes several environmental databases for its computational needs. The Extreme and Percentile Environmental Reference Tables (ExPERT) database contains pre-calculated climatological values for over 400 worldwide sites as well as various land, ocean, and free atmospheric regions. For individual ExPERT sites, this database contains an extensive climatological record of temperature, dewpoint temperature, humidity (relative, absolute and specific), wind, and altimeter settings. The ExPERT database lists these climatological records in the form of probabilities or percentiles of occurrence. These percentiles are the elemental data for the HELEEOS probabilistic climatology  $C_n^2$  profiles. [8]. Figure 2.6 shows all the ExPERT sites currently available globally.

For optical turbulence profiles, HELEEOS accesses the Master Database for Optical Turbulence Research in Support of the Airborne Laser. [4] These vertical optical turbulence profiles were chiefly derived from nighttime thermosonde campaigns at various worldwide sites. A unique characteristic of HELEEOS is a feature known as the Climatological  $C_n^2$  profile. This profile correlates data from the extensive ExPERT climatological database to the Master Database for Optical Turbulence Research. This gives HELEEOS the ability to tailor a probabilistic Climatological  $C_n^2$  profile to a specific land site based on temperature and relative humidity distributions within the ExPERT database.



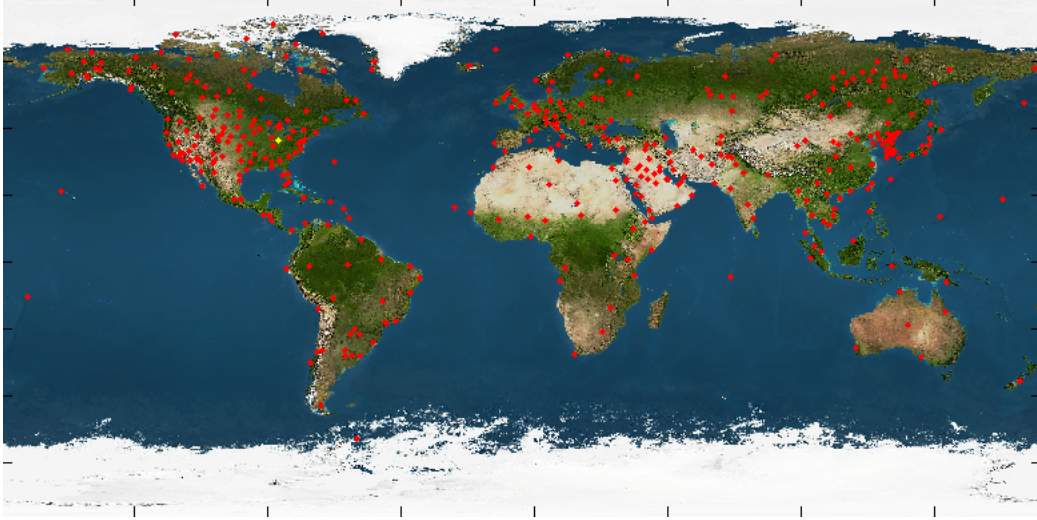


Figure 2.6: Worldwide ExPERT sites. The user can select any of the more than 400 global sites. Each site contains specific climatological data pertinent to that site. Climatological  $C_n^2$  is one atmospheric parameter that can be selected for each site.

Gravelly showed that the distributions of  $C_n^2$  derived from thermosonde campaigns exhibit a log-normal distribution. [8] This agrees well with literature from nighttime experiments that show  $C_n^2$  is log-normally distributed with a standard deviation of 0.5 (dimensionless). [9] A random variable is log-normally distributed if it can be expressed in the form  $\Upsilon = \exp \Psi$ , where  $\Psi$  is a random variable with a normal probability density function (pdf). HELEEOS evaluates the uncertainty in an engagement in the form of a user-defined probability or “percentile of interest” based on these log-normal distributions. There are six separate percentiles available to the user for the Climatological  $C_n^2$  computations: Mode (most frequently occurring), 50<sup>th</sup>, 80<sup>th</sup>, 90<sup>th</sup>, 95<sup>th</sup>, and 99<sup>th</sup> percentiles. Each percentile grouping represents a total area under the curve of the log-normal pdf corresponding to that distinct level. Figure 2.7 shows an example of each percentile.

The ExPERT database provides HELEEOS with surface environmental temperature and relative humidity data for summer and winter seasons used to compute the HELEEOS Climatological  $C_n^2$  turbulence profiles. Currently, HELEEOS only provides Climatological  $C_n^2$  profiles for Desert and Mid-latitude sites for the winter and summer seasons. Each ExPERT site has a probabilistic temperature and relative hu-

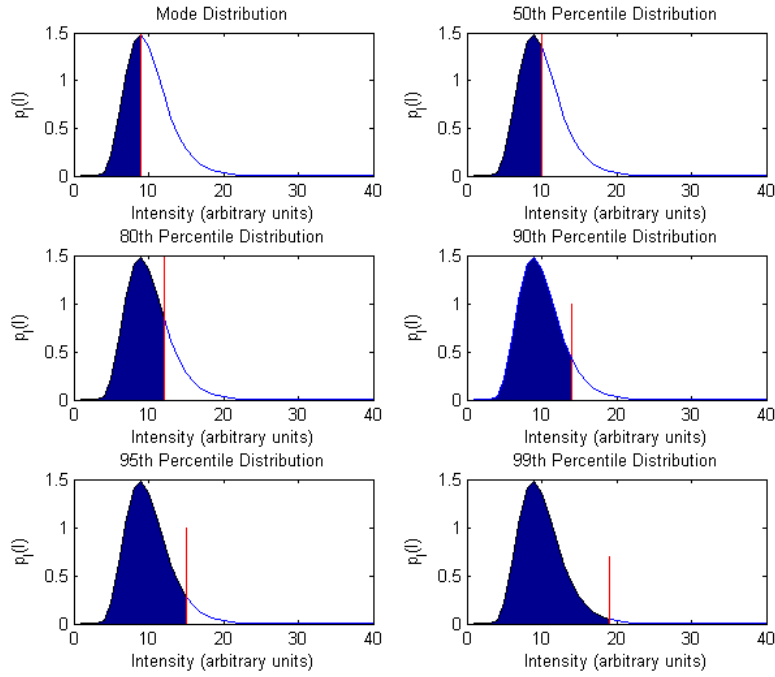


Figure 2.7: Example log-normal distributions and percentiles. The distributions are all log-normally distributed. The shaded area represents the percentile of interest. The mode value is the most frequent value contained in the distribution. The shaded area can be interpreted as containing that percentage of all  $C_n^2$  observations. For example, the 80<sup>th</sup> percentile contains 80% of all  $C_n^2$  observations obtained from the thermosonde soundings. The log-normal distributions were generated using the equation:  $p_I(I) =$

$$\frac{1}{\sqrt{2\pi}I\sigma_I} \exp \left[ -\frac{\left( \ln\left(\frac{I}{\langle I \rangle}\right) + \frac{1}{2}\sigma_I^2\right)^2}{2\sigma_I^2} \right]$$

midity database. For each site, relative humidity probabilities, recorded in the form of observed percentiles, range from the most dry conditions (1<sup>st</sup> percentile) to the most moist conditions (99<sup>th</sup> percentile). However, this climatological history is recorded as hourly annual data rather than seasonal data. This complicates the temperature-versus-relative humidity (Temp-vs-RH) tables HELEEOS uses to compute the Climatological  $C_n^2$  profiles. To overcome this complication, HELEEOS utilizes only one-half of the EXPERT climatological record for each season at each land site. HELEEOS uses the top half of the Temp-vs-RH tables for the summer season, corresponding to warmer temperatures and higher relative humidities, while the bottom half of the

Temp-vs-RH tables serves as the winter season database, corresponding to colder temperatures and lower relative humidities.

It is important to note that the 50<sup>th</sup> percentile corresponds to the average observed meteorological conditions of temperature and relative humidity. However, the 50<sup>th</sup> percentile relative humidity does not mean 50% relative humidity, as is often assumed. The 50<sup>th</sup> percentile data are time-averaged observed relative humidities and temperatures at each given site. For example, in a desert climate, the average (50<sup>th</sup> percentile) relative humidity may very well correspond to observed relative humidities much less than 50%.

HELEEOS computes both the temperature and RH pdfs for land sites, ocean sites, and upper air regions. The land site surface temperature and RH pdfs are well-correlated based on many years of hourly climatological history. The upper air and ocean sites, on the other hand, are not as well correlated since they rely on bi-daily radiosonde (weather balloon) reports or sporadic weather reports from ships and aircraft. As a result, the surface land site temperature and relative humidity pdfs provide more meaningful data in computing Climatological  $C_n^2$  profiles, and HELEEOS restricts the Climatological  $C_n^2$  profiles to land sites only. However, there is also an underlying assumption that the atmospheric boundary layer can be characterized by its surface parameters. This is a reasonable assumption since research has shown that a well-mixed boundary layer is nearly homogeneous in its potential temperature (the temperature a parcel would have if it were brought adiabatically to a pressure of 1000 hPa), moisture, pollutant/aerosol content and wind speed. [4] The typical, fair weather afternoon boundary layer extends vertically to an altitude about 1.5 km above the surface. HELEEOS defaults the vertical extent of the daytime, or diurnal, atmospheric boundary layer to 1524 m (5k ft). The boundary decreases with the loss of solar radiation and convective mixing to approximately 500 m above the earth's surface during the nighttime, or nocturnal, hours. The default value for the nocturnal boundary layer is 500 m. During the periods of transition such as mid-morning or

early evening when the boundary layer is rising or lowering, the default boundary layer value in HELEEOS is 1000 m.

The ExPERT database correlated temperature and relative humidity pdfs (assuming a homogeneous boundary layer) and the Master Database for Optical Turbulence Research are the primary constituents used to compute the Climatological  $C_n^2$  profiles. In order to compute a vertical Climatological  $C_n^2$  profile, HELEEOS divides the atmosphere into the two distinct layers - the boundary layer and the free atmosphere. Within the boundary layer, HELEEOS correlates (or "bins") the Climatological  $C_n^2$  value to the relative humidity pdfs; in the free atmosphere the binned values correspond to temperature correlations. Relative humidity was chosen as the boundary layer meteorological correlation parameter because relative humidity plays a key role in the growth and scattering effects of aerosols, which in turn can have a pronounced effect on the strength of the optical turbulence. Recent research shows that  $C_n^2$  exhibits an inverse relationship with relative humidity in the absence of solar insolation. [5] Thus, correlating  $C_n^2$  to a relative humidity bin is more appropriate within the boundary layer, and the user-defined percentile of interest corresponds directly to a boundary layer relative humidity value.

HELEEOS subdivides the atmospheric boundary layer into two distinct sub-layers. The first layer, the surface layer, extends from the surface through 60 m. The next vertical volume extends from 60 m to the top of the boundary layer. Recall the HELEEOS boundary layer is 1524 m during the day, 500 m during the night, and 1000 m at transition periods. Within these layers, HELEEOS uses Climatological  $C_n^2$  values correlated to the relative humidity pdfs for the site climatology. The Climatological  $C_n^2$  look-up tables bin optical turbulence values according to the relative humidity percentages (not percentiles). The site climatology establishes the basis for the user-defined relative humidity percentile. For example, if the user chooses the 50% - Average RH percentile, and for a given site this 50<sup>th</sup> percentile corresponds to an average 65% relative humidity, HELEEOS correlates the Climatological  $C_n^2$  turbulence

value with the 65% relative humidity bin. Probabilistic climatology then becomes the foundations of the Climatological  $C_n^2$  profiles, a feature solely unique to HELEEOS.

For the free atmosphere, HELEEOS produces a Climatological  $C_n^2$  profile using correlated standard atmosphere temperature pdfs. The free atmosphere, like the boundary layer, is subdivided into several layers. These layers correspond to the standard atmosphere layers: every 1k ft from 1k-10k ft, every 2k ft from 10k-20k ft, every 5k ft from 20k-50k ft, and every 10k ft from 50k-100k ft. HELEEOS provides a site-tailored Climatological  $C_n^2$  profile through 24 km (approximately 78k ft). There is also a region of overlap between the free atmosphere and the boundary layer. Near the top of the boundary layer (day, night or transition periods), HELEEOS uses an extension of the free atmosphere upper air temperature pdfs to prevent sudden discontinuities in the turbulence profile. These discontinuities arise from Climatological  $C_n^2$  value differences between where the boundary layer Climatological  $C_n^2$  turbulence values end and the free atmosphere Climatological  $C_n^2$  turbulence values begin. In the free atmosphere, HELEEOS matches Climatological  $C_n^2$  values to corresponding standard atmosphere temperatures to complete the Climatological  $C_n^2$  turbulence profile through 24 km.

To calculate a vertical Climatological  $C_n^2$  profile, HELEEOS first requires a relative humidity percentile and a user-defined turbulence percentile obtained through user selection on the HELEEOS Atmospheric graphical user interface (GUI). HELEEOS has nine user selectable relative humidity percentiles ranging from the 1<sup>st</sup> percentile to the 99<sup>th</sup> percentile, and six Climatological  $C_n^2$  turbulence profiles ranging from the Mode to the 99<sup>th</sup> percentile. The default relative humidity percentile in HELEEOS is the 50<sup>th</sup> percentile, or average conditions and the default Climatological  $C_n^2$  turbulence percentile is the Mode value. HELEEOS then accesses the ExPERT database for the climatological record at the user defined relative humidity percentile, and from this HELEEOS physically correlates this value to a binned Climatological  $C_n^2$  value in the Master Database for Optical Turbulence Research. Values in the Master Database for Optical Turbulence Research database are calculated from the log-normal distribu-

tions from a limited set of measured thermosonde data. The user-defined turbulence percentile of interest determines the values extracted from these look-up tables.

Within the boundary layer, each relative humidity percentile is also cross-referenced to a corresponding temperature percentile. From the temperature and relative humidity, HELEEOS calculates a dew point at each location in the profile. The temperature and dew point are lapsed through the boundary layer at the standard adiabatic lapse rates of 6.5 °C/1000 m for saturated atmospheres or 10 °C/1000 m for dry atmospheres. At each defined altitude, HELEEOS recalculates the relative humidity, based on the relationship between the lapsed temperature and dewpoint, and extracts a value from the look-up tables for the user defined turbulence percentile. The relative humidity percentiles remain constant (99<sup>th</sup> percentile) if the temperature and dewpoint curves reach saturation within the boundary layer.

In the free atmosphere, HELEEOS uses correlated temperatures determined from upper air standard atmosphere temperature curves. HELEEOS selects values from the look-up tables at each standard atmosphere altitude and interpolates between these points. Figure 2.8 shows an example of a Climatological  $C_n^2$  vertical profile. Notice that HELEEOS provides an "envelope" of profiles, depicted by the span of the 3 distinct profiles. Thus, HELEEOS not only tailors the Climatological  $C_n^2$  profile to a specific site, it also provides a range of optical turbulence profiles. This is unmatched by empirical models.

The Climatological  $C_n^2$  values for ExPERT Desert sites originated from thermosonde data collected in the Middle Eastern campaigns for Saudi Arabia, Qatar, and Bahrain. This collection of summer and winter thermosondes form the foundation of the all other desert sites within HELEEOS. Likewise, the Mid-latitude summer and winter Climatological  $C_n^2$  look-up tables originated from a limited set of thermosonde campaigns conducted at Osan, South Korea. This dataset forms the basis for all mid-latitude Climatological  $C_n^2$  profiles in HELEEOS.

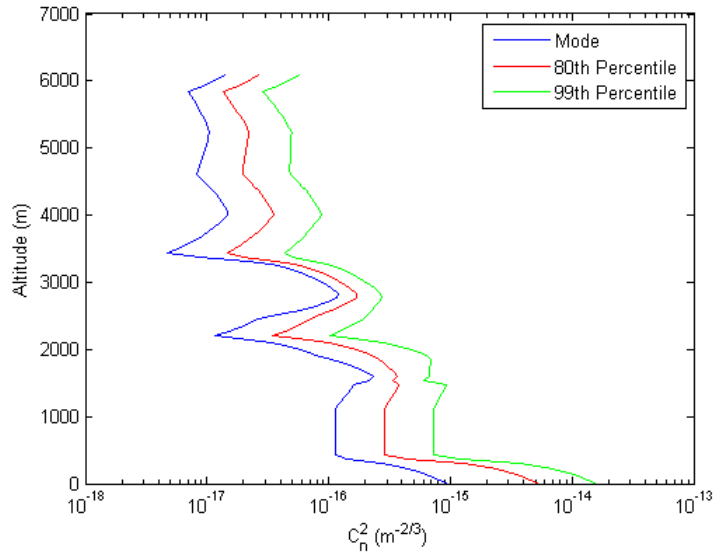


Figure 2.8: Example Climatological  $C_n^2$  profiles for Wright-Patterson AFB, OH. Three user-defined percentiles of interest are shown: Mode, 80<sup>th</sup>, and 99<sup>th</sup> percentile. The relative magnitude of the Climatological  $C_n^2$  profiles increases as the percentiles of interest increase. This is expected, since the 99<sup>th</sup> percentile encapsulates 99% of all  $C_n^2$  measurements within one standard deviation.

This methodology, while very different from empirical methodologies, produces  $C_n^2$  profiles that match well with observed thermosonde soundings. Figure 2.9 shows how the HELEEOS Climatological  $C_n^2$  profile is a very good representation of the true turbulence within an atmospheric volume, for a sample thermosonde from Vandenberg AFB, CA. Also plotted is the Hufnagel-Valley 5/7 turbulence profile. The HELEEOS Climatological  $C_n^2$  profile is a summer profile produced from the Mode turbulence percentile, average relative humidity, and a 500 m boundary layer (night-time). HELEEOS closely replicates the observed random  $C_n^2$  fluctuations along the vertical path. The HV57 profile completely misses these subtle changes in the vertical column due to its empirical nature. This is typical of all the HELEEOS Climatological  $C_n^2$  turbulence profiles, and makes these probabilistic Climatological  $C_n^2$  profiles a very useful tool for forecasting the strength of optical turbulence along a vertical path.

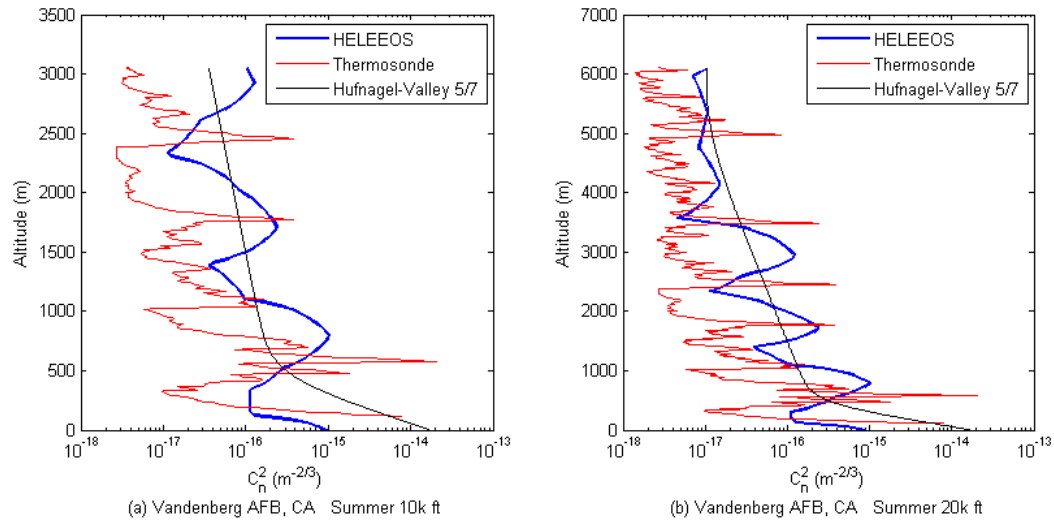


Figure 2.9: HELEEOS Climatological  $C_n^2$  and thermosonde profiles for Vandenberg AFB, CA.

This thesis focuses on the path-integrated values of the Climatological  $C_n^2$  profiles for the Mode and 50<sup>th</sup> percentiles of interest. Path-integrated values comprise the total strength of the optical turbulence over the propagation path. Observed nominal path-integrated  $C_n^2$  values are in the range  $10^{-13} \text{ m}^{-2/3}$  to  $10^{-12} \text{ m}^{-2/3}$  for a 3048 m (10k ft) vertical path length, and  $10^{-12} \text{ m}^{-2/3}$  for a 6096 m (20k ft) vertical path.

## 2.7 Design of Experiments

Design of experiments (DOE) is a test methodology that ensures the test data collected throughout an experiment is statistically useable, and that the conclusions supported by the data are valid and objective. [17] Statistical methods increase the efficiency of an experimentation and often bolster the conclusions supported by the experimental data. DOE techniques uncovers hidden interactions revealing dependencies of the process that would otherwise go unnoticed. This powerful design and analysis tool is used extensively throughout the engineering and scientific communities.

The atmosphere, and specifically optical turbulence, is a random process, and as such can be analyzed from a statistical vantage, as shown in Sections 2.2 and 2.3.



$C_n^2$  is also a random variable in the atmosphere, depending on the randomly distributed temperature gradients within a volume of space. It makes sense to design an experiment for measuring  $C_n^2$  with an increased emphasis on statistical analysis.

There are two main aspects to any DOE experimental approach: the design of the experiment and the statistical analysis of the data. A repeatable design is critical to data collection, but the execution of the design must invoke some measure of randomness. Randomness ensures the error, more appropriately the noise, in a measurement is not a function of a step-by-step approach to data collection. In addition, the experiment must also be capable of accounting for nuisance factors that are insignificant to the experiment but that may induce variations in the data. The statistical analysis of the data must be robust and must be capable of identifying interactions among the test factors within the data.

A random variable can be discrete or continuous. The pdf and its moments completely describe the random variable or process. The first two moments of the pdf, the mean and the variance, are extremely important to the statistical analysis of a random variable. These two moments are essential to the science of expectation and probability theory. [14, 24] Let  $p_x(x)$  be the pdf of a discrete random variable,  $x$ . The first moment, the mean, of the random variable is given by

$$\mu = \sum_{\text{all } k} x_k p_x(x_k) , \quad (2.24)$$

and the second moment, the variance, is given by

$$\sigma^2 = \sum_{\text{all } k} (x_k - \mu)^2 p_x(x_k). \quad (2.25)$$

The mean and variance of a sample set are often used in an experiment as a statistical representation of the entire population. If a sample set of the population is used, the sample mean is defined as

$$\bar{x} = \frac{1}{n} \sum_{i=1}^n x_i , \quad (2.26)$$

and the sample variance is defined as

$$s^2 = \frac{1}{n-1} \sum_{i=1}^n (x_i - \bar{x})^2 . \quad (2.27)$$

The sample mean is a point estimator of the population mean,  $\mu$ , and the sample variance is a point estimator of the population variance,  $\sigma^2$ . [17]

An essential component of DOE is the factorial design. Factorial designs allow for thorough examination of the effects of two or more factors within an experiment. Full factorial design refers to a complete design experiment in which all possible combinations of the levels of the factors are realized and investigated. If, for example, factor A has  $\alpha$  levels or variations, and factor B has  $\beta$  levels, there are a total of  $\alpha \cdot \beta$  combinations that can be realized. A full factorial design realizes all of these  $\alpha\beta$  combinations. Partial factorial designs (half-fraction or quarter-fraction factorial designs) realize only the critical factors, but still provide the insight into factor interaction that the full factorials give. Thus, a DOE designed experiment provides the ability to realize a full test with only a fraction of the full  $\alpha \cdot \beta$  combinations, oftentimes saving both time and money.

The effect of a factor is defined as the change in the realization produced by a variation in the levels of the factor. It is referred to as a "main effect" when it is a primary factor of interest in the experiment. Consider a two-factor factorial design experiment shown in Figure 2.10. Each of the two factors have two levels, denoted by Low (-) and High (+). The main effect of factor A is the average change in the response from the high level to the low level. Numerically this is

$$\text{main effect of factor A} = \frac{21 + 77}{2} - \frac{14 + 35}{2} = 24.5 . \quad (2.28)$$

The main effect of increasing factor A from the low level to the high level results in an average response change of 17.5 units. Similarly for factor B,

$$\text{main effect of factor B} = \frac{35 + 77}{2} - \frac{14 + 21}{2} = 38.5 . \quad (2.29)$$

An interaction between the factors occurs when the difference in response between the levels of one factor is not the same at all levels of the other factors. [17] In the case of Figure 2.10(b), the effect of factor A at the low level of factor B is

$$A = 77 - 21 = 56 \quad (2.30)$$

and the effect of factor A at the high level of factor B is

$$B = 14 - 35 = -21 . \quad (2.31)$$

The effect of A depends on the level chosen for factor B indicating there is an interaction between factors A and B. The magnitude of the interaction is the difference between the two A effects ( $AB = (-21-56)/2 = -38.5$ ). Figure 2.11 illustrates this graphically. In (a), the lines do not intersect indicating there is no interaction between the factors over the specified range. In (b), there is clearly an interaction between the factors, seen by the crossed lines in the graph.

Partial factorial designs offer the advantage of designing an experiment in such a way that fewer realizations are required (often less than all of the  $\alpha\beta$  combinations) while gaining most of the same insight into the factor interactions. Efficiency in time and data collection over a one-factor-at-a-time realization method increases as the number of factors increase.

The DOE statistical model exhaustively analyzes the error within the data through the Analysis of Variance (ANOVA). The main sources of error are the variances, from an expected value, associated with each data element of the test and are known as residual errors. Residual error is the noise error found in the experiment. A

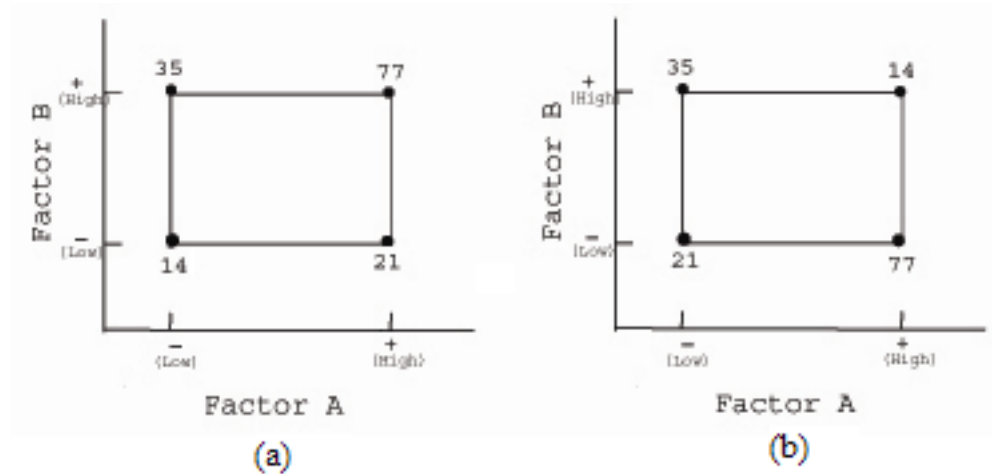


Figure 2.10: A two-factor factorial design. The figure on the left is a factorial design without interactions. The figure on the right is a factorial design with interactions. Adapted from Montgomery, 2006

level of significance value, referred to as the  $\alpha$  value, is determined prior to the DOE analysis. This  $\alpha$  value is the error arising from the hypothesis testing of the data, and is the overall significance level of the test. Errors in hypothesis testing assume two basic types, Type I and Type II error. Type I error,  $\alpha$ , is the error injected into the analysis if the basic, or null, hypothesis is rejected when it is actually true. For example, if the null hypothesis is  $\mu_1 = \mu_2$  and the data leads to rejection of this hypothesis, Type I error is created if the claim  $\mu_1 \neq \mu_2$  is made and the null hypothesis is rejected when it is actually true. Generally, this type of error is the most significant error in any test and committing a Type I error often invalidates the test. The goal is to make the  $\alpha$  value as small as possible to reduce the probability of this critical error occurring. Type II error, the  $\beta$  value, arises when the analysis fails to reject the null hypothesis when it is false. For the example, Type II error occurs if the hypothesis is  $\mu_1 = \mu_2$  and this hypothesis is substantiated while it is in fact false. Both are gross test errors, but the criticality of the error depends on the amount of risk involved in committing each type of error. Typically, the  $\alpha$  value is held low and the test is designed so that the probability of Type II error  $\beta$  occurring is reasonably low.

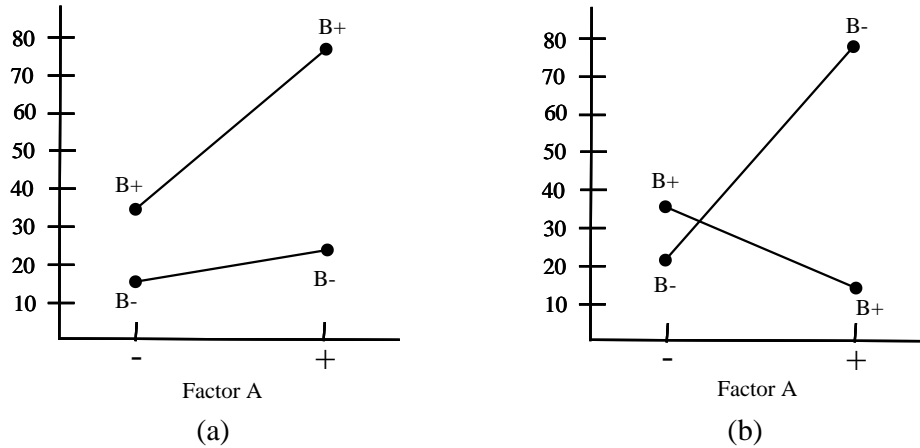


Figure 2.11: A two-factor factorial design. The figure on the left is a factorial design without interactions. The figure on the right is a factorial design with interactions. The crossed lines in (b) indicate interactions between Factor A and Factor B. Adapted from Montgomery, 2006

A p-value test is required to determine if the errors within the test are causal, or significant sources of error. The p-test is the probability that the resultant test statistic will take on a value that is as extreme as the observed test statistic when the null hypothesis is true. This test correlates a specific value to a test statistic, main effect or interaction, in relation to its causal factors. It conveys information about the weighting of the justification to reject the null hypothesis. The p-value test can be thought of as the smallest level of significance,  $\alpha$  at which the data becomes significant enough to reject the null hypothesis. When these p-values are very low, the data are very significant and the error is directly attributed to the causal factors. Low p-values provide sufficient justification for upholding or rejecting the null hypothesis based on the given test factor. The intuition here is that any change in the data can be directly attributable to the causal test factors.

Validation of the DOE statistical model is required before analyzing the results of a DOE designed test. This ensures the statistical model is complete and thorough and that the results of the test are accurate. The DOE statistical analysis model has three basic assumptions to ensure model completeness: the samples are independent, residual errors are normally distributed with zero mean and the residual variances in

each cell are equal. A fourth assumption is that the model is adequate, an assumption met if the other three assumptions are also met. These assumptions require the data to be independent, normally distributed data  $NID(0, \sigma^2)$ . Each of these assumptions must be satisfied or the results of the DOE experiment will be in error.

Usually, independence is satisfied through proper test conduct and data collection methodology. The second assumption for this test model is that these residual errors are normally distributed with zero mean. If the residuals are not normally distributed, data transformation is required to satisfy this assumption. Data transformation removes dependencies within the data and ensures data normality. In this test, the  $C_n^2$  values are lognormally distributed and require data transformation to satisfy this assumption. The logarithmic transformation removes the lognormal distributions within the data and ensures normal distribution of the data  $NID(0, \sigma^2)$ .

The variances of the residuals must also be equal, although these variance do not have to be known. This assumption relates to the randomness of the test. For example, if a test was conducted with an operator in the loop, the variances in the early part of the test may be greater as the operator learns the equipment. Increased variances at the end of a test may indicate operator fatigue. Randomness in the test ensures these outside factors do not influence the test. If randomness is designed into the test then any variations are due to the data and not these outside influences. The statistical model is considered complete if all three assumptions have been met.

Graphical validation of the statistical model is made through the use of normal probability plots and histogram plots of the residual errors. These residual errors are defined by

$$e_i = y_i - \hat{y}_i \quad (2.32)$$

where  $y_i$  is the  $i^{th}$  observation or data element, and  $\hat{y}_i$  is the point estimator of the observation as determined from the regression model. In a normal probability plot, the residuals lie along a line of correlation. In a histogram plot, the data exhibit

the classical appearance of a normal data distribution. If the data are normal, then approximately 68% of the residuals lie within one standard deviation and approximately 99% of the residuals fall within three standard deviations. After the analysis is conducted, the data are untransformed (if transformation was required) to the form of the original data, in this case, the lognormal distribution.

Several texts abound on the topic of DOE statistical analysis and the reader is encouraged to explore these works to gain further insight into the fundamentals of DOE.

## III. Research Methodology and Data

### 3.1 Chapter Overview

The purpose of this chapter is to outline, in detail, the research methodology used for this thesis and to describe the data used to conduct that research. The generalized test approach is discussed in Section 3.2. This section outlines the approach of comparing HELEEOS Climatological  $C_n^2$  profiles to measured thermosonde profiles. Section 3.3 provides insight into terminology used throughout the thesis. The terminology is confusing at times, and this section provides definition of those terms. Section 3.4 deals specifically with the thermosonde test methodology and test data. This section discusses the validation of each thermosonde and the locations of the campaigns used. Section 3.5 presents the HELEEOS test methodology and test data. This section covers EXPERT site selection and the two HELEEOS datasets used in the test. It also discusses the use of the ATMTools<sup>®</sup> software package. Finally, Section 3.6 presents the detailed DOE test design and methodology. It identifies all test factors used in the design matrix, as well as sample design matrices.

### 3.2 Generalized Test Approach

This thesis focuses on path-integrated  $C_n^2$  values that are pertinent to mid-tropospheric HEL applications such as the ATL. Three operational flight altitudes comprise the path for this platform: 5k (1524 m), 10k (3048m) and 20k (6096m) ft. The path is defined as the surface through each orbit altitude, and path-integrated  $C_n^2$  values come from these vertical layers. The objective is to ascertain 80% confidence bounds on the path-integrated Climatological  $C_n^2$  profiles for these altitudes, based on typical operational requirements. These confidence intervals provide a span of optical turbulence ranges to assess system performances or for use in research endeavors.

The data come from two primary sources: HELEEOS and thermosonde campaigns. HELEEOS is used to calculate the Climatological  $C_n^2$  profiles, while the thermosonde data comes from actual thermosonde campaigns conducted at various locations worldwide. The thermosonde data are used as truth data for comparison



purposes to HELEEOS. Table 3.1 lists the locations of the thermosonde campaigns and the corresponding ExPERT site used to generate the Climatological  $C_n^2$  profile in HELEEOS. The ExPERT sites chosen were those in closest proximity to the location of the thermosonde launches.

Table 3.1: Locations of Thermosonde Campaigns and Nearest ExPERT Site

Thermosonde Location	ExPERT Site Location
Adelaide, Australia	Adelaide Airport, Australia
Bahrain	Bahrain Intl Airport
Doha, Qatar	Abu Dhabi Intl Airport
Gap, France	Paris, France
Holloman AFB, NM	Holloman AFB, NM
Vandenberg AFB, CA	Vandenberg AFB, CA
Osan AB, South Korea	Pyongtaek, South Korea
Riyadh, Saudi Arabia	Riyadh, Saudi Arabia
Sirene Observatory, France	Paris, France
Three Rivers, CA	Fairfield/Travis AFB, CA

Comparison is made between each HELEEOS Climatological  $C_n^2$  path-integrated turbulence profile (for the “nearest” ExPERT site) to the measured thermosonde  $C_n^2$  path-integrated turbulence profile for each of the three defined operational altitudes. A path-integrated optical turbulence value is the sum of all  $C_n^2$  values multiplied by the differential heights at each point along the path. Mathematically, this is represented by

$$Path\ integrated\ value = \int_0^L C_n^2 dz \quad (3.1)$$

where L is the orbit altitude and z is the differential vertical layer depth.

These path-integrated values are the basis for the DOE experiment. Rigorous DOE analysis, particularly through a rigorous ANOVA, can reveal any hidden interactions within HELEEOS that are affecting the overall performance of Climatological  $C_n^2$  profiles. In addition, the DOE test places confidence bounds on these path-integrated values, which is the goal of this thesis.

The strength of the optical turbulence along a vertical path increases within the boundary layer where the greatest exchange of heat occurs between the earth and the atmosphere above it. The sfc-5k ft altitude encompasses all possible HELEEOS boundary layers of this important earth-atmosphere interaction. In terms of a path integration, this region encapsulates the majority of the path optical turbulence. The remaining altitudes closely mirror the 5k ft path-integrated value, but the main contributor to the path-integrated sum is that region between the surface and 5k ft.

DOE analysis identifies any interactions within the data. Some interactions are expected. For example, the factors of season, Summer or Winter, with climate, Mid-latitude or Desert, will have strong interactions since they determine selection of an ExPERT location. However, unexpected interactions might surface that have causal effects, and the DOE experiment draws these interactions out. If these interactions prove to be problem areas they can be identified and solutions sought out as well.

### ***3.3 Terminology***

It is important to define the terminology used throughout this thesis. The most confusing term used in this thesis may be "boundary layer." In terms of atmospheric, this is the region most influenced by dynamic heat exchange between the surface and the atmosphere above it. By convention, the atmospheric boundary layer is 1524 m during daytime conditions and 500 m during nighttime conditions. There are three HELEEOS boundary layers - 1524 m, 1000 m and 500 m - each corresponding to a particular user-defined time-of-day. In majority cases, a reference to the boundary layer indicates the HELEEOS boundary layer. In all other instances, the atmospheric boundary layer is specifically referenced. In addition, the 1524 m HELEEOS boundary layer may be referred to as the daytime boundary layer and the HELEEOS 500 m boundary layer referred to as the nighttime boundary layer. Any references to the daytime boundary layer specifically indicate both an atmospheric and HELEEOS boundary layer of 1524 m. Likewise, any references to a nighttime boundary layer identifies both an atmospheric and HELEEOS boundary layer of 500 m.

Use of the term "percentiles" is also confusing. HELEEOS has percentiles for both turbulence (mode through 99<sup>th</sup> percentile) and relative humidity (1<sup>st</sup> through 99<sup>th</sup> percentile.) References such as "50<sup>th</sup> percentile turbulence profile, 50<sup>th</sup> percentile relative humidity" quickly become confusing. It is important the reader acknowledge the dual usage of the term percentile to both turbulence and relative humidity. It is also important to distinguish between the two when this common term is used.

The HELEEOS boundary layer is also dependent upon a user-defined time of day. There are nine time-of-day selections available in HELEEOS - eight 3-hour time blocks and a daily average selection. The daily average selection corresponds to the daily average temperature, and a boundary layer value of 1524 m. Daily average time-of-day is the default selection in HELEEOS. The time-of-day hours of 00:00 - 06:00 local time are the nighttime hours (500 m boundary layer), and the time-of-day hours of 09:00 - 21:00 local time are the daytime hours (1524 m boundary layer). Usage of the term "nighttime" or "daytime" infers a variety of factors, and it is important to understand these combinations of factors.

Finally, altitudes in this thesis have units of both meters and feet. For all  $C_n^2$  vertical profile plots, the altitudes are in meters. The boundary layer is always given in units of meters. However, the altitudes of interest in this thesis are given in terms of feet. Aircraft operating altitudes are defined in terms of thousands of feet and this convention is used here as well. In addition, a variety of altitude combinations exist. For example, a chart may show results for the three operating altitudes (in kft) as a function of both the 500 m and 1524 m boundary layers. It is important the reader understand this convention when referencing the Figures in Chapter 4.

### ***3.4 Thermosonde Data***

The thermosonde data used in this research effort originated from campaigns at various worldwide locations. The Air Force Research Laboratory's Air and Space Vehicles Directorate, Atmospheric Data Acquisition/Archival Systems Branch (AFR-L/VSBYA) at Hanscom AFB, MA, provided all the thermosonde data used in this

effort, courtesy of Dr. George Jumper and Lt John Meyers. Thermosonde data existed for the ten sites listed in Table 3.1. The thermosonde campaigns for Holloman AFB, NM and Vandenberg AFB, CA originated at the Airborne Laser Systems Program Office. AFOSR conducted the international campaigns at Gap, France and Adelaide, Australia, as well as at Three Rivers, CA. Figure 3.1 shows a sample thermosonde profile from Holloman AFB, NM.

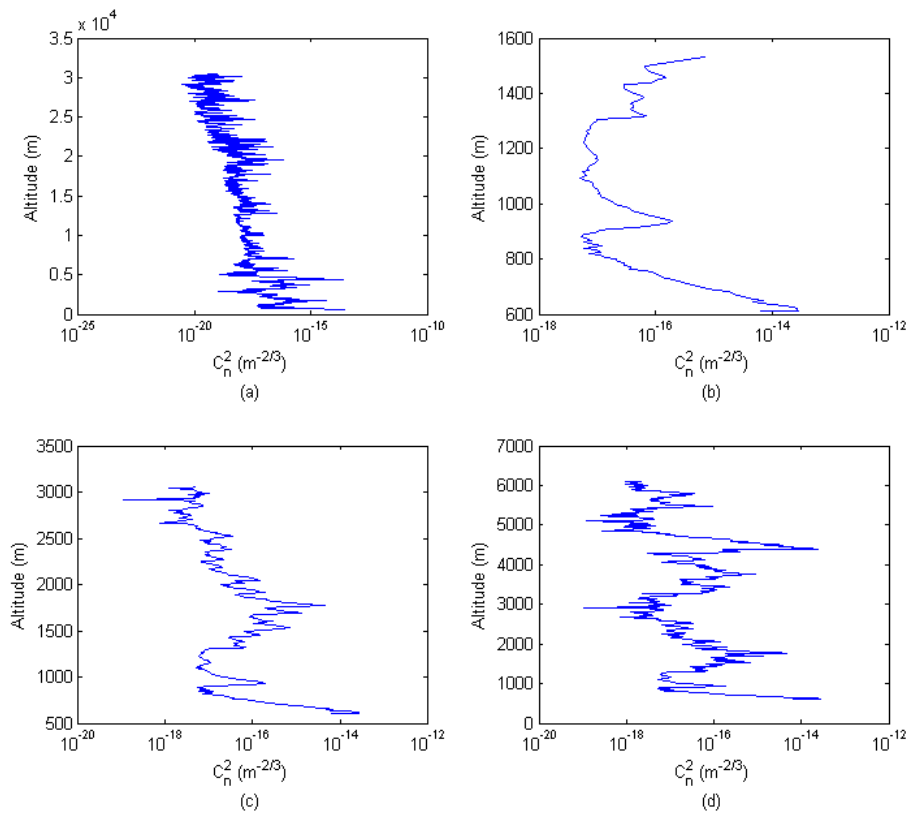


Figure 3.1: Vertical  $C_n^2$  profiles of an actual thermosonde flight launched from Holloman AFB, NM. The complete vertical profile of the launch is shown in (a), while the 5k ft, 10k ft and the 20k ft vertical profiles are shown in (b), (c) and (d) respectively. The elevation was 609 m. Note the large variations in the magnitude of the optical turbulence along the ascension path. Increasing temperature gradients and stronger optical turbulence are observed at the top of the boundary layer near 1800m, and at 4300m, possibly created by mountain wave activity in the vicinity of launch.

Each thermosonde flight data consisted of measured observations of altitude (in m mean sea level, MSL), pressure, temperature, relative humidity, and  $C_n^2$  taken

every 7-8 m from the surface through a vertical extent of approximately 30 km. In addition, each flight contained several other computed parameters based on these measurements. Each flight contained either 14 or 15 columns of observed measurements, depending on the particular campaign. The delineating factor for each row of raw observed data was the altitude measurement.

The raw thermosonde measurements required validation prior to inclusion as test data. In many cases the measurements had missing data elements, which defaulted to values of "-999." Retention of these flights depended on the measured parameter. For example, if the faulty data were with the measured pressure, the flight became part of the dataset. However, if the faulty data were  $C_n^2$  measurements, and the vertical depth of the missing data exceeded 200 m, it was discarded and not used in this test. If retained, the faulty data elements were zeroed to prevent calculation errors. In some cases the thermosonde measurement devices either failed after launch for several hundred meters or failed during a portion of the flight ascension path, after which data readout began. Data verification for these flights depended on the location of the missing data blocks and the depth of the vertical layer of missing data. The deciding factors were greater than 200 m of vertical depth and an altitude of 3048 m. If the missing vertical depth occurred below 3048 m the flights were discarded.

Observed thermosonde parameters used in the course of this research were altitude, pressure, temperature, relative humidity and  $C_n^2$ . All raw measurement data were imported into Matlab<sup>®</sup> and only the necessary data stripped off. All other data columns were disregarded.

Thermosonde data existed for various summer and winter campaigns. In some cases, several summer or winter campaigns existed for the same site. Each season had a matching ExPERT season in HELEEOS. Some campaigns also recorded data from spring and fall campaigns. Specific climatological assumptions were made for these seasons that did not correspond to an ExPERT summer or winter season. Twenty-three Vandenberg AFB, CA fall flights, collected from 18-25 October, and deemed

representative of a summer atmosphere by comparisons of the surface temperature and relative humidity to the summer climatological record, became a representative summer dataset. The Three Rivers, CA campaign, conducted from 20 March - 5 April, formed a representative winter dataset for surface temperatures correlated with the winter climatological temperature of 7.25 °C. The Holloman AFB, NM summer dataset consisted of three merged campaigns forming one ensemble of 63 flights.

Table 3.2 shows the seasonal thermosonde data available for each site and the total number of flights, or the sample size, available for each campaign. No thermosonde data existed for the following site and season combinations: Adelaide, Australia (summer), Bahrain (winter), Three Rivers, CA (summer), Vandenberg AFB, CA (winter), Gap, France (winter) or Sirene Observatory, France (winter).

Table 3.2: Seasonal Thermosonde Campaigns

Site Location	Seasons Available	Number of Flights
Adelaide, Australia	Winter	20
Bahrain	Summer	46
Doha, Qatar	Summer, Winter	15, 15
Gap, France	Summer	12
Holloman AFB, NM	Summer, Winter	63, 24
Vandenberg AFB, CA	Summer	23
Osan AB, South Korea	Summer, Winter	25, 49
Riyadh, Saudi Arabia	Summer, Winter	30, 35
Sirene Observatory, France	Summer	9
Three Rivers, CA	Winter	15

After importation of the raw thermosonde data into Matlab<sup>®</sup>, several Matlab<sup>®</sup> scripts converted the raw thermosonde data into useable data structures segregated by site and season. The structure included populated fields for site location and season, elevation, altitude, pressure, relative humidity,  $C_n^2$ , and path-integrated values of  $C_n^2$  for sfc-5k, sfc-10k and sfc-20k ft. Array structures of altitude, pressure, temperature, relative humidity and  $C_n^2$  contained all the raw measurement data from each individual flight. These data structures facilitated computation of all pertinent statistics, including vertical profiles generated from the data and mean and standard deviation statistics. Table 3.3 lists the mean path-integrated  $C_n^2$  values and the standard de-

viations for each site. The mean and standard deviations for each site are based on the number of useable flights for each given season. Note from Table 3.3 that average path-integrated values are generally in the range of  $5 \times 10^{-13} \text{ m}^{-2/3}$  to  $1 \times 10^{-12} \text{ m}^{-2/3}$  for all three vertical layers of interest.

All thermosondes are assumed collected under average meteorological conditions. While it is recognized that meteorological extremes can be observed during a flight, for example a migratory weather system that affects temperatures, relative humidities and pressures, it is assumed the ensemble averages are representative of the seasonal climatological record for a given site. This eliminates the need to test all  $\alpha\beta$  combinations of temperature and relative humidity percentiles, and reduces the test factors to average values.

Turbulence theory is founded upon the assumption of weak turbulence. Therefore, each thermosonde flight required validation of this weak turbulence assumption, and elimination of any flights not meeting this requirement. The moments of  $C_n^2$  throughout a 30 km vertical extent of the flight established the baseline definition for weak turbulence. Since these moments entirely characterize the turbulence along the path, they are the defining parameters on the strength of turbulence. Classification of weak turbulence, for each flight, are limiting values of coherence length,  $\rho_0$ , and isoplanatic angle,  $\theta_0$ , of 10 cm and 10  $\mu$ radians respectively. [2] The  $C_n^2$  moments were computed for each thermosonde flight through a 30km vertical atmosphere using the data structures and Matlab<sup>®</sup> scripts realizing Equations 2.19 and 2.20.

Matlab<sup>®</sup> functions for mode and mean calculations produced the corresponding value from the thermosonde data structures for direct comparison to the HELEEOS Climatological  $C_n^2$  Mode and 50<sup>th</sup> percentile values. The percentile function in Excel<sup>®</sup> calculated the 80th through the 99th percentiles of interest. The exact percentile value in Excel<sup>®</sup> depended on the span of the values in the ensemble using a Gaussian or normal distribution fit to the data. Excel<sup>®</sup> did not use a specific lognormal fit, however, the assumption was that the path-integrated  $C_n^2$  values were indeed lognormally

Table 3.3: Thermosonde  $C_n^2$  Statistics

Site and Season		Mean Path-Integrated $C_n^2$ ( $m^{-2/3}$ )		
		5k ft	10k ft	20k ft
Adelaide, Australia	Winter	$1.0998 \times 10^{-12}$	$1.1990 \times 10^{-12}$	$1.2552 \times 10^{-12}$
Bahrain	Summer	$4.5548 \times 10^{-13}$	$4.9361 \times 10^{-13}$	$5.3548 \times 10^{-13}$
Doha, Qatar	Summer	$7.5853 \times 10^{-13}$	$7.9553 \times 10^{-13}$	$8.7080 \times 10^{-13}$
	Winter	$6.4620 \times 10^{-13}$	$6.9153 \times 10^{-13}$	$7.5833 \times 10^{-13}$
Gap, France	Summer	$1.0918 \times 10^{-12}$	$1.2430 \times 10^{-12}$	$1.3671 \times 10^{-12}$
Holloman AFB, NM	Summer	$4.8557 \times 10^{-13}$	$6.1630 \times 10^{-13}$	$7.8335 \times 10^{-13}$
	Winter	$7.4733 \times 10^{-13}$	$8.8679 \times 10^{-13}$	$9.6988 \times 10^{-13}$
Osan AB, South Korea	Summer	$3.0936 \times 10^{-13}$	$3.5972 \times 10^{-13}$	$3.9592 \times 10^{-13}$
	Winter	$5.8321 \times 10^{-13}$	$6.6763 \times 10^{-13}$	$7.0747 \times 10^{-13}$
Riyadh, Saudi Arabia	Summer	$5.1197 \times 10^{-13}$	$5.4710 \times 10^{-13}$	$6.0070 \times 10^{-13}$
	Winter	$4.0680 \times 10^{-13}$	$4.8366 \times 10^{-13}$	$6.9549 \times 10^{-13}$
Sirene Observatory, France	Summer	$4.4989 \times 10^{-13}$	$6.4189 \times 10^{-13}$	$7.5911 \times 10^{-13}$
Three Rivers, CA	Winter	$1.3135 \times 10^{-12}$	$1.7595 \times 10^{-12}$	$2.0137 \times 10^{-12}$
Vandenberg AFB, CA	Summer	$1.0998 \times 10^{-12}$	$1.1990 \times 10^{-12}$	$1.2552 \times 10^{-12}$
Site and Season		Standard Deviation ( $m^{-2/3}$ )		
		5k ft	10k ft	20k ft
Adelaide, Australia	Winter	$7.9141 \times 10^{-13}$	$7.7433 \times 10^{-13}$	$7.9058 \times 10^{-13}$
Bahrain	Summer	$3.9894 \times 10^{-13}$	$4.0841 \times 10^{-13}$	$4.1995 \times 10^{-13}$
Doha, Qatar	Summer	$8.2377 \times 10^{-13}$	$8.1943 \times 10^{-13}$	$8.0601 \times 10^{-13}$
	Winter	$3.4958 \times 10^{-13}$	$3.7215 \times 10^{-13}$	$3.8444 \times 10^{-13}$
Gap, France	Summer	$8.8588 \times 10^{-13}$	$9.3230 \times 10^{-13}$	$9.5864 \times 10^{-13}$
Holloman AFB, NM	Summer	$5.2659 \times 10^{-13}$	$6.2845 \times 10^{-13}$	$8.0697 \times 10^{-13}$
	Winter	$6.9598 \times 10^{-13}$	$7.7722 \times 10^{-13}$	$8.1809 \times 10^{-13}$
Osan AB, South Korea	Summer	$2.3305 \times 10^{-13}$	$2.4286 \times 10^{-13}$	$2.5323 \times 10^{-13}$
	Winter	$4.8472 \times 10^{-13}$	$5.6364 \times 10^{-13}$	$5.6297 \times 10^{-13}$
Riyadh, Saudi Arabia	Summer	$5.5274 \times 10^{-13}$	$5.6312 \times 10^{-13}$	$6.0198 \times 10^{-13}$
	Winter	$3.0294 \times 10^{-13}$	$3.4168 \times 10^{-13}$	$5.4640 \times 10^{-13}$
Sirene Observatory, France	Summer	$5.5911 \times 10^{-13}$	$7.3025 \times 10^{-13}$	$7.7315 \times 10^{-13}$
Three Rivers, CA	Winter	$1.1483 \times 10^{-12}$	$1.1071 \times 10^{-12}$	$1.1019 \times 10^{-12}$
Vandenberg AFB, CA	Summer	$7.9139 \times 10^{-13}$	$7.9959 \times 10^{-13}$	$7.9563 \times 10^{-13}$



distributed in all cases, corresponding to known atmospheric distributions of  $C_n^2$ . Figure 3.2 (c) and (d) show this is a valid assumption for larger sample sizes. Smaller sample sizes generally assume a lognormal-like pattern, as in Figure 3.2 (a) and (b). However, lognormal distributions are assumed regardless of sample size.

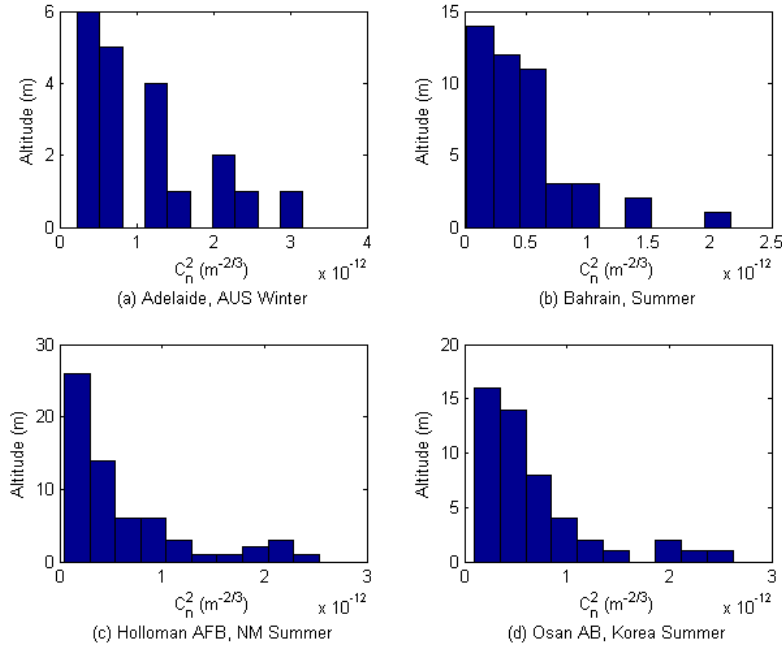


Figure 3.2: Thermosonde distributions for three mid-latitude and one desert site. The lognormal distribution can be seen in each plot. For larger sample sizes, the lognormal distribution becomes apparent, as in (c) and (d). Small sample sizes do not exhibit a recognizable lognormal distribution, but it is assumed all thermosondes are lognormally distributed.

### 3.5 HELEEOS Data

Each site listed in Table 3.1 required generation of two separate datasets: one dataset for the default local time of day (daily average) and another dataset for the local night. Figure 3.3 shows the default atmospheric parameters for the 500 m HELEEOS boundary layer (local night); Figure 3.4 lists the 1524 m HELEEOS boundary layer (local day) defaults. All realizations used the 50% - Average relative humidity default. Each dataset contained information for all six HELEEOS Climatological  $C_n^2$  turbulence percentiles for vertical altitudes of 5k, 10k and 20k ft,

resulting in 12 individual HELEEOS realizations (6 day and 6 night) at each altitude. Matlab® functionalities computed all path-integrated Climatological  $C_n^2$  values and other statistics for each realization.

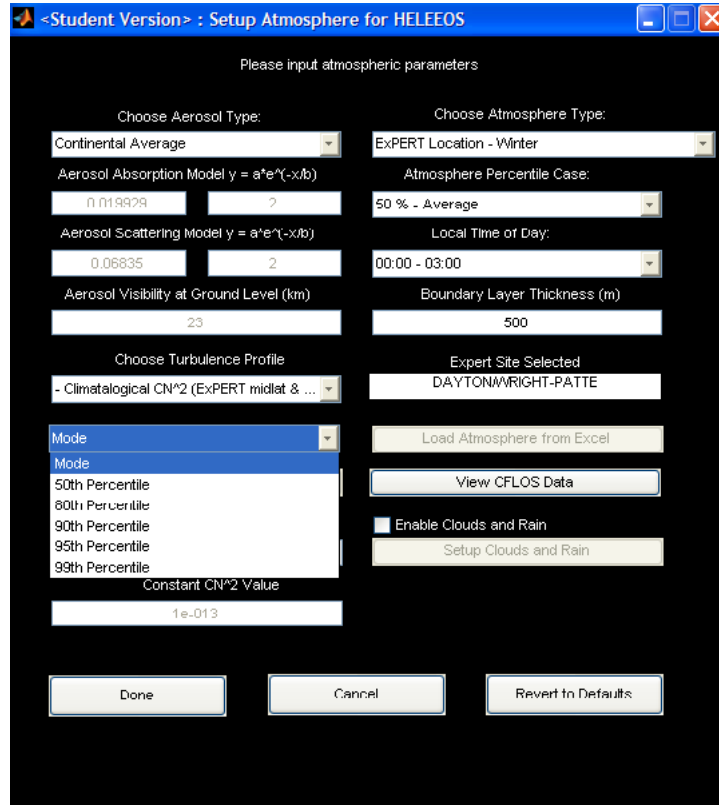


Figure 3.3: HELEEOS Atmosphere GUI for 500 m boundary layer. Notice the time of day selection 00:00-03:00 results in a 500 m boundary layer. The HELEEOS turbulence percentiles are also depicted.

The default boundary layer value for the daily average time of day was 1524 m. The nighttime boundary layer varied from 500 m to 1000 m depending on the time. Recall during transition periods the boundary layer is 1000 m. All nocturnal boundary layer values in HELEEOS reference the 500 m atmospheric boundary layer.

A supplementary software package known as ATMTools® was used to create random  $C_n^2$  profiles consistent with the Climatological  $C_n^2$  profiles for each ExPERT site. ATMTools® is an atmospheric analysis software package created by MZA Associates in Albuquerque, NM, and operates as a fully functional Matlab® atmospheric toolbox for propagation path modeling. ATMTools® wave optics codes utilize the scaling laws

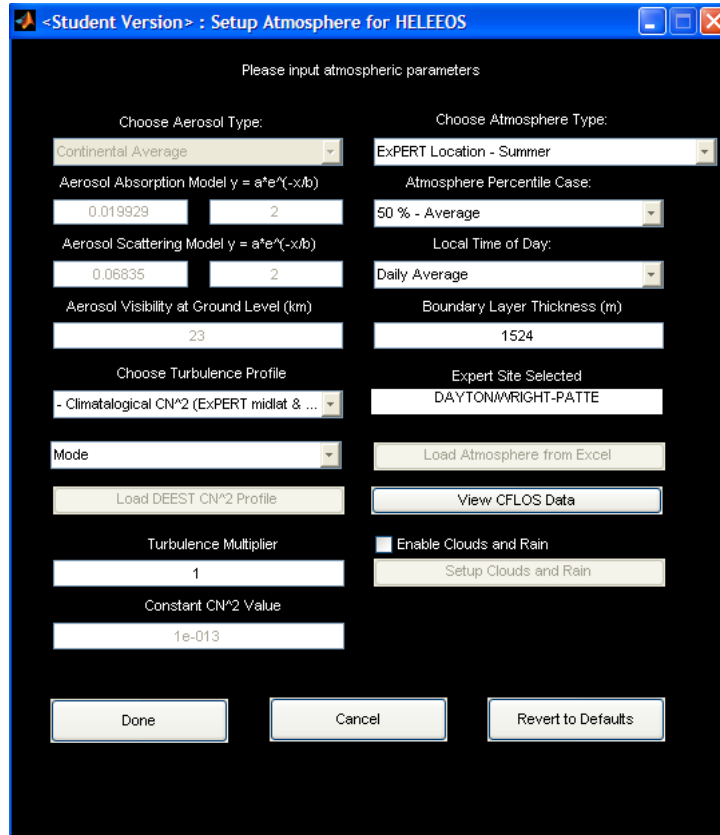


Figure 3.4: HELEEOS Atmosphere GUI for 1524 m boundary layer. Note Local Time of Day is the default value of Daily Average. The 1524 m boundary layer can also be selected by using Local Time of Day 09:00-21:00.

of the Scaling Code for Airborne Laser Engagement (SCALE) and the Scaling law for High Altitude Relay Engagement (SHARE). [16] The atmospheric characterizations within ATMTools<sup>®</sup> include functions for computing atmospheric parameters such as  $r_0$ ,  $\theta_0$ , and the Rytov variance,  $\sigma_\chi^2$ ; atmospheric modeling includes functions for generating atmospheric parameters such as  $C_n^2$ , absorption, scattering, wind, temperature, pressure and density. ATMTools<sup>®</sup> generates an atmospheric Matlab<sup>®</sup> data structure and the only required information are the engagement geometry and information regarding the phase screens for each analysis point.

The *RandCn2Prof* (Random  $C_n^2$  Profiles) function within ATMTools<sup>®</sup> generates random  $C_n^2$  profiles with fixed parameters established by a basis atmospheric structure. This function creates random  $C_n^2$  profiles through the vector addition of null

space vectors with degrees of freedom equivalent to the number of phase screens, or propagation points, within the atmospheric structure. HELEEOS generates a specific atmospheric structure, based on the Climatological  $C_n^2$  profile, and this structure is the basis atmospheric structure for the *RandCn2Prof* function. The *RandCn2Prof* function analyzes the atmospheric structure and generates random  $C_n^2$  profiles with identical  $r_0$ ,  $\theta_0$  and  $\sigma_\chi^2$  parameters as that in the HELEEOS atmospheric structure. Figure 3.5 is an example of three random  $C_n^2$  profiles created using *RandCn2Prof*. The random  $C_n^2$  profiles generate varying, but equivalent, null space vectors at each point, but the vector addition of these null space vectors do not alter the fixed-path parameter values of the  $C_n^2$  moments. The random profiles can generate as many null space vectors as there are degrees of freedom, thus making it a robust tool for replicating the optical path parameters but randomizing the overall  $C_n^2$  value along the path. The *RandCn2Prof* function also has built-in safeguards to reject invalid  $C_n^2$  values, and will only attempt to generate a "good" profile 10,000 times. [15]

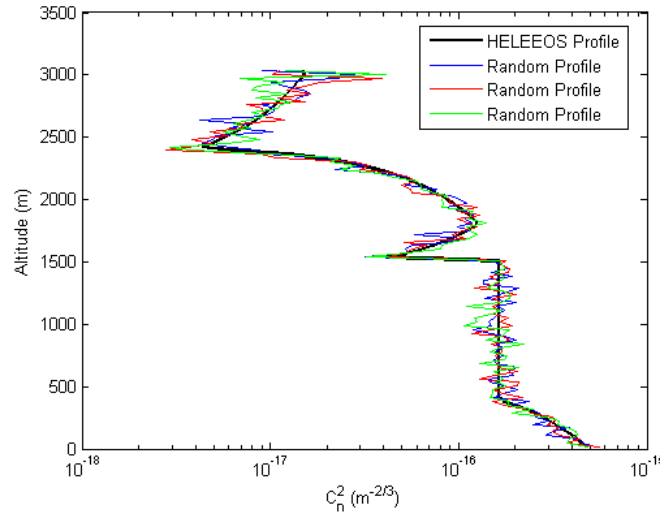


Figure 3.5: Random  $C_n^2$  profiles generated by the *RandCn2Prof* function in *ATMTools*<sup>®</sup>. The black line is the HELEEOS profile created for Holloman AFB, NM (EXPERT Summer, mode Climatological  $C_n^2$  turbulence, 50th percentile RH, and daily average temperature). The blue, red and green lines are the random  $C_n^2$  profiles created that retain the same atmospheric parameters of  $r_0$ ,  $\theta_0$  and  $\sigma_R^2$  as the basis atmospheric structure (the black profile). Standard deviation for 1000 random iterations was  $7.1081 \times 10^{-17} \text{ m}^{-2/3}$ . Note: all altitudes are in m above ground level (AGL) rather than m mean sea level (MSL).

These random  $C_n^2$  profiles establish standard deviations for the HELEEOS Climatological  $C_n^2$  profiles. HELEEOS generates only a single, non-variant profile for a given ExPERT site and percentile of interest. However, to analyze the profiles properly utilizing DOE techniques, a standard deviation is needed. The *RandCn2Prof* function generated 5000 random  $C_n^2$  profiles with identical atmospheric parameters for each HELEEOS atmosphere. This number of profiles ensured a log-normal distribution to the  $C_n^2$  profiles. This is confirmed in Figure 3.6. These iterations were then analyzed to arrive at a standard deviation for each site. The standard deviations are random as well, generated from the 5000 random  $C_n^2$  iterations, and varies for each 5000 iteration ensemble. Using this method to arrive at standard deviations may result in additional error in the test, but given that these standard deviations are on the order of  $10^{-16} \text{ m}^{-2/3}$  or less while the path-integrated values are on the order of  $10^{-13} \text{ m}^{-2/3}$ , it is sufficient to consider this additional error a nuisance noise factor in the statistical analysis of the data. All standard deviation calculations are the ensemble average of the 1000 realizations for each altitude of interest.

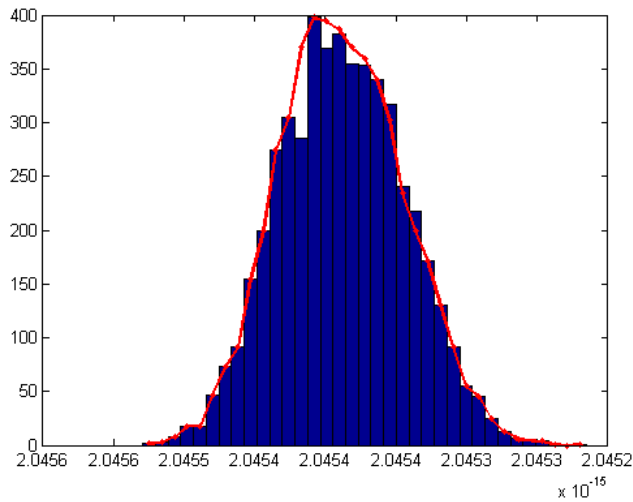


Figure 3.6: Log normal distribution of 5000 random  $C_n^2$  realizations using ATMTools®. The rough lognormal curve is depicted by the red line. As the number of iterations increase, the distribution becomes even more “classically” lognormally distributed.

Two problems directly affecting the Climatological  $C_n^2$  calculations surfaced during the HELEEOS data collection effort. The first problem was a discrepancy associ-

ated with the HELEEOS calculations of the boundary layer Climatological  $C_n^2$  values. Recall from Section 2.5 that the HELEEOS boundary layer is divided into two layers. Layer 1 extends from the surface through 60 m; the second from 60 m through the top of the respective boundary layer as defined by the time of day selection. Calculations of the second layer (60m-boundary layer height) contained large vertical sections of constant Climatological  $C_n^2$  values created by nearest neighbor correlations from the look-up tables. If a particular bin within the look-up tables is not populated, HELEEOS uses the nearest neighbor bin value for the Climatological  $C_n^2$  calculation. The lack of populated bins in the look-up tables resulted in these large vertical layers with constant Climatological  $C_n^2$  values. Figure 3.7 depicts this problem for Bahrain. Notice the nearly constant layer from 360m through the top of the boundary layer in Figure 3.7(a).

This unexpected problem occurred at all locations to varying degrees. The main effect of this problem was a substantial increase in the path-integrated  $C_n^2$  values for the 1524 m HELEEOS boundary layer data. The partial fix to this problem was a HELEEOS software update to smoothly interpolate, or lapse, the Climatological  $C_n^2$  profile from the point where constant, repetitive Climatological  $C_n^2$  values occur to the top of the HELEEOS boundary layer. Figure 3.7(b), shows the resultant profile where the smooth interpolation technique is easily recognizable in the Climatological  $C_n^2$  curve. While this reduces the error in the path-integrated  $C_n^2$  values, it does not completely eliminate it. Time did not permit a complete solution to this problem for this research effort, and this issue will be addressed at a later date.

Another problem arose in the seasonal climatological record matching for southern hemisphere sites. The algorithm did not access the climatology for Southern Hemispheric sites, and was defaulting to Northern Hemispheric climatological data for the Climatological  $C_n^2$  curves. The algorithm was corrected, and this problem was solved.

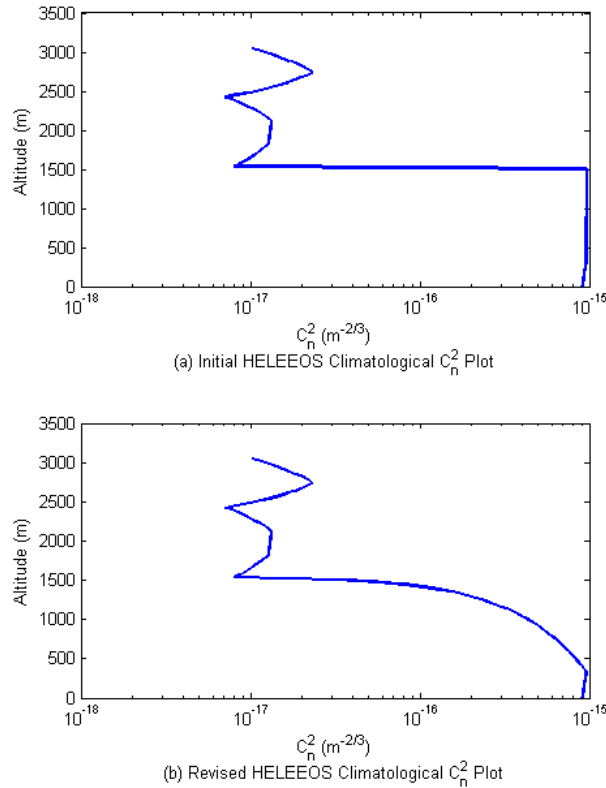


Figure 3.7: Problems associated with the boundary layer calculations in HELEEOS. In (a), constant Climatological  $C_n^2$  values are observed from about 360 m through 1524 m. In (b), the temporary software solution produced a smooth curve from about 360 m to 1524 m.

### 3.6 DOE Test Methodology and Design

This designed experiment consisted of eight primary factors: Source, Climate, Location, Altitude, Season, Boundary Layer, Time of Day, and Turbulence Level. A Source factor indicated either HELEEOS or Thermosonde. A Climate factor indicated Desert or Mid-latitude, in agreement with the HELEEOS interpretation of the ExPERT database. The Season factors consisted of summer or winter; the Altitude factors indicated the respective altitude of interest: sfc-5k ft (1524 m), sfc-10k ft (3048 m) and sfc-20k ft (6096 m). Figure 3.8 depicts a sample design matrix of the Vandenberg AFB, CA summer nighttime (500 m boundary layer) runs.

A2 HELEEOS / Thermasonde										
	A	B	C	E	F	G	H	I	L	M
1		climate			season		time			
2	HELEEOS / Thermasonde	Desert / Midlat	location	altitude	summer / winter	BL (m)	night / daily ave	Turbulence level	C <sub>n</sub> <sup>2</sup> (response)	
1047	HELEEOS	midlat	Vandenberg	5K	summer	500	night	mode	5.2500E-13	
1048	HELEEOS	midlat	Vandenberg	5K	summer	500	night	50%	6.9400E-13	
1049	HELEEOS	midlat	Vandenberg	5K	summer	500	night	80%	1.1010E-12	
1050	HELEEOS	midlat	Vandenberg	5K	summer	500	night	90%	1.4290E-12	
1051	HELEEOS	midlat	Vandenberg	5K	summer	500	night	95%	1.8280E-12	
1052	HELEEOS	midlat	Vandenberg	5K	summer	500	night	99%	2.4330E-12	
1053	HELEEOS	midlat	Vandenberg	10K	summer	500	night	mode	6.6100E-13	
1054	HELEEOS	midlat	Vandenberg	10K	summer	500	night	50%	8.6000E-13	
1055	HELEEOS	midlat	Vandenberg	10K	summer	500	night	80%	1.3560E-12	
1056	HELEEOS	midlat	Vandenberg	10K	summer	500	night	90%	1.7490E-12	
1057	HELEEOS	midlat	Vandenberg	10K	summer	500	night	95%	2.2160E-12	
1058	HELEEOS	midlat	Vandenberg	10K	summer	500	night	99%	2.9880E-12	
1059	HELEEOS	midlat	Vandenberg	20K	summer	500	night	mode	7.3300E-13	
1060	HELEEOS	midlat	Vandenberg	20K	summer	500	night	50%	9.0000E-13	
1061	HELEEOS	midlat	Vandenberg	20K	summer	500	night	80%	1.3330E-12	
1062	HELEEOS	midlat	Vandenberg	20K	summer	500	night	90%	1.6440E-12	
1063	HELEEOS	midlat	Vandenberg	20K	summer	500	night	95%	1.9980E-12	
1064	HELEEOS	midlat	Vandenberg	20K	summer	500	night	99%	2.8670E-12	
1065	Thermasonde	midlat	Vandenberg	5K	summer	n/a	night	mode	3.3000E-13	
1066	Thermasonde	midlat	Vandenberg	5K	summer	n/a	night	50%	1.0590E-12	
1067	Thermasonde	midlat	Vandenberg	5K	summer	n/a	night	80%	1.3480E-12	
1068	Thermasonde	midlat	Vandenberg	5K	summer	n/a	night	90%	2.1176E-12	
1069	Thermasonde	midlat	Vandenberg	5K	summer	n/a	night	95%	2.8760E-12	
1070	Thermasonde	midlat	Vandenberg	5K	summer	n/a	night	99%	3.0235E-12	
1071	Thermasonde	midlat	Vandenberg	10K	summer	n/a	night	mode	3.4400E-13	
1072	Thermasonde	midlat	Vandenberg	10K	summer	n/a	night	50%	1.0850E-12	
1073	Thermasonde	midlat	Vandenberg	10K	summer	n/a	night	80%	1.3794E-12	
1074	Thermasonde	midlat	Vandenberg	10K	summer	n/a	night	90%	2.1682E-12	
1075	Thermasonde	midlat	Vandenberg	10K	summer	n/a	night	95%	2.9157E-12	
1076	Thermasonde	midlat	Vandenberg	10K	summer	n/a	night	99%	3.0654E-12	
1077	Thermasonde	midlat	Vandenberg	20K	summer	n/a	night	mode	4.2900E-13	
1078	Thermasonde	midlat	Vandenberg	20K	summer	n/a	night	50%	1.1110E-12	
1079	Thermasonde	midlat	Vandenberg	20K	summer	n/a	night	80%	1.4118E-12	
1080	Thermasonde	midlat	Vandenberg	20K	summer	n/a	night	90%	2.1874E-12	
1081	Thermasonde	midlat	Vandenberg	20K	summer	n/a	night	95%	2.9420E-12	
1082	Thermasonde	midlat	Vandenberg	20K	summer	n/a	night	99%	3.0854E-12	

Figure 3.8: Partial DOE nighttime summer design matrix for Vandenberg AFB, CA. The nighttime thermosonde data served as the test truth data for both the nighttime and daytime (daily average) Time of Day categories.

The Time-of-Day (ToD) categories corresponded to the HELEEOS ToD selections in the Atmosphere GUI, with classifications of either night or daily average. The daytime, or diurnal, ToD factor corresponds to the local hours of 09:00-21:00. The nighttime, or nocturnal, ToD factor corresponds to local hours of 00:00-06:00. Thermosonde campaign data are nighttime data, allowing for a direct comparison to the nighttime HELEEOS Climatological  $C_n^2$  profiles. However, comparison of the nocturnal thermosonde data to the daily average HELEEOS data required the assumption that the "daily average" encompasses all hours of the day. Therefore, the noctur-



nal thermosonde data are the truth data basis for both the daytime and nighttime HELEEOS Climatological  $C_n^2$  profiles.

The time of day selection in HELEEOS is important because it establishes the probabilistic temperature for the Climatological  $C_n^2$  profile. Choosing a specific time of day means choosing a specific climatology for given time of day at that site. Recall from Section 2.5 that HELEEOS computes the boundary layer turbulence profiles from the climatological temperature and relative humidity record. The climatology for each site is divided into hourly surface average temperatures and relative humidities, as well as daily surface averages for both of these parameters. The lapsing through the boundary layer is dependent upon the surface temperature and relative humidity correlated to the time of day selection. This was also additional justification for testing the daily average time of day profiles against the nocturnal thermosonde data. Figure 3.9 shows a partial HELEEOS design matrix for the daily average time of day selection for the Vandenberg AFB, CA summer runs.

A2		HELEEOS / Thermosonde								
	A	B	C	E	F	G	H	I	L	
1	climate		time							
2	HELEEOS / Thermosonde	Desert / Midlat	location	altitude	summer / winter	BL (m)	night / daily ave	Turbulence level	$C_n^2$ (response)	
1083	HELEEOS	midlat	Vandenberg	5K	summer	1524	daily ave	mode	4.1100E-13	
1084	HELEEOS	midlat	Vandenberg	5K	summer	1524	daily ave	50%	8.4900E-13	
1085	HELEEOS	midlat	Vandenberg	5K	summer	1524	daily ave	80%	1.7820E-12	
1086	HELEEOS	midlat	Vandenberg	5K	summer	1524	daily ave	90%	2.6430E-12	
1087	HELEEOS	midlat	Vandenberg	5K	summer	1524	daily ave	95%	3.6700E-12	
1088	HELEEOS	midlat	Vandenberg	5K	summer	1524	daily ave	99%	5.0640E-12	
1089	HELEEOS	midlat	Vandenberg	10K	summer	1524	daily ave	mode	5.4600E-13	
1090	HELEEOS	midlat	Vandenberg	10K	summer	1524	daily ave	50%	1.0150E-12	
1091	HELEEOS	midlat	Vandenberg	10K	summer	1524	daily ave	80%	2.0370E-12	
1092	HELEEOS	midlat	Vandenberg	10K	summer	1524	daily ave	90%	2.9630E-12	
1093	HELEEOS	midlat	Vandenberg	10K	summer	1524	daily ave	95%	4.0580E-12	
1094	HELEEOS	midlat	Vandenberg	10K	summer	1524	daily ave	99%	5.6190E-12	
1095	HELEEOS	midlat	Vandenberg	20K	summer	1524	daily ave	mode	6.5200E-13	
1096	HELEEOS	midlat	Vandenberg	20K	summer	1524	daily ave	50%	1.2200E-12	
1097	HELEEOS	midlat	Vandenberg	20K	summer	1524	daily ave	80%	2.4560E-12	
1098	HELEEOS	midlat	Vandenberg	20K	summer	1524	daily ave	90%	3.5780E-12	
1099	HELEEOS	midlat	Vandenberg	20K	summer	1524	daily ave	95%	4.9080E-12	
1100	HELEEOS	midlat	Vandenberg	20K	summer	1524	daily ave	99%	6.7830E-12	

Figure 3.9: Partial DOE daytime summer design matrix for Vandenberg AFB, CA.

The Location factors corresponded to the ten site locations listed in Table 3.1. The ExPERT location nearest Doha, Qatar was Abu Dhabi International Airport. This location was renamed Qatar (Abu Dhabi) for the purposes of the test. In ad-

dition, the two combined France locations (Gap and Sirene Observatory, France) corresponded to the ExPERT site location of Paris.

Relative humidity was not designed into this test. HELEEOS' default relative humidity is the 50<sup>th</sup> percentile, or average percentile. There are nine relative humidity percentiles available for selection in HELEEOS. Analysis of the difference of these nine percentiles revealed a maximum two-fold change in the strength of the optical turbulence from the lowest path-integrated Climatological  $C_n^2$  value (99<sup>th</sup> RH percentile) to the highest Climatological  $C_n^2$  value (1<sup>st</sup> RH percentile). In addition, the turbulence strength was identical for the 80<sup>th</sup>, 90<sup>th</sup>, and 99<sup>th</sup> percentiles in all cases. Since these values are typically viewed on a logarithmic scale to begin with, even a scalar doubling of the turbulence strength is relatively little variation in the overall magnitude. This inverse behavior in the strength of optical turbulence was expected since relative humidity exhibits an inverse relationship with the strength of optical turbulence, as described in Section 2.6. In addition, since all thermosondes are assumed collected under average meteorological conditions, the average relative humidity category was deemed appropriate to this test.

The Turbulence Level factors corresponded to the turbulence percentiles in HELEEOS. For the thermosondes, the turbulence profiles were calculated using the method described in Section 3.4.

The complete design matrix consisted of 1098 lines for all the sites listed in Table 3.1. A Microsoft Excel<sup>®</sup> spreadsheet (the design matrix) served as the input for the statistical DOE analysis software package Statistica<sup>®</sup> that includes a module designed specifically for DOE applications. Its powerful algorithms easily detect higher order interactions between the various test factors and shows the comparisons of one data set to another. It determines if the two data sets (HELEEOS and Thermosonde) are statistically the same or if they vary and by how much. In addition, it establishes confidence bounds on the statistical equivalence of the data. All DOE analysis was completed using the Statistica<sup>®</sup> software.

In addition to the DOE analysis module, **Statistica**<sup>®</sup> also incorporates a robust ANOVA module designed to rigorously analyze the variance in the residual errors. This particular design allowed for analysis of all main effects and 2-way interactions. Three-way interactions are inferred, but do not reflect ANOVA values. This occurs due to limited degrees of freedom associated with this design that prevented ANOVA analysis for these higher-order interactions. All higher-order interactions were rolled into a single error term and handled accordingly in the ANOVA analysis.

## IV. Results

This chapter describes the results obtained during the course of this research effort. Section 4.1 discusses the validation of the statistical DOE model. This is important for accurate results from the Statistica® analysis. Section 4.2 covers some of the data manipulation for the DOE design matrix. Large higher order interactions, specifically 9-level interactions, demanded the use of blocking factors and data groupings for the DOE analysis. In addition, the data required transformations in order to remove the lognormal dependencies. Subsection 4.3.1 presents the results of the transformed data format while Subsection 4.3.2 presents the untransformed results. Section 4.4 demonstrates the usefulness of the HELEEOS Climatological  $C_n^2$  optical turbulence model through several applications of wave optics simulations. These simulations validate the Climatological  $C_n^2$  model as a viable optical turbulence model. Overall results from this research effort are contained in Section 4.5.

### 4.1 Validation of the Statistical Model

Recall the DOE statistical analysis model has three basic assumptions for ensuring model completeness: independent samples, normally distributed residual errors with zero mean and equal residual cell variances. The goodness of the statistical model is determined in part through the normal probability plot for the variances and the histogram plot for the normal distribution.

For the thermosondes, measurement techniques validated the independence of the samples. Each flight is independent of all other flights. The collection method, downlink of the radiosonde information, is unique to each flight and does not rely on the collections of previous or future thermosonde flights. In addition, each campaign is independent. The Adelaide, Australia campaign is not dependent on the results of the Three Rivers, CA campaign, for example. The probabilistic nature of the Climatological  $C_n^2$  profile ensures independence of the HELEEOS samples. Each profile requires the climatological record of that particular site. Since no two climatologies are identical, the independence of each HELEEOS sample is validated.

The second model assumption mandates normally distributed zero mean residual errors. For both the HELEEOS and thermosonde data, initial investigations indicated the data required transformation. The natural logarithm transformation removed the lognormal dependencies in both the HELEEOS and thermosonde data. The transformation used was:

$$\text{Transformed data} = \ln (C_n^2 * 10^{12} m^{2/3}) . \quad (4.1)$$

This transformation ensured the normality requirement of the model. Proof of this is easily recognized in a histogram plot, shown in Figure 4.1 (a). All residual errors lie within three standard deviations of the zero mean value.

The variances of the residuals must also be equal (but not known exactly) to validate the statistical model. This assumption relates to the randomness of the test, as described previously. Randomness in the test ensures outside factors do not adversely influence the test. The normal probability plot in Figure 4.1 (b) shows the correlation of the residuals. The transformations produced an acceptable correlation, although some minor residuals in the tails of the normal distribution showed some slight variability. Based on these results, the statistical model was validated and the DOE test was conducted on the transformed data.

#### ***4.2 Data Manipulation and Blocking Factors***

Recall from Chapter 2 that an interaction between factors is the change in the realization produced by a variation in the levels of the factors. The 9-level variable forced by the Location factor required special consideration. Due to the large size of the Location factor, several separate analyses were performed. One ANOVA analysis focused solely on the location factor taking into account the Source and Season factors. A separate DOE analysis investigated the Location interactions using blocks on the Location factor. Another DOE analysis interrogated the Location factor by considering only the 2- and 3-level variables, this time without blocking. The initial

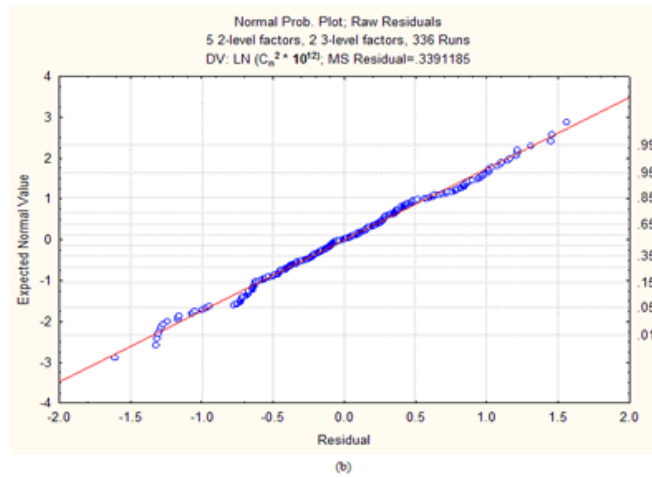
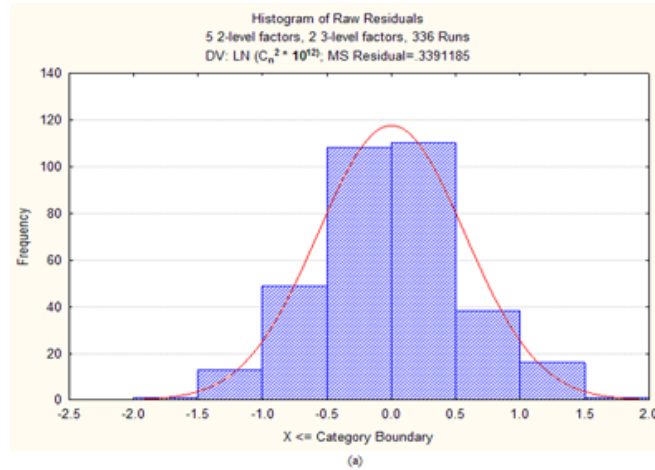


Figure 4.1: Histogram plot of the residual errors is shown in (a). The normal probability plot of the residuals is shown in (b). The plot shows acceptable correlation of the residuals. All residuals fall within three standard deviations of the mean. The model was not a perfect model as shown by the lack of perfect linearity in the residual errors.

DOE analysis showed potential for combining several of the higher level interactions into 2- or 3-level variables thereby allowing analysis of the effects of these higher level interactions. After data transformation, effects deemed statistically insignificant were rolled into a single error term. Combining all non-significant interactions into test data noise strengthens the DOE analysis by considering only causal factors in the final analysis. All of the main factors (Climate, Season, Time of Day, Boundary Layer, etc.) with the exception of the Location factor were causal factors. The regression

model, used for point estimators of the residual errors, accounts for all causal and higher order interactions.

The regression model input consisted of six 2-level factors and one 3-level factor, allowing for a complete factorial design of the experiment. The final regression equation for this model, after all data manipulations, was:

$$\begin{aligned}
 \hat{y} = & 135933.55 + 20.89 \cdot Source - 1401.83 \cdot Climate - 2629.02 \cdot Altitude(L) \\
 & + 12.85 \cdot Altitude(Q) + 26.04 \cdot Season - 0.18 \cdot BoundaryLayer(L) \\
 & + 0.21x10^{-4} \cdot BoundaryLayer(Q) + 1.00 \cdot TurbulenceLevel \\
 & + 0.39 \cdot Source \cdot Climate - 0.60 \cdot Source \cdot Season \\
 & - 0.01 \cdot Source \cdot TurbulenceLevel + 25.92 \cdot Climate \cdot Altitude(L) \\
 & - 0.13 \cdot Climate \cdot Altitude(Q) + 0.35 \cdot Climate \cdot Season \\
 & + 2.64x10^{-3} \cdot Climate \cdot BoundaryLayer(L) \\
 & - 2.00x10^{-6} \cdot Climate \cdot BoundaryLayer(Q) \\
 & - 8.63x10^{-4} \cdot Season \cdot BoundaryLayer(L) \\
 & - 1.38x10^{-3} \cdot TimeofDay \cdot TurbulenceLevel
 \end{aligned} \tag{4.2}$$

where (L) is the linear interaction term associated with the specific factor and (Q) is the quadratic interaction term.

The ANOVA regression model required blocking variables due to the large 9-level relationship associated with the Location factor. Furthermore, the two France campaigns complicated the comparison with the HELEEOS ExPERT site Paris. Combining these two campaigns into a single dataset allows for full comparative analysis of the HELEEOS and thermosonde data. However, it was necessary to determine statistical equivalence of these two campaigns first before merging the two campaigns into a single dataset. Results of a limited factorial ANOVA (of the two France thermosonde campaigns) proved statistical equivalence, these two campaigns formed a

single "Paris" dataset. A final Climate block for the Location factor was used to segregate the Mid-latitude sites from the Desert sites. This assumed no interactions between the Climate factors. Applying the Climate block restricted all higher order interactions and allowed for a full ANOVA analysis of the Mid-latitude and Desert sites.

Computation of the 80<sup>th</sup> through 99<sup>th</sup> percentiles for the thermosonde data relied on the Excel<sup>®</sup> percentile function for the Turbulence Level factor. This Excel<sup>®</sup> function utilizes a Gaussian fit to the data while the corresponding HELEEOS percentiles utilize a true lognormal fit. This difference produced unsatisfactory variability in the initial results due to the differences in the distributions used to arrive at these percentiles. The variations decreased in the tails of both distributions, but the error induced by these differences at the 80<sup>th</sup> through 95<sup>th</sup> provided reasonable justification for eliminating these outlier percentiles from the test. Therefore, the DOE factorial design retained only the Mode and 50<sup>th</sup> percentile data (both HELEEOS and thermosonde) for the research. The Matlab<sup>®</sup> mode and mean functions computed these values for the thermosonde data, and these two categories are equivalent indexes in both the HELEEOS and thermosonde datasets. This reduced the Turbulence Level factor to a 2-level factor and completed the factorial design of the test.

### **4.3 Results**

The results in this section are presented in two formats. The first is in the transformed data format, with elimination of the lognormal dependencies within the data. All charts in this section came directly from the Statistica<sup>®</sup> software package, and presentation of each chart is in the form of point estimators with error bars. The second format is for the untransformed data results. The presentation of these results are in the form of bar charts with error bounds.

This section introduces new terminology and units, particularly with the untransformed data results. All references to 5k, 10k and 20k ft in the following discussions refer to the vertical profiles from the sfc-5k, sfc-10k, and sfc-20k ft respectively.



However, specific usage of an altitude level, such as 5k ft, indicates a vertical layer from the surface to that particular altitude. The term “mean” in the untransformed results is interpreted as the mean value of the range of the data, not as indicating a strict relation to the 50<sup>th</sup> percentile profile data. Finally, the y-axes for all transformed data charts consist of unitless logarithmic values. The y-axis variable is labeled as  $\text{LN}(C_n^2 * 10^{12})$  to indicate the transformation used on the original data. Negative values appear on these charts and are a direct result of the applied logarithmic data transformation. The negative values assume positive real values after untransforming the data into units of  $\text{m}^{-2/3}$ .

*4.3.1 Transformed Data Results.* Figure 4.2 shows the overall outcomes of the DOE analysis. This is a plot of HELEEOS data versus Thermosonde data as a function of site Location and Source and combines both turbulence values (Mode and 50<sup>th</sup> percentile) with all other factors (Climate, Season, etc.) This chart is a composite result of all possible interactions of the test factors, and it determines the statistical equivalence of the two datasets - HELEEOS and Thermosonde. The vertical bars denote the upper and lower 80% confidence intervals for the range of path-integrated  $C_n^2$  values at each respective location.

The null hypothesis of this test is that the HELEEOS means are equal to the thermosonde means at each location. Statistical equivalence implies equality of the statistical moments for each location. Statistical differences indicate enough variation in the data to state the means and standard deviations are not equal. However, statistical differences do not infer disagreements in the data; they merely point out a wider variability in the moments. Fully substantiating these differences requires a broader insight into the data than a mere statement of the statistical equivalence of the moments. For example, if the results pointed to statistical differences in the means, but these differences varied only by a scalar fraction in the strength of the path-integrated optical turbulences, the overall results may show the means do in fact agree. It is important not to declare statistical equivalence or difference without

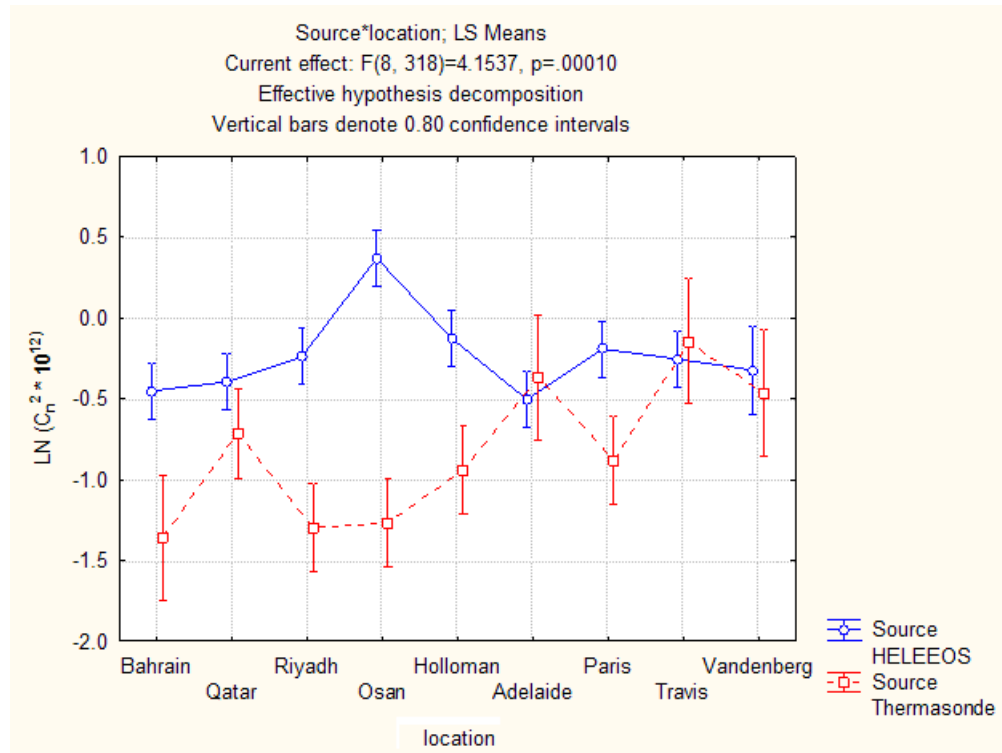


Figure 4.2: Least squares means for all locations. The blue line is the HELEEOS results and the red line is the thermosonde results. The vertical bars indicate 80% confidence intervals. The blue circle denotes the mean value of the HELEEOS datasets and the red square denotes the mean value of the thermosonde datasets.

taking all possible information into account. In addition, transformed data emphasize these statistical equivalences or differences more emphatically than the untransformed data because the lognormal distributions in the data are removed. The transformed data show greater variation, but when the data are untransformed, the true results show a more realistic agreement in the data.

Figure 4.2 shows the HELEEOS and the thermosonde transformed data are generally statistically different from one another when all factors are combined. Adelaide, Travis and Vandenberg exhibit statistical equivalence, while Osan exhibits the largest statistical difference of all the locations. In most cases, the HELEEOS mean is larger than the thermosonde mean. These results are expected for two reasons. First, Section 3.5 described a noted tendency to higher HELEEOS path-integrated  $C_n^2$  values because of the smoothing algorithm used in the boundary layer Climatological  $C_n^2$

profile for the 1524 m boundary layer. These results encapsulate all possible values, including the larger 1524 m data, and skew the results. When the 1524 m boundary layer is removed, the 500 m boundary layer data exhibits better statistical equivalence. This is discussed in greater detail in the next section. Secondly, the HELEEOS profile utilizes probabilistic climatology, and this removes the variability seen during a thermosonde campaign, even though these campaigns are conducted under nearly homogeneous meteorological conditions. The homogeneous conditions at the time of a thermosonde launch may not be entirely representative of long-term climatological conditions, and this disparity may very well surface as a statistical difference between the HELEEOS and thermosonde data.

Note the tighter HELEEOS confidence intervals as compared to the thermosonde confidence intervals in Figure 4.2. This is a by-product of a single HELEEOS generated profile as compared to many measured thermosonde profiles. These tight confidence intervals reflect the small standard deviations calculated by the *RandCn2Prof* function in *ATMTools*<sup>®</sup>.

The large differences in the Osan data are a potential cause for concern. This is a result of sparse data in the look-up tables, which in turn, induce higher path-integrated  $C_n^2$  values for the 1524 m boundary layer. As a general rule, Osan data exhibit statistical differences from the thermosonde data when all factors are considered both as a composite and independently. Osan thermosonde data forms the foundation of all HELEEOS Mid-latitude sites. These other mid-latitude sites may be artificially skewed because of this issue in the Osan data. It appears this is not the case, however, since the Travis and Vandenberg profiles closely correlate to the thermosonde data. Still, this statistical difference may point to a residual problem created by the software update to correct the computation of the Climatological  $C_n^2$  profile within the boundary layer.

Figure 4.3 shows the combined effects of Source, Location and Altitude. This is a plot of the effects of altitude on the path-integrated HELEEOS and thermosonde

data at each site location. Some interesting features arise from the data. Figure 4.3 (a-1) emphasizes the statistical equivalence of the three altitudes. This is not surprising since the 5k and 10k ft profiles are subsets of the 20k ft profiles. The closeness in the thermosonde means is a physical realization of the properties of homogeneity and isotropy under the weak turbulence regime. The overlapping confidence intervals prove the means are not a function of time or position, and show the thermosonde means are statistically equivalent in the atmospheric volumes under consideration. It is a fair assumption to expect this same behavior in the HELEEOS means, and the profiles show this is generally the case. The Paris and Travis profiles deviate slightly, but overall the results are consistent with the thermosonde.

Figure 4.3 (b) splits the analysis further into specific altitudes and compares the HELEEOS Mode and 50<sup>th</sup> percentile turbulence data to the corresponding thermosonde data. All three altitude levels exhibit consistent results, with Osan again exhibiting the greatest deviation. It is the opinion of this author that these deviations are the result of sparsely populated look-up tables between 360 m and the top of the 1524 m boundary layer, particularly for the winter season. Further analysis of the effects of season revealed the winter season contributed the preponderance of the statistical differences noted in the overall results, and combining the two seasonal datasets results in a greater overall statistical difference. However, individual analysis shows the HELEEOS summer season data correlates well to the thermosonde data, while the HELEEOS winter season data are largely different from the thermosonde means. Figure 4.4 (a) and (b) emphasizes these pronounced distinctions. These plots consider only the combined effects of season and altitude; all other factors are ignored. Missing thermosonde sites are consistent with Table 3.2.

Figure 4.5 shows the seasonal results for all combined effects. It encapsulates all factors of Climate, Season, Altitude, Location, Time of Day and Boundary Layer. Again, the summer datasets exhibits closer statistical equivalence as compared to the winter datasets. This plot lends further credence to the claim of sparsely popu-

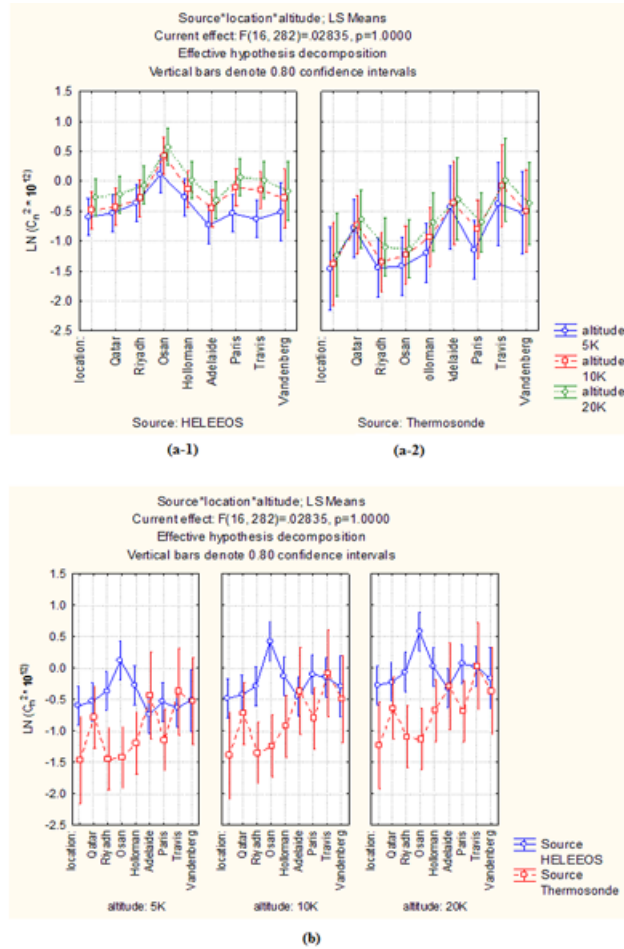


Figure 4.3: Least squares means plot of the effects of Altitude and Location on the HELEEOS and therosonde path-integrated  $C_n^2$  values. Plots (a-1) and (a-2) demonstrate the consistency of both the HELEEOS and therosonde. Plot (b) breaks the altitudes out for a closer analysis. All plots are for the combined effects of Mode and 50<sup>th</sup> percentile turbulence levels.

lated look-up tables that skew the results to higher path-integrated  $C_n^2$  values. This significance is discussed further in the next Section.

*4.3.2 Untransformed Data Results.* Transforming the data removes all logarithmic dependence in the data and allows for treating the data as  $(NID(0, \sigma^2))$ . Untransforming the data returns a logarithmic dependence to the data, but preserves the results of the DOE analysis. The data was untransformed using the following:

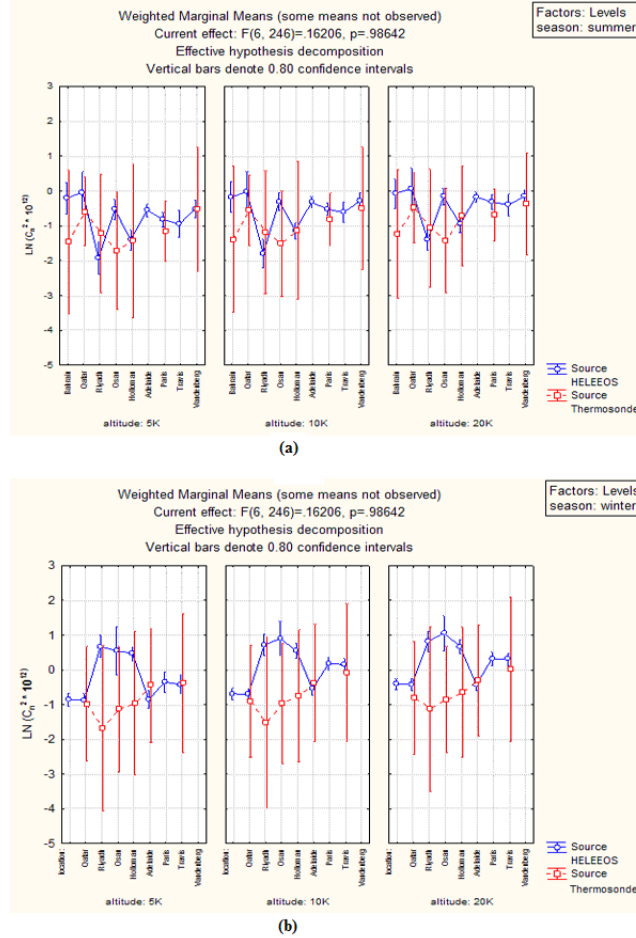


Figure 4.4: (a) Weighted marginal means plot of the effects of Summer and Altitude for the HELEEOS and thermosonde path-integrated  $C_n^2$  values. (b) Weighted marginal means plot of the effects of Winter and Altitude for the HELEEOS and thermosonde path-integrated  $C_n^2$  values. All plots combine the effects of the Mode and 50<sup>th</sup> percentile turbulence levels.

$$Untransformed\ data = \exp [\log (C_n^2 * 10^{12})] * 10^{-12} m^{-2/3}. \quad (4.3)$$

This section presents results in relation to the EXPERT climate and season. Recall the usage of the term “mean” in this context refers to the mean value of the span of confidence intervals and not to the 50<sup>th</sup> percentile turbulence values. This term is used with both the Mode and 50<sup>th</sup> percentile data. Untransforming the data returns a lognormal distribution to the confidence interval span. In this regard, the mean value represents the mode value of each lognormal range of confidence intervals.

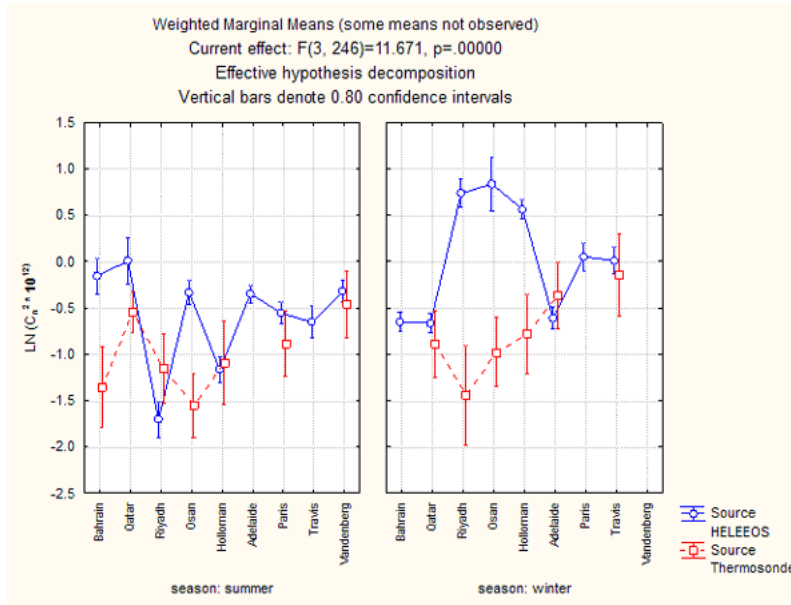


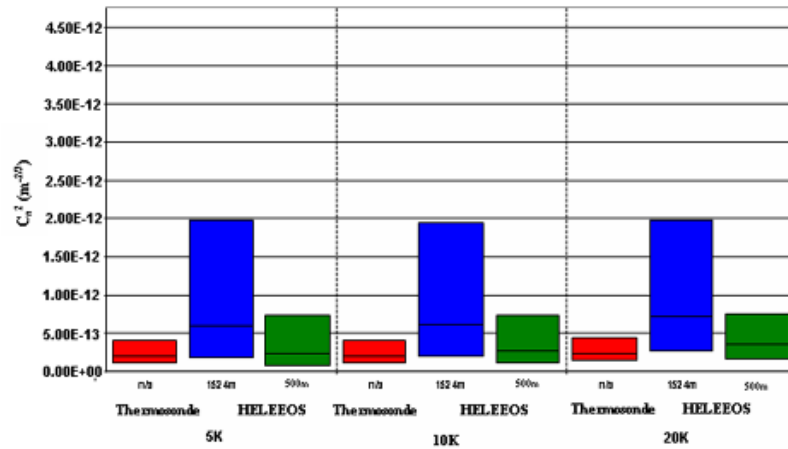
Figure 4.5: Weighted marginal means plot of the effects of Season and Location on the HELEEOS and thermosonde path-integrated  $C_n^2$  values. The results are similar to the least squares means plot of the previous figure.

The terminology may be confusing, and it is important to realize the proper definitions in this context. In all the following Figures, the y-axis is the untransformed path-integrated  $C_n^2$  values, with bar charts indicating the upper and lower limits of the 80% confidence intervals. In addition, the discussions reference the confidence intervals in conjunction with the Mode and 50<sup>th</sup> percentile turbulence profiles. It is vitally important to note the proper references to avoid confusion.

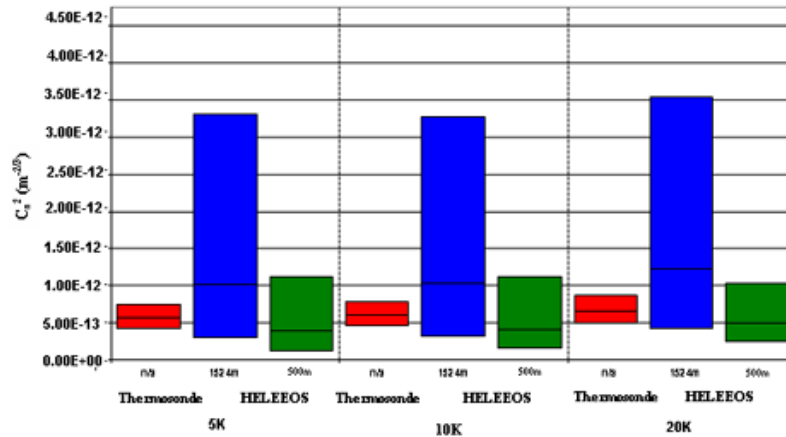
The untransformed data represents the truest estimation of the null hypothesis. In the previous section, the transformation enhanced the statistical differences within the datasets. Results in this section scale these larger variations to identical units, and reduce the amount of statistical variability. These results present the data in comparable values and emphasize the similarity in the data.

4.3.2.1 *Desert Summer Mode and 50<sup>th</sup> Percentile.* Figure 4.6(a) and (b) depicts the final results for the HELEEOS Desert Summer Mode and 50<sup>th</sup> percentile turbulence profiles respectively. These charts incorporate the results from all

three desert sites used in this research. The results represent the knowledge garnered from a factorial design of three Desert Summer sites, but the confidence intervals can be directly applied to the Climatological  $C_n^2$  profiles for other HELEEOS Desert Summer sites.



(a)



(b)

Figure 4.6: Final results for Desert Summer Mode (plot (a)) and 50<sup>th</sup> percentile (plot (b)) turbulence profiles. Note the lognormal distribution of the confidence intervals, consistent with naturally occurring distributions of atmospheric turbulence values.

In Figure 4.6, the confidence intervals exhibit the same lognormal patterns of the original thermosonde and HELEEOS  $C_n^2$  distributions. The middle line in each bar graph represents the mean value of the distribution (the mode value of the span), and



the portions of the graphs above and below the mean value represent the respective upper and lower 80% confidence intervals. Intuitively, these Figures exhibit expected behaviors. The default HELEEOS boundary layer value, 1524 m, exhibits the largest confidence interval ranges, and the 500 m boundary layer results exhibit the least variability in the confidence interval range. In all altitude cases, the 500 m boundary layer values are statistically equivalent to the thermosonde data, with tightly spaced means and acceptable confidence intervals. The HELEEOS confidence intervals for the Desert mode and 50<sup>th</sup> percentile turbulence profiles are numerically tabulated in Table 4.1 for both the Desert Summer and Desert Winter seasons.

*4.3.2.2 Desert Winter Mode and 50<sup>th</sup> Percentile.* Figure 4.7(a) and (b) show the results of the HELEEOS and thermosonde Desert Winter analysis for the Mode and 50<sup>th</sup> percentile turbulence profiles. These charts incorporate the results from all three desert sites used for this research. The results represent the knowledge garnered from a factorial design of three Desert Winter sites, but the confidence intervals can be directly applied to the Climatological  $C_n^2$  profiles for other HELEEOS Desert Winter sites.

These figures also exhibit acceptable boundary layer characteristics. However, in the case of the Desert Winter, the 1524 m boundary layer values exhibit greater variability than the Desert Summer case for the same boundary layer. This is also true for the 500 m boundary layer values at all altitudes. As is the case for the Desert Summer profiles, the 500 m boundary layer values are the most statistically equivalent to the thermosonde data.

Some observations are worth noting for the Desert Winter HELEEOS turbulence profiles. First, the variability in the means for the HELEEOS Mode turbulence profiles increases with height for both boundary layer conditions, whereas the thermosondes remain fairly consistent for these same conditions. The datasets become statistically different at 20k ft. Within the 5k and 10k ft layers, the means correlate well to the thermosonde means. The deviation at 20k ft may be indicative of variations in

Table 4.1: HELEEOS 80% Confidence Intervals (CI) for ExPERT Desert Sites

HELEEOS Mode Turbulence Profile					
Season	Alt (ft)	Boundary Layer	Mean Value	Lower 80% CI	Upper 80% CI
Summer	5k	1524m	$5.9447 \times 10^{-13}$	$1.7885 \times 10^{-13}$	$1.9428 \times 10^{-12}$
		500m	$2.4230 \times 10^{-13}$	$8.0202 \times 10^{-14}$	$7.2705 \times 10^{-13}$
	10k	1524m	$6.1902 \times 10^{-13}$	$1.9733 \times 10^{-13}$	$1.9759 \times 10^{-12}$
		500m	$2.6802 \times 10^{-13}$	$9.8803 \times 10^{-14}$	$7.3199 \times 10^{-13}$
	20k	1524m	$7.2354 \times 10^{-13}$	$2.6393 \times 10^{-13}$	$1.9835 \times 10^{-12}$
		500m	$3.5285 \times 10^{-13}$	$1.6740 \times 10^{-13}$	$7.4375 \times 10^{-13}$
Winter	5k	1524m	$7.9546 \times 10^{-13}$	$2.7628 \times 10^{-13}$	$2.2903 \times 10^{-12}$
		500m	$4.3382 \times 10^{-13}$	$1.9963 \times 10^{-13}$	$9.4275 \times 10^{-13}$
	10k	1524m	$8.8068 \times 10^{-13}$	$3.2907 \times 10^{-13}$	$2.3570 \times 10^{-12}$
		500m	$5.1018 \times 10^{-13}$	$2.5876 \times 10^{-13}$	$1.059 \times 10^{-12}$
	20k	1524m	$1.1011 \times 10^{-12}$	$4.7248 \times 10^{-13}$	$2.5659 \times 10^{-12}$
		500m	$6.6015 \times 10^{-13}$	$3.6404 \times 10^{-13}$	$1.1971 \times 10^{-12}$
HELEEOS 50 <sup>th</sup> Percentile Turbulence Profile					
Season	Alt (ft)	Boundary Layer	Mean Value	Lower 80% CI	Upper 80% CI
Summer	5k	1524m	$1.0009 \times 10^{-12}$	$3.0257 \times 10^{-13}$	$3.3112 \times 10^{-12}$
		500m	$3.7966 \times 10^{-13}$	$1.2918 \times 10^{-13}$	$1.1158 \times 10^{-12}$
	10k	1524m	$1.0314 \times 10^{-12}$	$3.2535 \times 10^{-13}$	$3.2694 \times 10^{-12}$
		500m	$4.1148 \times 10^{-13}$	$1.5191 \times 10^{-13}$	$1.1146 \times 10^{-12}$
	20k	1524m	$1.2213 \times 10^{-12}$	$4.2123 \times 10^{-13}$	$3.5411 \times 10^{-12}$
		500m	$5.0029 \times 10^{-13}$	$2.4221 \times 10^{-13}$	$1.0333 \times 10^{-12}$
Winter	5k	1524m	$1.2913 \times 10^{-12}$	$4.0425 \times 10^{-13}$	$4.1249 \times 10^{-12}$
		500m	$6.4817 \times 10^{-13}$	$2.6196 \times 10^{-13}$	$1.6038 \times 10^{-12}$
	10k	1524m	$1.4019 \times 10^{-12}$	$4.6688 \times 10^{-13}$	$4.2097 \times 10^{-12}$
		500m	$7.4740 \times 10^{-13}$	$3.3185 \times 10^{-13}$	$1.6833 \times 10^{-12}$
	20k	1524m	$1.7298 \times 10^{-12}$	$6.4245 \times 10^{-13}$	$4.6576 \times 10^{-12}$
		500m	$9.4746 \times 10^{-13}$	$4.5407 \times 10^{-13}$	$1.9770 \times 10^{-12}$

the Desert upper air look-up tables. However, this cannot be fully substantiated by this chart. The 50<sup>th</sup> percentile turbulence profiles do not exhibit this same behavior, pointing to specific causes within the Mode turbulence Climatological  $C_n^2$  calculations. The 500 m boundary layer means are statistically equivalent for all 50<sup>th</sup> percentile turbulence profile altitudes of interest.

Secondly, the upper bounds for the HELEEOS profiles double in magnitude from the Mode turbulence profile to the 50<sup>th</sup> percentile turbulence profiles at the 1524 m boundary layer. This points to a widening of the lognormal distribution

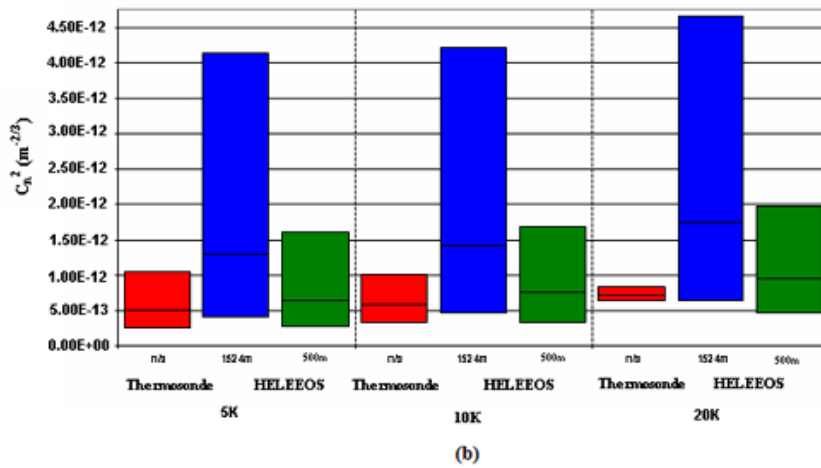
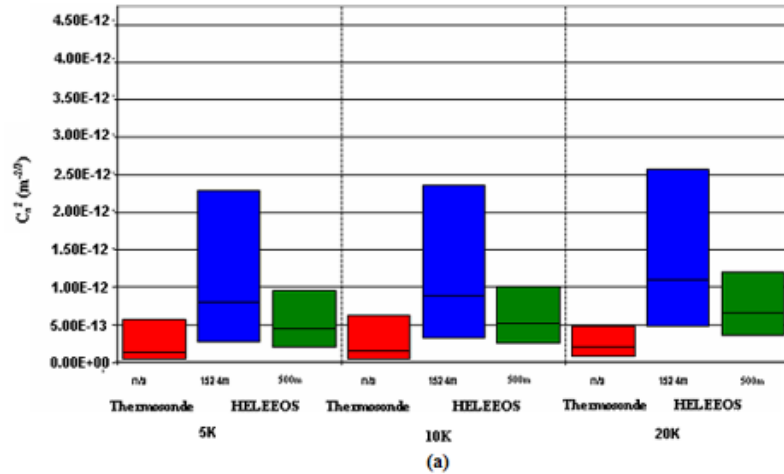


Figure 4.7: Final results for Desert Winter Mode (plot (a)) and 50<sup>th</sup> percentile (plot (b)) turbulence profiles. Note the lognormal distribution of the confidence intervals, consistent with naturally occurring distributions of atmospheric turbulence values.

curve between the mode value and the 50<sup>th</sup> percentile value for the Desert Winter sites. Recall these original lognormal distribution fits were chiefly derived from a limited set of available wintertime desert thermosonde campaigns. This research also contained limited wintertime thermosondes, as evidenced in Table 3.2. The original work on the Climatological  $C_n^2$  profiles fit the data to a sparse number of thermosondes resulting in non-ideal distribution curves. In some cases, less than ten data elements contributed to the original lognormal fits. This sparsity of data clearly surfaces in these charts. However, it is also worth noting that even with these less than ideal

distributions, the 50<sup>th</sup> percentile turbulence profiles remain statistically equivalent to the thermosonde data at all altitudes of interest.

*4.3.2.3 Mid-latitude Winter Mode and 50<sup>th</sup> Percentile.* Figure 4.8 displays the HELEEOS Mid-latitude Winter results. These charts incorporate the results from the seven Mid-latitude sites used throughout this research effort. The results represent the knowledge garnered from a factorial design of seven Mid-latitude Winter sites, but the confidence intervals can be directly applied to the Climatological  $C_n^2$  profiles for other HELEEOS Mid-latitude Winter sites. Table 4.2 lists the numerical outcomes of the Mid-latitude analysis for both the Winter and Summer seasons.

Overall, these results reflect consistencies with the previous charts - the 1524 m boundary layer exhibits the greatest variability and the confidence intervals reflect the lognormal dependencies within in the data. However, the data do exhibit some irregularities, even with the thermosonde data. Figure 4.8 (a) shows inconsistencies in the data for the Mode turbulence profiles for both the 1524 m and 500 m boundary layers. The HELEEOS Mode turbulence profiles and the thermosonde data match closely for a 5k ft altitude and 500 m boundary layer, but deviate statistically for the 10k ft and 20k ft altitudes. Across all altitudes, the means increase steadily with increasing altitude. This is not the case for the 50<sup>th</sup> percentile data for the 500 m boundary layers, where the means remain statistically equivalent for all altitudes of interest. In all the 50<sup>th</sup> percentile altitude cases, HELEEOS accurately reproduces the thermosonde data for the 500 m boundary layer vertical profiles. However, the 1524 m boundary layer means also increase with height. As mentioned earlier, this may point to variations in the free atmosphere look-up tables, but this cannot be stated outright without additional information.

Once again, the 1524 m boundary layer data display more pronounced variability as expected. The 1524 m boundary layer confidence intervals are acceptable for both the mode and 50<sup>th</sup> percentile turbulence profiles since there are no validation data to compare these results to. With large daytime variations expected in  $C_n^2$  values,

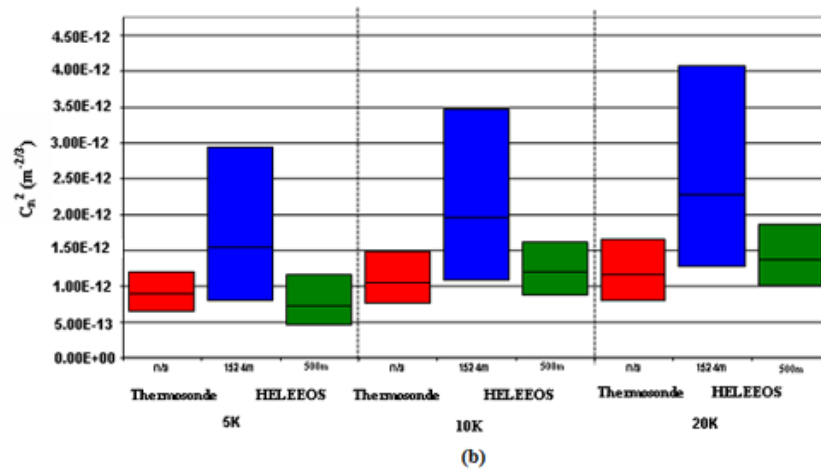
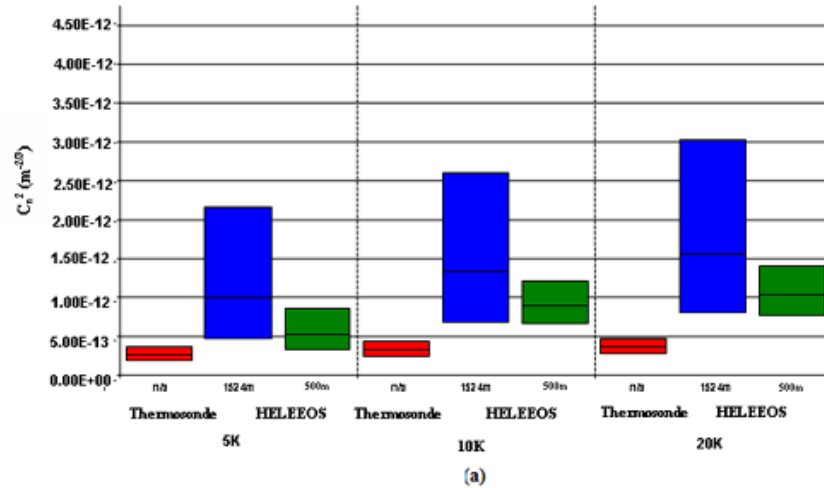


Figure 4.8: Final results for Mid-latitude Winter Mode (plot (a)) and 50<sup>th</sup> percentile (plot (b)) turbulence profiles. Note the familiar lognormal distribution of the confidence intervals, consistent with naturally occurring distributions of atmospheric turbulence values.

particularly near the surface of the earth where dynamic mixing is at a maximum, these confidence intervals are considered acceptable.

Figure 4.8 (a) shows an interesting characteristic in the Mode thermosonde data. All three altitudes reflect very tight confidence intervals. The narrow confidence intervals for the Mode turbulence values are actually artificially smaller than the 50<sup>th</sup> percentile turbulence values. This is due to the method used to compute the Mode value in Matlab<sup>®</sup>. The mid-latitude winter dataset consisted of only three campaigns - Osan, Three Rivers and Holloman. Due in part to limited sample sizes, particularly

with the Three Rivers campaign, Matlab<sup>®</sup> mode calculations produced lower Mode path-integrated values than the 50<sup>th</sup> percentile (average) path-integrated values, and larger margins of error for the smaller sample sizes. This resulted in the tight confidence intervals depicted in the plots. The mean calculations in Matlab<sup>®</sup> produced more precise results. It is important to remember these results are the combined results from all three Mid-latitude Winter campaigns, regardless of sample size, and the variability of the confidence intervals reflects the overall statistical differences seen in each campaign.

The HELEEOS methodology for computing the free atmosphere Climatological  $C_n^2$  profiles may also contribute to the increasing means for the 1524 m boundary layer. Once a boundary layer is selected, HELEEOS uses a temperature correlation for the Climatological  $C_n^2$  values in the free atmosphere. These temperature correlations come from standard atmosphere temperatures curves, but are matched to Climatological  $C_n^2$  values from the measured thermosonde data.

The profiles for all HELEEOS Mid-latitude sites are based on thermosonde data collected at Osan AB, South Korea during November 1999 and February 2000. There exists two distinctly different airmasses over Korea during these months. In the fall and early winter, the Korean atmosphere is continental in nature, with decreasing temperatures at all levels as colder air migrates across the peninsula. By February, however, the airmass becomes largely arctic in nature, caused by continual entrainment of very cold air from Siberia and Upper Mongolia across this region. The inclusion of temperatures representative of two different airmasses near the surface may have created a broader temperature distribution and resulted in a subtle bias in the Climatological  $C_n^2$  values. Figure 4.8 (a) and to some degree (b) shows this increasing bias in the means for both the Mode and 50<sup>th</sup> percentile turbulence profiles. Since all mid-latitude sites use these data to derive site-specific Climatological  $C_n^2$  profiles, they are likewise skewed to greater Climatological  $C_n^2$  values.

Another plausible explanation for these discrepancies may be that the look-up tables are sparsely populated for the Mid-Latitude Winter, particularly for extremely low temperatures. When this occurs, HELEEOS selects the nearest neighbor data point within the look-up table for the upper air calculations. If the predominate temperatures used to correlate the Climatological  $C_n^2$  values to the standard atmosphere is the colder arctic (February) temperatures, the nearest neighbor selections in HELEEOS may result in this skewing to the higher Climatological  $C_n^2$  values seen in the plots.

Table 4.2 lists the mean values of each profile along with the values for the corresponding confidence intervals for both the Mid-Latitude Winter and Summer Mode and 50<sup>th</sup> percentile turbulence profiles.

*4.3.2.4 Mid-latitude Summer Mode and 50<sup>th</sup> Percentile.* Figure 4.9 shows the final results of the HELEEOS Mid-latitude Summer Mode and 50<sup>th</sup> percentile turbulence profiles analysis. These charts incorporate the results from the seven Mid-latitude sites used throughout this research effort. The results represent the knowledge gained from a factorial design of seven Mid-latitude Summer sites, but the confidence intervals can be directly applied to the Climatological  $C_n^2$  profiles for other HELEEOS Mid-latitude Summer sites.

At first glance, these results appear very good. However, these results are somewhat misleading. At once, the reader will notice the smaller confidence intervals for the Mid-latitude Summer sites. Another obvious difference is the apparent lack of lognormal distributions in the confidence ranges at both the 1524 m and 500 m boundary layers. In addition, the 500 m boundary layer confidence ranges exceed those of the 1524 m boundary layer. This clearly goes against the physical intuition of the boundary layers and the strength of turbulence associated with each boundary layer.

These appear to be discrepancies in the HELEEOS turbulence profiles, but in reality, they are a manifestation of an inherent limitation in the current HELEEOS

Table 4.2: HELEEOS 80% Confidence Intervals (CI) for ExPERT Mid-Lat Sites

HELEEOS Mode Turbulence Profile					
Season	Alt (ft)	Boundary Layer	Mean Value	Lower 80% CI	Upper 80% CI
Summer	5k	1524m	$3.0433 \times 10^{-13}$	$2.4523 \times 10^{-13}$	$3.7769 \times 10^{-13}$
		500m	$4.3519 \times 10^{-13}$	$3.3392 \times 10^{-13}$	$5.6716 \times 10^{-13}$
	10k	1524m	$4.2692 \times 10^{-13}$	$3.5427 \times 10^{-13}$	$5.1446 \times 10^{-13}$
		500m	$5.5648 \times 10^{-13}$	$4.3709 \times 10^{-13}$	$7.0850 \times 10^{-13}$
	20k	1524m	$5.1385 \times 10^{-13}$	$4.2437 \times 10^{-13}$	$6.2220 \times 10^{-13}$
		500m	$6.5431 \times 10^{-13}$	$5.1909 \times 10^{-13}$	$8.2477 \times 10^{-13}$
Winter	5k	1524m	$9.9423 \times 10^{-13}$	$4.5555 \times 10^{-13}$	$2.1699 \times 10^{-12}$
		500m	$5.2703 \times 10^{-13}$	$3.2536 \times 10^{-13}$	$8.5370 \times 10^{-13}$
	10k	1524m	$1.3319 \times 10^{-12}$	$6.8467 \times 10^{-13}$	$2.5909 \times 10^{-12}$
		500m	$8.9344 \times 10^{-13}$	$6.6222 \times 10^{-13}$	$1.2054 \times 10^{-12}$
	20k	1524m	$1.5609 \times 10^{-12}$	$8.0275 \times 10^{-13}$	$3.0350 \times 10^{-12}$
		500m	$1.0394 \times 10^{-12}$	$7.6698 \times 10^{-13}$	$1.4085 \times 10^{-12}$
HELEEOS 50 <sup>th</sup> Percentile Turbulence Profile					
Season	Alt (ft)	Boundary Layer	Mean Value	Lower 80% CI	Upper 80% CI
Summer	5k	1524m	$5.4746 \times 10^{-13}$	$4.3965 \times 10^{-13}$	$6.8171 \times 10^{-13}$
		500m	$5.7168 \times 10^{-13}$	$4.5571 \times 10^{-13}$	$7.1717 \times 10^{-13}$
	10k	1524m	$6.9901 \times 10^{-13}$	$5.7635 \times 10^{-13}$	$8.4777 \times 10^{-13}$
		500m	$7.1745 \times 10^{-13}$	$5.7676 \times 10^{-13}$	$8.9247 \times 10^{-13}$
	20k	1524m	$8.3881 \times 10^{-13}$	$6.8663 \times 10^{-13}$	$1.0247 \times 10^{-12}$
		500m	$8.3647 \times 10^{-13}$	$6.8331 \times 10^{-13}$	$1.0240 \times 10^{-12}$
Winter	5k	1524m	$1.5330 \times 10^{-12}$	$8.0027 \times 10^{-13}$	$2.9366 \times 10^{-12}$
		500m	$7.2742 \times 10^{-13}$	$4.5971 \times 10^{-13}$	$1.1510 \times 10^{-12}$
	10k	1524m	$1.9427 \times 10^{-12}$	$1.0891 \times 10^{-13}$	$3.4653 \times 10^{-12}$
		500m	$1.1919 \times 10^{-12}$	$8.7734 \times 10^{-13}$	$1.6192 \times 10^{-12}$
	20k	1524m	$2.2819 \times 10^{-12}$	$1.2798 \times 10^{-13}$	$4.0689 \times 10^{-12}$
		500m	$1.3764 \times 10^{-12}$	$1.0170 \times 10^{-13}$	$1.8628 \times 10^{-12}$

Summer look-up tables. These are best explained by example. Recall that HELEEOS calculates a vertical profile by correlating surface temperatures and relative humidities to a user-defined relative humidity percentile. This test used the 50%, or average, percentile, corresponding to a 50% temperature percentile as well. From these two percentiles, HELEEOS calculates a dewpoint and lapses the temperature and dewpoint curves at either a moist adiabatic lapse rate ( $6.5 \text{ }^\circ\text{C}/1000 \text{ m}$ ) or a dry adiabatic lapse rate ( $10 \text{ }^\circ\text{C}/1000 \text{ m}$ ), depending on the seasonal conditions. At each point in the vertical profile through the boundary layer, HELEEOS recalculates a new tempera-



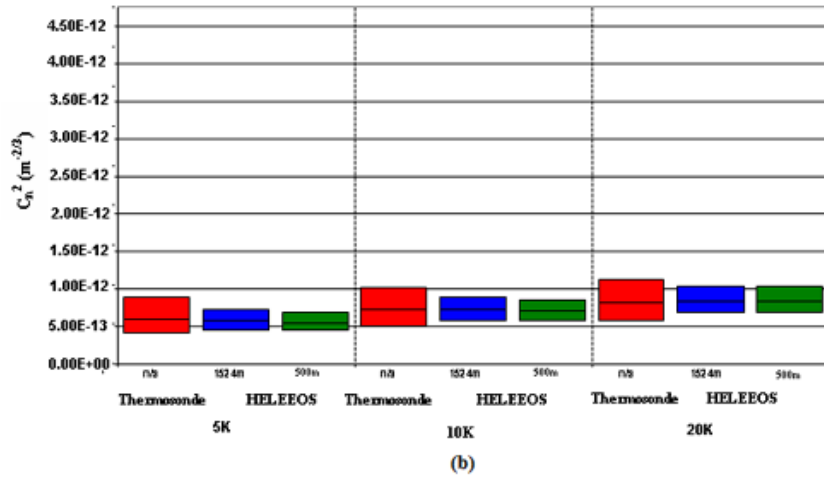
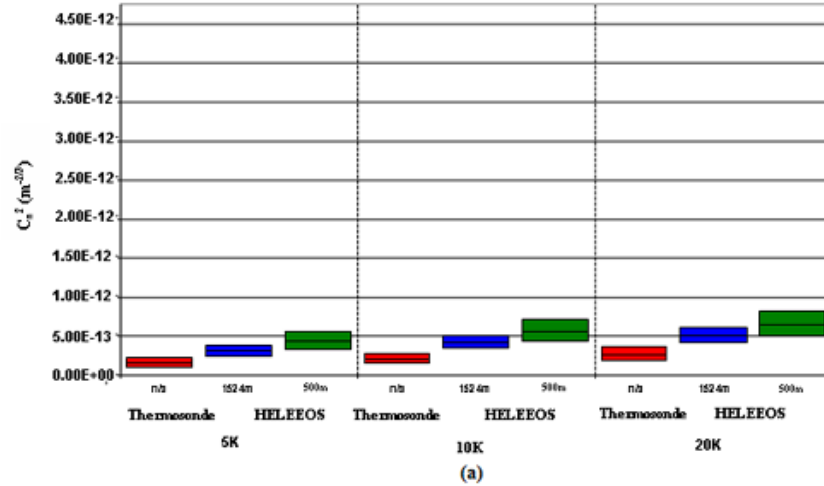


Figure 4.9: Final results for Mid-latitude Summer Mode (plot (a)) and 50<sup>th</sup> percentile (plot (b)) turbulence profiles.

ture and dewpoint from these lapsed values, and recomputes a corresponding relative humidity. HELEEOS then references the look-up tables for this calculated relative humidity and extracts a Climatological  $C_n^2$  value for that given altitude.

The limitations of HELEEOS arise when the reference look-up tables have sparsely populated relative humidity bins. Also recall that HELEEOS uses two boundary layer slabs - one from the surface to 60 m and the other from 60 m to the top of the selected boundary layer. For a 500 m boundary, only a 440 m slab exists with limited data before the free atmosphere Climatological  $C_n^2$  values populate the

remaining vertical path. However, for the 1524 m boundary, this slab is 1484 m thick. HELEEOS smoothly interpolates between the 60 m data point and the 1524 m data point, with no variations showing demonstrated in the profile. The original reasoning for selecting these two boundary layer slabs was to break up the boundary layer in more representative layers and also to attempt to address the lack of thermosonde data within the first 5k ft of the atmosphere. As a consequence of this methodology, the 500 m boundary layer turbulence profiles show considerable variation in the first 5,000 ft of the atmosphere due to the extensions of the free atmosphere; the 1524 m boundary layer profiles do not. Figure 4.10 plainly shows this limitation in the 10k ft Mid-latitude turbulence profiles. The red line, the 1524 m boundary layer turbulence profile, smoothly lapses from 60 m through 1524 m with little variation in profile. As a consequence, the 500 m boundary layer path-integrated  $C_n^2$  values are greater in magnitude than the corresponding 1524 m boundary layer path-integrated  $C_n^2$  values.

It is also interesting to note the peak near 1000m in the 500 m boundary layer profile. This naturally occurring inversion or capping layer is a feature often seen in nighttime thermosonde measurements. HELEEOS accurately replicates this inversion layer; this underscores the versatility of the HELEEOS engagement package.

#### ***4.4 Application of the Model***

The results of this research effort demonstrate the accuracy of the HELEEOS optical turbulence model. However, before the HELEEOS Climatological  $C_n^2$  model gains credence as an improved optical turbulence, it must show similar or improved results as compared to the empirical optical turbulence standards such as Hufnagel-Valley 5/7 or Clear 1.

The simulations in this research utilize accepted mainstream wave optics modeling functions found in **ATMTools**<sup>®</sup>. It uses the **ATMTools**<sup>®</sup> *TBWaveCalc* function to model the propagation path of an ATL-like high energy laser. This function requires several input structures - geometry, atmosphere, laser, engagement, and propagation controls.

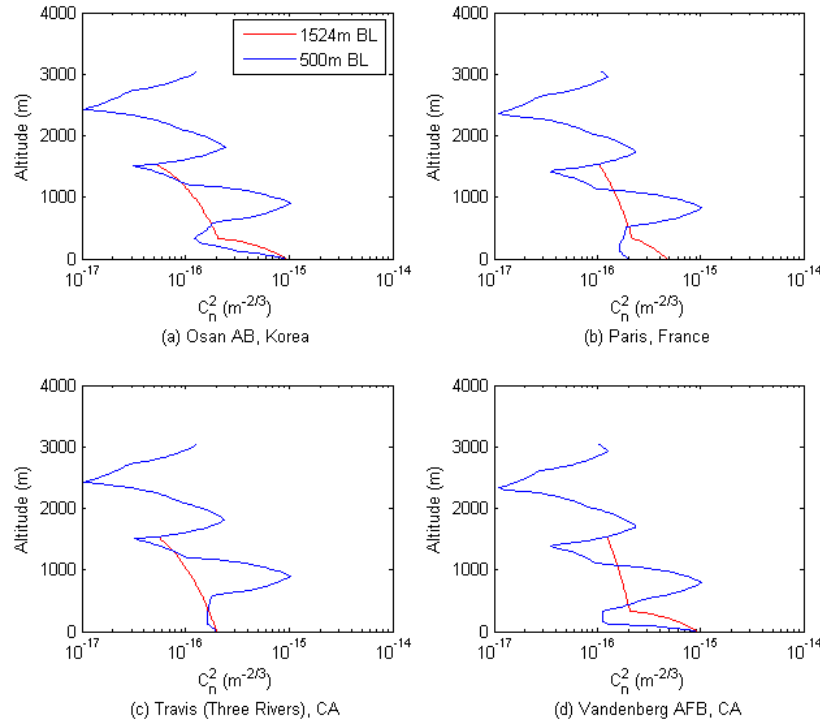


Figure 4.10: Mid-latitude Summer sites vertical Climatological  $C_n^2$  profiles, sfc-10k ft. The 500 m boundary layer (BL) is indicated by the blue line and the 1524 m boundary is indicated by the red line. In all cases of the Mid-latitude Summer profiles, the nighttime vertical Climatological  $C_n^2$  profile (500 m BL) is stronger than the daytime vertical Climatological  $C_n^2$  profile (1524 m BL). The subplots are shown from the sfc-10k ft for clarity of the boundary layer.

The atmosphere structure requires a turbulence model. Usually this is either HV57 or Clear 1, but the focus of the modeling is to validate the HELEEOS Climatological  $C_n^2$  model. Therefore, these simulations substitute the HELEEOS Climatological  $C_n^2$  model in place of the HV57 or Clear 1 models. The wave optics simulations require only a turbulence model, and substituting the HELEEOS Climatological  $C_n^2$  model into the atmosphere structure ensures the laser is propagated through multiple phase screens using the Climatological  $C_n^2$  values as the baseline  $C_n^2$  values within the phase screens.

This modeling simulation assumes a specific geometry. It models an ATL-like platform orbiting at 10k ft, firing on a surface target 6000 m downrange, for a total

slant propagation path of 6731 m. The ATL's forward propagation vector is easterly at 100 m/s. The target's forward propagation vector is east at 10 m/s.

The laser is a 50 kW laser emitting at 1.325  $\mu\text{m}$ ; the aperture is 0.5 m with a 0.1 m center obscuration. The laser beam is modeled as a Gaussian beam focused at the target, with a  $\sigma$  value of 0.17678 m. The propagation path is modeled with a spherical  $r_0$  at the receiver of 11.19 cm, and a  $\theta_{0max}$  of 82.094  $\mu\text{rad}$ .

The `ATMTools®wtgeomprop` function calculated the wave optics simulations propagation controls. The meshgrid spacing is 256 x 256 pixels, with a differential spacing of 0.0081 m per pixel. The propagation model uses 100 phase screens, with a distinct  $C_n^2$  value defined at each phase screen, resulting in a  $C_n^2$  matrix of 100 elements. The simulations propagate a HEL beam using the HV57, Clear 1, and HELEEOS Climatological  $C_n^2$  models as the input turbulence models.

Several parameters could be calculated from the wave optics simulations, but this effort restricts the results to a single metric of long-term spot size. The long-term spot size is a time integration of 100 propagation realizations representing a total time on target of 45.6 ms. Thermal blooming was not considered in these propagations. The wave optics simulations realize the analytic form of Equation 2.17. The time-integrated spot size increases beyond the diffraction limit as the turbulence increases. Each long-term spot is calculated from Gaussian best-fit for both the P-axis (direction perpendicular to target forward motion) and T-axis (direction transverse to target forward motion) intensity lobes. Each lobe is measured at the  $1/e^2$  position of the best fit Gaussian. The long-term spot is realized using

$$spot\ size = \sqrt{\sigma_P^2 + \sigma_T^2} \quad (4.4)$$

where  $\sigma_P$  is the spot size radius of the  $1/e^2$  position in the P-axis lobe, and  $\sigma_T$  is the spot size radius of the  $1/e^2$  position in the T-axis lobe.

The ABL program uses 2 x Clear 1 as the baseline turbulence model for research purposes. Doubling the strength of the Clear 1 model produces very strong surface

optical turbulences. However, since this is the baseline model for ABL research, it is included here for reference. Recall the Clear 1 model is not defined below 1230 m. **ATMTools**<sup>®</sup> calculates an extension of the model to the surface with an extrapolation of the model between 2130m and 1230m. [16] Figure 4.11 shows the results of a 45.6 ms realization using the Clear 1 optical turbulence model in **ATMTools**<sup>®</sup>. The long-term spot is 12.4 cm. Figure 4.12 shows the results of identical propagations using HV57. Here the long-term spot size is 10.7 cm.

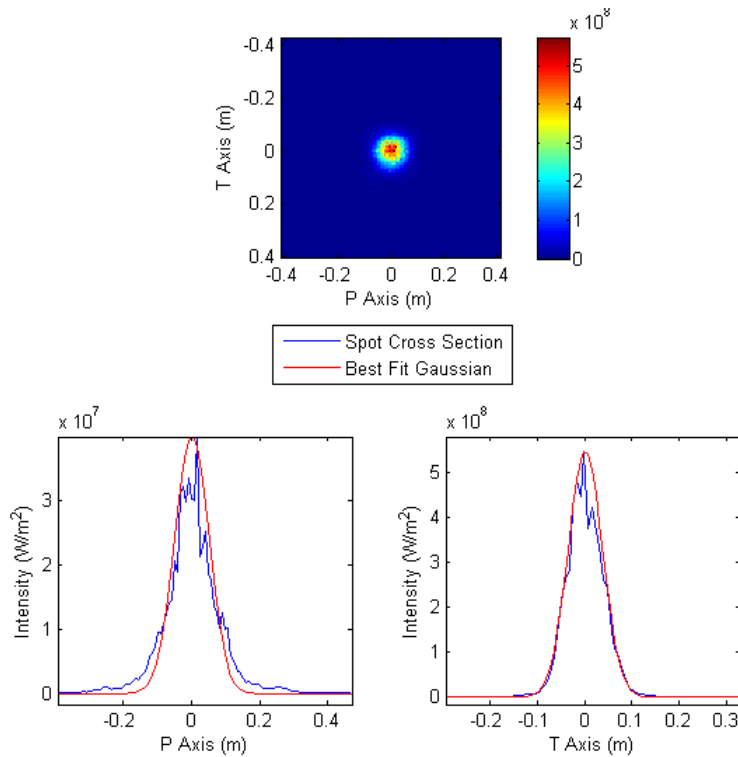


Figure 4.11: Long-term spot size 45.6 ms realization using the Clear 1 optical turbulence model. The long-term spot size is 12.4 cm.

Figure 4.11 points out the overall impact of increased turbulence. The spot size clearly shows an aberrated phase front and a significantly broadened spot size, well beyond the diffraction limit. The P-axis and T-axis lobes are poorly formed as a result of the phase front aberrations. The intensity pattern within the spot size is randomly distributed, resulting in less power per unit area. The HV57 spot size in Figure 4.12 shows less aberration and a more uniform distribution across the target.

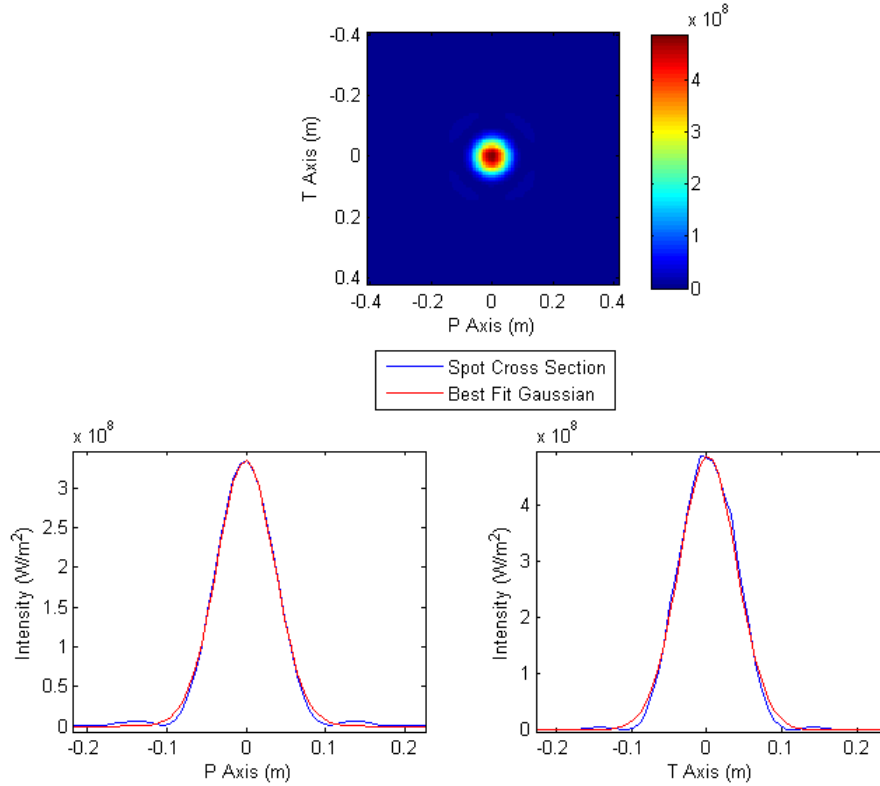


Figure 4.12: Long-term spot size 45.6 ms realization using the HV57 optical turbulence model. The long-term spot size is 10.7 cm.

There are still aberrations in the spot, but they are considerably less than the 2 x Clear 1 model. In all these charts, the spot size cross section is the cross sectional view across the centroid of the respective lobe.

Development of the Clear 1 empirical model was based on data gathered in the New Mexico desert. [23] Comparison studies of HV57 to the New Mexico data showed that the model performed poorly under low tropospheric winds. [2] Recall the HV57 model is a parametric model requiring inputs for mid-tropospheric rms wind speed and a nominal surface  $C_n^2$  value. This research effort uses the Holloman AFB, NM Climatological  $C_n^2$  data to provide a realistic assessment of the HELEEOS optical turbulence profiles against the Clear 1 model. It also uses the Osan AB, Korea Climatological  $C_n^2$  data in a comparative analysis against the HV57 parametric optical turbulence model.

Figures 4.13 and 4.14 show the results of the propagation simulations using the HELEEOS Climatological  $C_n^2$  Mode turbulence profile for Holloman AFB, NM. In Figure 4.14 the summer long-term spot size is 10.4 cm; in Figure 4.13 the winter long-term spot size is 10.3 cm. The HELEEOS Climatological  $C_n^2$  modeling exhibits nearly a 17% reduction in spot size when compared to the 2 x Clear 1 model. The Figures depict a uniform intensity distribution across the centroids of the spot size cross sections, and result in more power per unit area.

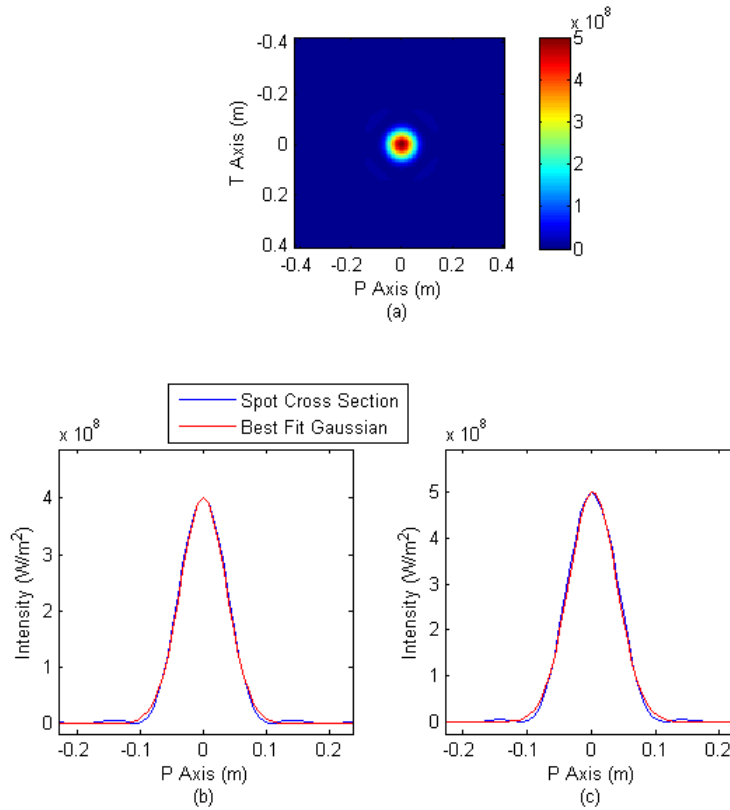


Figure 4.13: Long-term spot size 45.6 ms realization using the Winter HELEEOS Climatological  $C_n^2$  Mode turbulence profile for Holloman AFB, NM . The long-term spot size is 10.3 cm.

These spots are likewise smaller than the spot size formed from the propagations using HV57. However, the HELEEOS Climatological  $C_n^2$  spot sizes are not significantly smaller than the HV57 spot size for the same propagation parameters. This begs an answer to the question of "why HELEEOS?" The power of HELEEOS is its

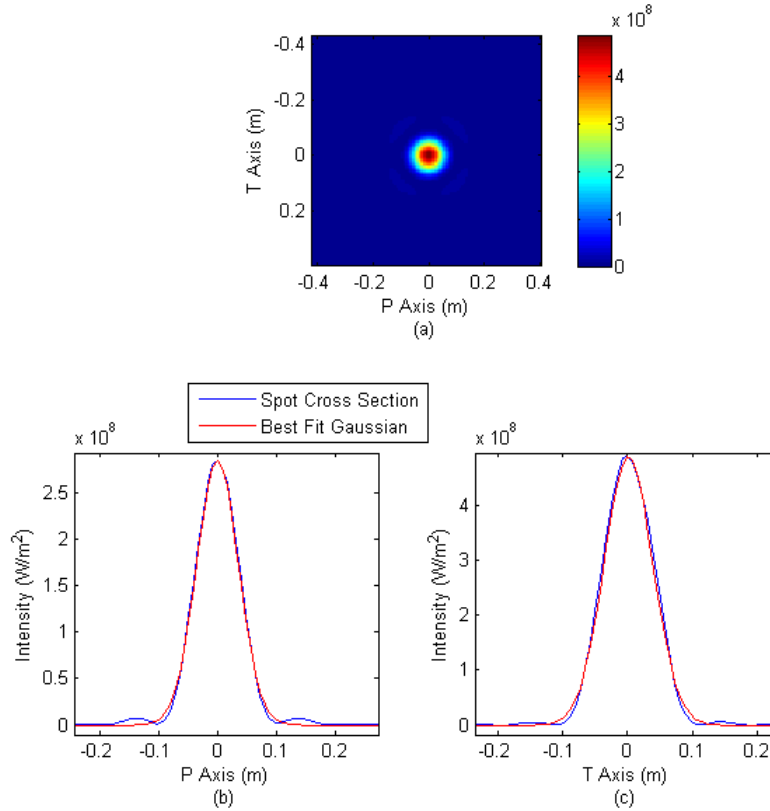


Figure 4.14: Long-term spot size 45.6 ms realization using the Summer HELEEOS Climatological  $C_n^2$  Mode turbulence profile for Holloman AFB, NM. The long-term spot size is 10.4 cm.

ability to accurately model seasonal variations in the optical turbulence fields, and its adaptability to all worldwide Mid-latitude and Desert sites through the probabilistic climatology of the ExPERT database. This powerful feature provides a tailor-made optical turbulence at a specific site, rather than a standard, empirical model designed to work only under strict atmospheric regimes. In addition, this simulation shows differences in the size of the spot size depending on the season. HV57 and Clear 1 do not afford this level of adaptability.

The results of a propagation run using the Osan AB, Korea Winter Climatological  $C_n^2$  Mode turbulence profile are shown in Figure 4.15. Again, HELEEOS shows improvement over HV57 under identical propagation parameters. The stronger Winter turbulence profiles produce a larger spot size than those from Holloman, con-



sistent with the results presented in Section 4.3.2. The previous discussion noted the larger values of the wintertime profiles, and this effect also arises in the propagation results. However, the HELEEOS Climatological  $C_n^2$  profile is a truer representation of the actual turbulence compared to the HV57 model. These results demonstrate the versatility and power of the HELEEOS Climatological  $C_n^2$  optical turbulence profiles.

Spot sizes increased with larger HELEEOS Climatological  $C_n^2$  turbulence percentiles. At Osan, the winter season spot size increased to 11.2 cm for the 80<sup>th</sup> percentile turbulence profile. The 80<sup>th</sup> percentile profiles at Holloman produced similar results, with the spot size in summer increasing to 10.9 cm and the winter spot size increasing to 11.1 cm. However, these spot sizes are still smaller than the spot sizes associated with the 2 x Clear 1 optical turbulence model. These results demonstrate that HELEEOS is a capable optical turbulence model suitable to research applications.

#### ***4.5 Overall Results***

The results of this analysis demonstrate the accuracy of the HELEEOS Climatological  $C_n^2$  profiles for a 500 m boundary layer. These profiles precisely replicate observed conditions, and validate the unique methodology of probabilistic climatology used to generate the Climatological  $C_n^2$  vertical profiles. The confidence intervals established in this research serve to characterize the expected path turbulence to within 80% confidence, that is, these results encapsulate the level of turbulences that can be expected 80% of the time. In addition, the modeling results reveal the suitability of the HELEEOS Climatological  $C_n^2$  model as a research model comparable to that of HV57, and even better suited compared to that of 2 x Clear 1. Furthermore, HELEEOS outperforms both empirical standards in modeling mid-tropospheric variations in the optical turbulence fields. This research also emphasizes HELEEOS' adaptability to many different locations in differing climatic regimes. This research effort also validates the method of probabilistic climatology used in HELEEOS. This

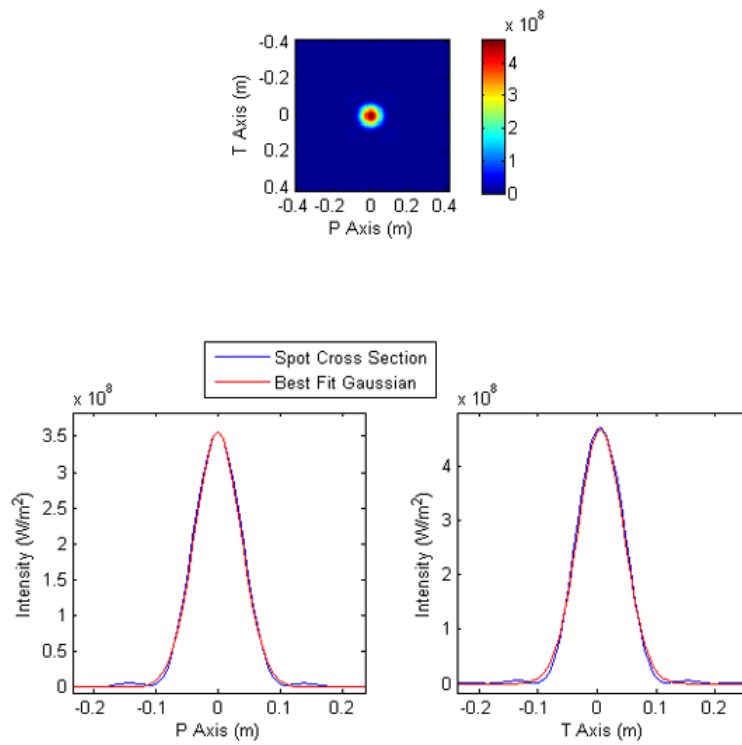


Figure 4.15: Long-term spot size 45.6 ms realization using the Winter HELEEOS Climatological  $C_n^2$  Mode turbulence profile for Osan AB, NM. The long-term spot size is 10.6 cm.

methodology is singular to HELEEOS; no other optical turbulence model incorporates environmental climatic data into its profiles.

## V. Conclusions and Recommendations

### 5.1 Research Conclusions

This research effort set out to achieve three goals: assess the performance of the HELEEOS Climatological  $C_n^2$  optical turbulence profiles, quantify confidence bounds on the path-integrated Climatological  $C_n^2$  vertical profiles, and test the HELEEOS Climatological  $C_n^2$  model against the current standard optical turbulence models. This research effort achieved satisfactory results for all three goals.

The 500 m boundary layer Climatological  $C_n^2$  profiles are the most accurate profiles HELEEOS currently offers. The HELEEOS default boundary layer (1524 m) exhibits larger confidence interval spans than the 500 m boundary layer, but this is expected since there are no current techniques to validate these daytime profiles. In the absence of daytime thermosonde data, the inference can be made that the 1524 m boundary layer profiles are reasonable facsimiles of the expected daytime optical turbulence. With a much greater confidence though, the nighttime 500 m boundary layer profiles generate statistically equivalent profiles to measured thermosonde data. These profiles closely replicate the conditions from the measured thermosonde data for each given site within the purview of this test. When taken as a path-integrated  $C_n^2$  value, these 500 m boundary layer profiles accurately reflect the prevailing conditions measured in thermosonde data. This is encouraging for the user since HELEEOS possesses the unique ability to project these vertical profiles globally, requiring only the site climatology to produce the profile. This measure of trust gives the HELEEOS user the confidence needed to predict optical turbulence at a specific site rather than relying on lesser suited empirical optical turbulence profiles.

The confidence intervals established in Tables 4.1 and 4.2 demonstrate an expected trend. The confidence intervals increase with larger Climatological  $C_n^2$  turbulence percentiles. Since this research did not assess the 80<sup>th</sup> through 99<sup>th</sup> turbulence percentiles, it can only be assumed, based on the trends between the Mode and 50<sup>th</sup> percentiles, that the confidence intervals grow larger with each increasing percentile.

The most accurate representation of the true thermosonde data is the Mode turbulence profile. Is is convenient this is the also the default turbulence percentile.

In order to properly exploit these turbulence profiles, the savvy user must be able to understand the importance of the path-integrated optical turbulence. For ATL applications, the path-integrated  $C_n^2$  value represents the sum total of the expected optical turbulence from a given altitude to the targets on the surface. The terminal phase of an ATL engagement encounters the greatest turbulence along that propagation path, resulting in both amplitude and phase distortions caused by the optical turbulence. For a user testing performance characteristics of the laser, the entire range of the 80% confidence intervals require testing. The lower confidence interval represents the least optical turbulence expected on the path, while the upper confidence interval represents the greatest optical turbulence expected along the propagation path (to within 80% confidence). This provides a range of optical turbulence strengths that can be fully examined by researchers to assess turbulence induced effects on the laser propagation. This research provides an avenue to assess optical turbulence as a range versus a specific value as given by empirical turbulence profiles. At first look, these ranges might appear to be excessively large. However, the thermosonde data itself also exhibit a similar spread for 80% confidence, particularly in the 50<sup>th</sup> percentile data. HELEEOS, at least for the 500 m turbulence profiles, accurately reproduces these ranges. Therefore, the values provided for the path-integrated Climatological  $C_n^2$  profiles can be considered the physical limits of the strength of the optical turbulence to within 80% confidence and bound by the weak turbulence regime. This is very important to ATL-type applications because it provides physical, deterministic numbers for weak turbulence conditions.

The upper bound is the most important. This represents the greatest extent of the expected optical turbulence. System performance parameters are often established based on extreme values of expected conditions. However, extreme values often translate into higher developmental costs. HELEEOS provides the 80% solution, based on a critical assessment of observed conditions, to better assist testers and developers in

characterizing the true optical turbulence at a given location. If HELEEOS can be utilized as the optical turbulence models in the research efforts, it may very well help to reduce costs by providing more realistic performance indicators.

These upper 80% confidence intervals are more suited to ATL applications rather than ABL applications. In the ABL program, the extreme turbulence condition is taken to be 2 x Clear 1, and this works well for upper atmospheric applications. However, this profile is not useful for surface applications without supplementing the model between 1230m and the surface. This region is not clearly defined by Clear 1, and the solution is often an adaptation of either the HV57 profile or an extrapolation of the Clear 1 model itself. The artificially biased 2 x Clear 1 profile produces much greater degradation effects, and these effects detract from its application to mid-tropospheric applications like the ATL. Reliance on this empirical standard will no doubt result in higher design and developmental costs. However, capitalizing on the more realistic HELEEOS profiles can help to reduce design, development and integrated testing costs.

A DOE-based factorial design proved to be the best approach for determining the statistical equivalence of the HELEEOS Climatological  $C_n^2$  profiles with the thermosondes. The results of this test explicitly demonstrate the power behind this proven test technique. ANOVA regression testing established the statistical equivalence of the two datasets, and solidified the HELEEOS methodology behind the Climatological  $C_n^2$  model. In addition, this research identified issues in HELEEOS, that, once fixed, will increase its usefulness. This research also validates the idea that probabilistic climatology can be conditionally correlated to the strength of optical turbulence for individual sites. This level of analysis firmly establishes confidence in the HELEEOS Climatological  $C_n^2$  model, and will hopefully generate user acceptance as well.

Finally, HELEEOS proved to be a viable optical turbulence model suitable for mainstream wave optics simulations. It compares well to the HV57 model, and routinely outperforms the ABL standard 2 x Clear 1 model. This opens the door to a

wider range of research areas. With the added advantage of accurately modeling the boundary layer and free atmosphere turbulence variations, HELEEOS could become a research tool commensurate with the empirical models. Assessing performance using these profiles can provide beneficial maximum and minimum metrics for parameters such as dwell time, Strehl ratio, scintillation and power in the bucket measurements.

## ***5.2 Recommendations and Future Work***

Recommendations mainly focus on two primary areas of concern: application of the data from this research and HELEEOS user friendliness and confidence.

The results of the research can be applied in three ways. First, change the default setting in HELEEOS to the most statistically equivalent profile. The combination of the HELEEOS Climatological  $C_n^2$  Mode turbulence profiles and the 500 m boundary layer with nighttime climatology proved to be the most accurate measure of the atmosphere at both Desert and Mid-latitude sites. The Desert profiles are spot on, and the Mid-latitude profiles are likewise statistically equivalent, but with slightly larger variations than the Desert profiles. However, the default time-of-day selection in HELEEOS automatically reverts to the 1524 m boundary layer. The first recommendation is to make the time of day selection default to the most reliable profile - the 500 m boundary layer. Changing the default time of day to coincide with the nighttime climatology ensures part-time users get the best possible product. The Mode turbulence profile is the current HELEEOS default, and should remain the default turbulence profile.

The results of this research can be applied in another way. This effort produced deterministic values for the 80% confidence intervals for a vertical, integrated path. Tabulate these results and include them as a reference in HELEEOS. Textbooks such as the ones cited in this thesis often relate optical turbulence strengths to the overall path-integrated strength. The confidence intervals in this thesis establish the upper bound for these strengths, and this is the metric most relevant to the researcher. There is really no way to precisely implement this table in the form of a

graphic the user can reference. However, modeling simulations often allow for scalar multipliers on the strength of turbulence. These upper bounds help to solidify these turbulence multipliers, and a reference table provides this needed information. The second recommendation is to include the results of Table 4.1 and 4.2 as a reference in HELEEOS.

It is possible, though, to depict the upper bounds in the form of a site-specific graphic. A simple Matlab<sup>®</sup> calculation produces the turbulence multiplier to use for the site. This multiplier, when applied to the Climatological  $C_n^2$  values, results in the vertical profile corresponding to the 80% confidence interval. Figure 5.1 shows an example of this 80% confidence interval profile.

In addition, the upper 80% confidence limits listed in Tables 4.1 and 4.2 ironically correspond to path-integrated values associated with other turbulence percentiles; however, there is not physical explanation for this coincidence. For example, the upper confidence limit on the Desert Summer profiles for 10k feet is  $7.3199 \times 10^{-13} \text{ m}^{-2/3}$ . The path-integrated values for the 50<sup>th</sup> percentile profiles for Bahrain, Qatar and Riyadh are  $6.74 \times 10^{-13}$ ,  $6.71 \times 10^{-13}$ , and  $6.29 \times 10^{-13} \text{ m}^{-2/3}$  respectively. While these values are not exactly, they most closely match the upper 80% confidence interval value for the Desert Summer profiles. These values are for the 500 m boundary layer only. The following combinations exist:

Upper 80% Confidence Interval	↔	HELEEOS Climatological $C_n^2$ Profile
Desert Summer	↔	50 <sup>th</sup> Percentile
Desert Winter	↔	90 <sup>th</sup> Percentile
Mid-latitude Summer	↔	80 <sup>th</sup> Percentile
Mid-latitude Winter	↔	50 <sup>th</sup> Percentile

These combinations are identical for all three altitudes. Combining the 80% confidence intervals and the corresponding Climatological  $C_n^2$  together on a single graphic provides the user with an envelope of potentially expected optical turbulences. The

graphic showing these profiles is simple to construct in HELEEOS. Figure 5.1 shows a sample of what these two overlaid profiles might look like. This plot has operational applicability and emphasizes the strengths of the HELEEOS Climatological  $C_n^2$  vertical turbulence profiles. It makes for an easy to understand graphical depiction of the 80% upper confidence limits at each site for a given season. This assumes though that all other ExPERT Desert and Mid-latitude sites exhibit the same statistical equivalence as those in this test. However, given the number of sites used for the Desert and Mid-latitude analysis, this is a fair assumption.

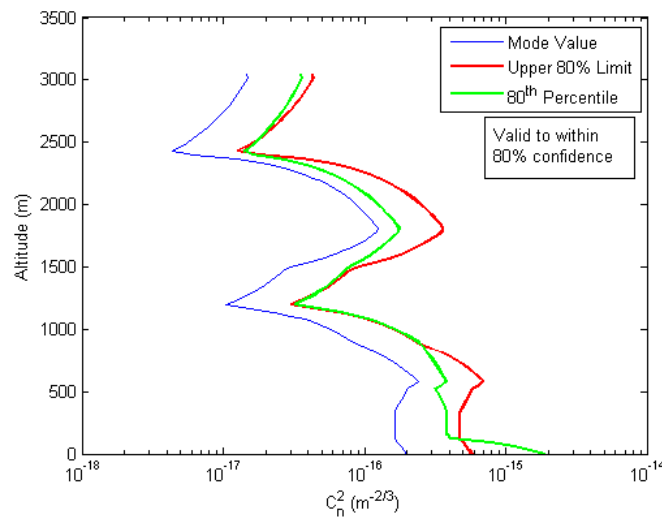


Figure 5.1: Sample Summer Climatological  $C_n^2$  profile depicting envelope of turbulence coverages for Holloman AFB, NM.

A final recommendation specifically relating to this test data is to expand the HELEEOS look-up tables with the thermosonde data used in this research. This includes five new Mid-latitude sites and one additional Desert site. Analysis showed the statistical equivalence of several of these sites and it is important to capitalize on these relevant resources. Chapter 4 points out some of the inherent deficiencies in these Summer and Winter look-up tables. Expanding the databases to include this new information fills the void in the sparsely populated boundary layer regions above 60 m, and enhances the quality of the HELEEOS Climatological  $C_n^2$  profiles. This



is already being accomplished and will be completed by the next HELEEOS version release.

HELEEOS is a solid engagement package, but it is difficult to understand and the user's guide is vague in its explanations. HELEEOS currently has many different atmospheric options (time of day, relative humidity percentiles and turbulence percentiles) for the user to select from. The reasoning for all these selections (time of day, percentiles, etc.) seems to be to cover the gamut of all possible meteorological combinations. However, users many times ignore these extraneous selections in favor of the default values. Atmosphere selections depend on a meteorological savvy user, and this is probably not the case the majority of the time. In addition, the HELEEOS users guide fails to fully explain the idea of percentiles, for both relative humidities and turbulence profiles, and lacks any description of Climatological  $C_n^2$  profiles. The duality in naming conventions results in confusion, this leaves atmospheric parameter decisions up to the user. Most users opt for the defaults in light of selections they do not understand.

Overcoming this obstacle means making the software package easy to use and understand. Relatively few users understand what an 80<sup>th</sup> percentile relative humidity means. Most will likely take this to mean simply 80% relative humidity and this is not what the percentile implies. However, everyone understands what 80% relative humidity means. The relative humidity options need to be changed into a format users will understand and use. Relative humidity categories of "dry," "average," and "moist" mean something to a user and they understand exactly what these categories imply. This same reasoning applies to the turbulence profiles as well. Without adequate descriptions of the Climatological  $C_n^2$  model in the users guide, users have no way of understanding what the percentile really means. Again, put this in terms of something the user does understand. The 99<sup>th</sup> percentile Climatological  $C_n^2$  turbulence profile seems nebulous without a definition; however, giving the user an option for an "Extreme" turbulence case leaves no doubt. The extreme case can be either the current 99<sup>th</sup> percentile, or the curve corresponding the upper 80% confidence range

described previously. Either way, the recommendation is to change the user selections into friendly, easy to understand and easy to use options rather than percentiles.

The AFIT Center for Directed Energy needs to bolster user confidence in the HELEEOS software package. HELEEOS Climatological  $C_n^2$  is a superb optical turbulence model, but it lacks solid user buy-in. The reason for this, at least in this author's mind, is because HELEEOS attempts to be the "end-all" answer to engagement modeling. It attempts to do everything. Building user confidence means wholesale advertising of the things that make this model unique. Climatological  $C_n^2$  is a perfect avenue for this. This is a viable optical turbulence model, rivaling the empirical models and even outperforming them. Studies such as this prove this claim, and more are needed. This research only scratches the surface in when it comes to modeling. However, the Climatological  $C_n^2$  optical turbulence model needs to be thoroughly explored in wave optics simulations before the model will gain widespread support from researchers. This research is a first step in that direction, but other similar efforts are needed to assess HELEEOS-versus-empirical model performance metrics such as thermal blooming, Strehl ratio, scintillation, and power in the bucket projections. The HELEEOS Climatological  $C_n^2$  model holds its own against the empirical models, but without these types of initiatives, user confidence in the Climatological  $C_n^2$  model will remain relatively low.

A final recommendation for future work is a validation effort for the Climatological  $C_n^2$  vertical profiles. Star scintillation measurements provide an  $r_0$  value for the vertical column. The path-integrated  $C_n^2$  value can be backed out from this value, making for an easy comparison between actual data and the HELEEOS predicted value. A concentrated comparison study of HELEEOS to star scintillation data may further enhance the confidence in this model and promote addition user support.

This research demonstrated the accuracy of the HELEEOS turbulence profiles compared to true thermosonde data. This strength needs to be conveyed to the users of HELEEOS. Implementing some of these recommendations will boost the

confidence in the Climatological  $C_n^2$  turbulence model and provide the needed proof that researchers and users appreciate. In doing so, HELEEOS becomes a viable alternative to empirical optical turbulence profiles for EO/IR applications and other mid-tropospheric applications such as the Advanced Tactical Laser.

## Bibliography

1. Andrews L. C. and Phillips R. L. *Laser Beam Propagation through Random Media* (2nd Edition). Bellingham, WA: SPIE Optical Engineering Press, 2005.
2. Beland R. R. *Propagation through Atmospheric Optical Turbulence*. The Infrared and Electro-Optical Systems Handbook, Vol. 2, Bellingham, WA and Ann Arbor, MI: SPIE Optical Engineering Press and Infrared Information Analysis Center, 1993.
3. Boeing.com , “Advanced Tactical Laser (ATL) Advanced Concept Technology Demonstration.” [http://www.boeing.com/news/feature/aa2004/backgrounders/advanced\\_tactical\\_laser.pdf](http://www.boeing.com/news/feature/aa2004/backgrounders/advanced_tactical_laser.pdf), 6 September 2006.
4. Fiorino S. T., Bartell R. J., Perram G. P., Bunch D. W., Gravley L. E., Rice C. A., Manning Z. P., and Krizo M. J. “The HELEEOS Atmospheric Effects Package: A Probabilistic Method for Evaluating Uncertainty in Low-Altitude, High-Energy Laser Effectiveness.” *Journal of Directed Energy Vol 1*. 347–360. Directed Energy Professional Society, Winter 2006.
5. Font C. O., Chang M. P. J. L., Oh E., and Gilbreath C. “Humidity Contribution to the Refractive Index Structure Function  $C_n^2$ .” *SPIE Vol. 6215 Atmospheric Propagation III*. 621502–1:9. 2006.
6. GlobalSecurity.org , “Advanced Tactical Laser (ATL).” <http://www.globalsecurity.org/military/systems/aircraft/systems/atl.htm>, 6 September 2006.
7. Goodman J. W. *Statistical Optics*. Wiley Classics Library Edition, New York, NY: John Wiley & Sons, Inc., 2000.
8. Gravley L. E. *Comparison of Climatological Optical Turbulence Profiles to Standard, Statistical and Numerical Models Using HELEEOS*. MS thesis, Graduate School of Engineering and Management, Air Force Institute of Technology, Wright-Patterson AFB OH, March 2006.
9. Hufnagel R. E. *The IR Handbook*. Ch. 6, Propagation Through Atmospheric Turbulence, Ann Arbor, MI: The Infrared Information Analysis (IRIA) Center, Environmental Research Institute of Michigan, 1993.
10. Jumper G. Y., Roadcap J. R., Adair S. C., Seeley G. P., and Fairley G. “Atmospheric Considerations in Engagement-Level Simulations of Tactical High-Energy Laser Systems.” *Journal of Directed Energy Vol 1*. 183–201. Directed Energy Professional Society, Fall 2005.
11. Jumper G. Y., Roadcap J. R., Tracy P., and McHugh J. P. “Estimating Velocity Turbulence Magnitudes Using the Thermosonde.” *Proceedings of the 41st Aerospace Sciences Meeting and Exhibit*. 1–10. Reston, Va: American Institute of Aeronautics and Astronautics, January 2003.

12. Jumper G. Y., Vernin J., Azouit M., and Trinquet H. "Comparisons of Recent Measurements of Atmospheric Optical Turbulence." *36th Plasmadynamics and Lasers Conference*. 1–12. June 2005.
13. Kopeika N. and Sadot D. "Prediction of  $C_n^2$  on the Basis of Macroscale Meteorology Including Aerosols." *SPIE Vol. 1487 Propagation Engineering: Fourth in a Series(1991)*. 40–50. 1991.
14. Leon-Garcia A. *Probability and Random Processes for Electrical Engineering* (2nd Edition). Reading, MA: Addison-Wesley Publishing Company, Inc., 1994.
15. Magee E. P. Personal Communication, 6 October 2006.
16. Magee E. P. and Ngwele A. M. *ATMTools: A Toolbox for Atmospheric Propagation Modeling*. MZA Associates Corporation, 6651 Centerville Business Pkwy Suite B, Dayton, OH, 45459-2678, May 2006. Version 3.2.219, <http://www.mza.com>, email:atmtools@mza.com.
17. Montgomery D. C. *Design and Analysis of Experiments* (5th Edition). New York, NY: John Wiley & Sons, Inc., 2001.
18. Richardson L. F. *Weather Prediction by Numerical Process*. Cambridge, U.K.: Cambridge University Press, 1922.
19. Roggemann M. C. and Welsh B. *Imaging Through Turbulence*. Boca Raton, FL: CRC Press, 1996.
20. "Defense Acquisitions: Status of Ballistic Missile Defense Program in 2004." United States Government Accountability Office Report to Congressional Committees, March 2004.
21. "Defense Acquisitions: Assessments of Selected Major Weapons Programs." United States Government Accountability Office Report to Congressional Committees, March 2005.
22. Verdeyen J. *Laser Electronics*. Prentice Hall Series in Solid State Physical Electronics, Englewood Cliffs, NJ: Prentice Hall, 1995.
23. White K. O., Garvey D. M., Peterson W. A., Eaton F. D., Brown J. H., Good R. E., and Furukawa P. M. *Atmospheric Characterization at the HIDL Site Clear I Program, 29 August to 28 September 1984*. Technical Report ASL-TR-0180, USAF Geophysics Laboratory, Hanscom AFB, MA and USAF Weapons Laboratory, Kirtland AFB, NM: US Army Atmospheric Sciences Laboratory, August 1985.
24. Williams R. H., "Probability, Statistics and Random Processes for Electrical Engineers." HKN Publishing, 1999.

# REPORT DOCUMENTATION PAGE

Form Approved  
OMB No. 0704-0188

The public reporting burden for this collection of information is estimated to average 1 hour per response, including the time for reviewing instructions, searching existing data sources, gathering and maintaining the data needed, and completing and reviewing the collection of information. Send comments regarding this burden estimate or any other aspect of this collection of information, including suggestions for reducing this burden to Department of Defense, Washington Headquarters Services, Directorate for Information Operations and Reports (0704-0188), 1215 Jefferson Davis Highway, Suite 1204, Arlington, VA 22202-4302. Respondents should be aware that notwithstanding any other provision of law, no person shall be subject to any penalty for failing to comply with a collection of information if it does not display a currently valid OMB control number. PLEASE DO NOT RETURN YOUR FORM TO THE ABOVE ADDRESS.

1. REPORT DATE (DD-MM-YYYY) 22-03-2007		2. REPORT TYPE Master's Thesis		3. DATES COVERED (From — To) Jun 2006 — Mar 2007	
4. TITLE AND SUBTITLE  Assessment of Optical Turbulence Profiles Derived From Probabilistic Climatology				5a. CONTRACT NUMBER	
				5b. GRANT NUMBER	
				5c. PROGRAM ELEMENT NUMBER	
				5d. PROJECT NUMBER	
				5e. TASK NUMBER	
6. AUTHOR(S)  Brett W. Wisdom, Capt, USAF				5f. WORK UNIT NUMBER	
7. PERFORMING ORGANIZATION NAME(S) AND ADDRESS(ES) Air Force Institute of Technology Graduate School of Engineering and Management (AFIT/EN) 2950 Hobson Way WPAFB OH 45433-7765				8. PERFORMING ORGANIZATION REPORT NUMBER  AFIT/GEO/ENP/07-02	
9. SPONSORING / MONITORING AGENCY NAME(S) AND ADDRESS(ES)  N/A				10. SPONSOR/MONITOR'S ACRONYM(S)	
				11. SPONSOR/MONITOR'S REPORT NUMBER(S)	
12. DISTRIBUTION / AVAILABILITY STATEMENT  APPROVED FOR PUBLIC RELEASE; DISTRIBUTION UNLIMITED.					
13. SUPPLEMENTARY NOTES					
14. ABSTRACT This research effort assesses the performance of the High Energy Laser End-to-End Operational Simulation (HELEEOS) Climatological $C_n^2$ optical turbulence model. Path-integrated $C_n^2$ values of two HELEEOS optical turbulence profiles at 3 distinct operational altitudes are compared to values determined from measured thermosonde data. HELEEOS desert and mid-latitude sites are selected from the Extreme and Percentile Environmental Reference Tables (ExPERT) database for comparison to the thermosonde data. Statistical equivalence of the two datasets is determined through a Design of Experiments (DOE) factorial test to within 80% confidence. The HELEEOS profiles are shown to be equivalent to the thermosonde data for a 500 m boundary layer profile. Deterministic values of the 80% confidence intervals are established. The HELEEOS optical turbulence model is used as the input turbulence model for wave optics simulations. Long-term spot size measurements show that HELEEOS outperforms empirical turbulence models by as much as 17%. Recommendations are made to improve the HELEEOS graphical outputs and reference tables.					
15. SUBJECT TERMS  HELEEOS (High Energy Laser End-to-End Operational Simulation), Atmospheric Turbulence, $C_n^2$ , Climatological $C_n^2$ , Thermosonde, Boundary Layer, Design of Experiments (DOE), Factorial Design					
16. SECURITY CLASSIFICATION OF:			17. LIMITATION OF ABSTRACT	18. NUMBER OF PAGES	19a. NAME OF RESPONSIBLE PERSON
a. REPORT	b. ABSTRACT	c. THIS PAGE			Steven T. Fiorino, Lt Col, USAF (ENP)
U	U	U	UU	117	19b. TELEPHONE NUMBER (include area code) (937) 255-3636, ext 4506; email: steven.fiorino@afit.edu